A Langevin Equation Approach to Diffusion Magnetic Resonance Imaging

A thesis submitted for the degree of

Doctor of Philosophy

Presented to:

The School of Medicine, Faculty of Health Sciences, Trinity College Dublin

Author

Jennie Cooke

M. Sc.

Research Supervisor

Dr. Christian Kerskens

Declaration

This thesis is the sole work of the author and has not been submitted in whole or in part to this or any other university for any other degree. The author gives permission for the library to lend or copy this work upon request.

Acknowledgements

I would like to thank my supervisor Dr. Christian Kerskens for the opportunity to pursue a research project in MRI physics. I thank him for his advice on experimental design and the sharing of his knowledge of IDL. I would like to gratefully acknowledge the invaluable advice of Prof. William T. Coffey on the theoretical developments in this thesis. I thank him for his enthusiastic guidance, and the countless hours he spent reading and editing this manuscript. I would also like to thank Prof. Yuri Kalmykov for his constant availability to promptly help with mathematical dilemmas and manuscript editing, despite our different geographical locations. Further thanks go to Liam Cleary and Roisin Rowley-Brook for their help with this project.

Many thanks to Sojo Josephs and Christoph Blau for their assistance with the acquisition of data on the 3T and 7T MRI scanners. I greatly appreciate the support and encouragement of Dr. Thomas Connor and Prof. Marina Lynch. For their company, advice, support and many useful and interesting discussions (on and off topic) I would like to the other members of my group, Michael, Joe and Christoph. I would like to thank all my experimental volunteers for the temporary donation of their brains to science. I am grateful for the support and encouragement of my colleagues in St. Jamess Hospital, especially Dr. Geraldine O'Reilly for facilitating the completion of this work.

I would like to thank my sister, Anna, for her beautiful diagrams, proofreading skills and moral support and encouragement. I also thank my parents for their proofreading, and I am constantly grateful for the love and support of my family, and their belief in me, without which I would never have attempted nor completed this thesis. I would like to thank my father for critically impor-

tant discussions in the early struggles with the equations, and for his unending enthusiastic interest in my studies. I thank my mother for timely messages and calls of concern when they were most needed, and for reminding me of the light at the end of the tunnel.

Finally I would like to thank Paul, without his love and encouragement (and programming help) I definitely could not have completed this work. I will never forget the unending patience, never-failing ability to cheer me up and constant thoughtfulness which he showed me at all times.

Contents

I Overview 3

II Phase Diffusion and Brownian Motion 6

A Brownian Motion 7

B Anomalous Diffusion 15

C The Bloch Equations 18

D The Bloch – Torrey Equation 25

E Diffusion Sensitive Pulse Sequences 29

F Evaluation of the dephasing for various gradients 34

G Summary of the preceding classical results 39

H Deviations from exponential decay 42

I Diffusion in Biological Tissue 53

J Anomalous Diffusion in Tissue 56

K Applications of DWI 61

III A Langevin Equation Approach to Normal Diffusion 70

A Noninertial Diffusion 70

B Diffusion equation for the phase 74

C Phase Diffusion Including the Inertia 78

IV Fractional Diffusion: Possible Explanations of the Stretched Exponential Behaviour using the Fractional Langevin equation . . 86

A Fractional Diffusion 88
B Solution of the Generalised Langevin Equation 90
C Extension to Fractional Diffusion for the Gradient Echo Case 93
D The Spin Echo Calculation 97
E The Ramp and Triangular Gradient Shapes 101
F Conclusion 103
V Magnetic Resonance Imaging Methods 104
A 3T Gradient Echo experiments 105
B 7T Spin Echo experiments 108
VI Results of experimental investigation 111
A Water phantom assessment 111
B Investigation of fractional diffusion equation *in vivo* . . . 115
C Comparison of fractional diffusion equations to a classical approach 128
D Conclusions 134
VII Discussion 135
Appendix 1 141
Appendix 2 144
List of Abbreviations 144

I Overview

Diffusion-weighted magnetic resonance imaging (DW MRI) is a noninvasive technique which is sensitive to the translational motion of water molecules because of their Brownian motion, allowing us to probe the microstructure of living cells and so achieve an understanding of tissue structure. The diffusive behaviour of water in cells alters in many disease states and during neuronal activation. Thus it has become a valuable and widely used diagnostic tool.

The dramatic changes in water diffusivity in tissue following ischemia or observed in tumours, mean that the diffusion-weighted images can provide qualitative information for the purpose of diagnosis and treatment planning. As the degree of diffusion sensitivity is increased in a series of DWI acquisitions, decay of the image intensity due to dephasing, as a result of random modulation of the Larmor frequency caused by the translational Brownian motion of the spin containing liquid molecules is observed. The logarithm of the phase decay in general departs from that predicted by the normal Brownian motion due to the complex cellular environment experienced by the water molecules. For example, the Bloch-Torrey diffusion equation of the magnetization (based on Einstein's theory of the translational Brownian motion) describes accurately the normal phase diffusion behaviour of free water essentially predicting a logarithm of the decay, which is cubic in time. However, the phase decay for free water fails to describe the behaviour of water molecules in human tissue due to the complex cellular environment mentioned above [1]. Hence it has been adapted in a variety of ways (e.g. to stretched exponentials or Kohlrausch–Williams–Watts (KWW) functions i.e. a form of anomalous diffusion), to create empirical formulae which fit the decay curves, however there is much debate about the microscopic explanations which are used to justify these expressions. Thus, if a physically plausible model possessing a

convincing microscopic explanation could be found to fit the decay observed in DWI imaging, it would have the potential to enhance the sensitivity of the technique for the observation of subtle changes in diffusion.

As a step towards achieving this goal it is the purpose of this thesis to first outline the normal phase diffusion problem and its treatment without the use of probability density diffusion equations, by means of the inherently simpler Langevin equation for the random variables, describing the problem using only the properties of the characteristic function of Gaussian random variables [1].

Next, in order to provide a possible microscopic explanation for the stretched exponential behaviour referred to above, it will be shown how the Langevin treatment may be simply extended [1] to anomalous diffusion giving rise to stretched exponential decay using a fractional generalisation of the Langevin equation proposed by Lutz [2], which in the present instance describes the dependence of the phase decay on its past history.

This equation describes the fractional Brownian motion of a free particle coupled to a fractal heat bath and so [2] represents Gaussian transport with the non-Markovian character being expressed via a memory function. In other words, in accordance with the pioneering work of Mandelbrot and van Ness [3] (See [4] for a comprehensive review), it allows one to include in the phase decay the fact observed in a host of natural time series, that the "span of interdependence" between samples of a random function may be infinite, unlike in Markov processes in which sufficiently distant samples of random functions are independent or nearly so. Indeed the concept of memory has been well put by Metzler and Klafter [4]; " unlike in a Markov process the now – state of the system depends on the entire history from its preparation". The fractional Brownian motion, stemming from a fractional Langevin equation rather than the continuous time random walk (CTRW) often used to discuss anomalous

diffusion is favoured here because it preserves many features associated with that walk, e.g. the stretched exponential decay while retaining the computational simplicity associated with Gaussian random variables.

The theoretical results for the phase decay are then compared with the results of diffusion weighted experiments acquired from human subjects on a 3T MRI scanner, and animals on a 7T small bore MRI scanner.

II Phase Diffusion and Brownian Motion

During signal acquisition in magnetic resonance imaging, nuclear magnetic moments are manipulated via a combination of static, gradient, and radiofrequency magnetic fields. These fields and their relative timing (or pulse sequences) can be varied in many ways in order to create image contrast based on characteristics of the medium, tissue or pathology. The study of water in living systems using nuclear magnetic resonance methods has unique advantages because they measure the signal from intrinsic water molecules directly and non-invasively. In addition to varying tissue contrast, flowing, diffusing and perfusing spins can be encoded in the image signal. The clinical applications of diffusion MRI are numerous, and changes in water diffusion in neuronal tissues have been associated with alterations in physiological and pathological states. These include the early detection of acute stroke [5], functional brain imaging [6], white matter fibre tracking [7], and the detection of multiple sclerosis [8] and tumours [9].

The precession and relaxation of the net magnetization, as a result of the spin manipulation, is described by the phenomenological Bloch equations [10]. In liquids, however, the positions of the spin containing molecules fluctuate due to Brownian motion so that the Larmor precession is randomly modulated, causing dephasing of the resonance signal. In other words, the magnetic field is no longer constant in space, but has a field gradient $\mathbf{G}$, defining the magnitude of the field at the site of a nucleus given by the position vector, $\mathbf{r}$, causing phase fluctuations

$$\Delta\Phi(t) = \int_0^t \omega(t')dt' = \gamma \int_o^t \mathbf{r}(t') \cdot \mathbf{G}(t')dt', \tag{1}$$

where γ is the gyromagnetic ratio. Dephasing as a result of random modulation

of the Larmor frequency, $\omega(t)$, was first observed by Hahn [11], who noted the attenuation of the observed transient signals in NMR experiments due to the self diffusion of 'spin-containing liquid molecules'.

Diffusion due to the Brownian motion of the liquid molecules during the application of a magnetic field gradient causes a dephasing of the transverse magnetisation. This results in a loss of the acquired signal. The extent of the signal attenuation depends on both sequence and sample parameters. The inclusion of a diffusion weighting gradient causes a sequence to be sensitive to molecular diffusion. The attenuation is also dependent on tissue type and microstructure, as well as on its physiological state. Magnetic resonance imaging methods which are designed to probe microscopic diffusion are called diffusion imaging sequences. The category of diffusion imaging can be subdivided into a number of different techniques including diffusion-weighted imaging (DWI), apparent diffusion coefficient (ADC) mapping, diffusion tensor imaging (DTI) , q-space imaging and diffusion spectroscopy.

A Brownian Motion

Diffusion is a manifestation of the random translational motion of molecules due to their thermal energy. The random walk [12, 13] executed by the diffusing molecules is called Brownian motion. Following the account of the phenomenon first recorded in a systematic way by the botanist Robert Brown in 1827 [12], the characteristics of Brownian motion as observed from detailed experiments were described by Gouy [12, 14]. The motion of a Brownian particle is very irregular; it's trajectory comprises translations and rotations and appears to have no tangent. The composition and density of the particles do not influence the motion, however the smaller their size, the more active the motion. In a less viscous fluid, or at higher temperatures the motion is also more vigourous.

The motion of the particles never ceases.

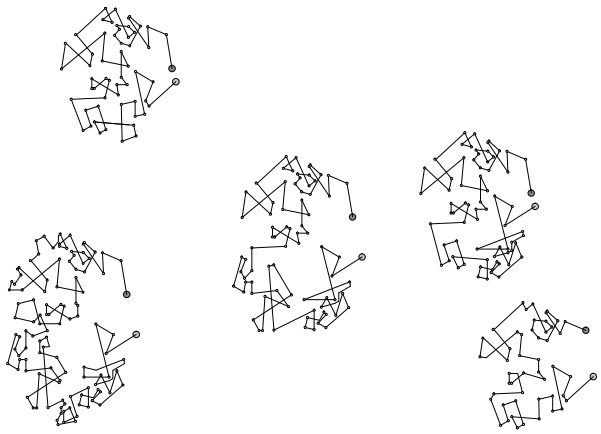

Figure 1: An example of particles performing a random walk. The dots indicate either the start or end of an observation time interval.

Several different approaches to the mathematical description of Brownian motion were developed towards the beginning of the 20^{th} century, however only two will be discussed here. Einstein's theory of the Brownian motion was based on the probability densities for a large ensemble of particles, whereas that of Langevin was developed from a single stochastic realisation of the process.

Einstein's theory of Brownian motion considers the Brownian particle to be a large particle in a fluid performing a discrete time random walk, where the walk is a result of continuous collisions with the molecules of the fluid. He assumed that the particles are non-interacting and therefore independent. The observation time is chosen which is much greater than τ, the time interval between displacements. However τ is assumed large enough that the motion has no long term memory, and that the motion of the walker at τ is statistically independent of its motion at $t \pm \tau$. The displacement of the particles is considered to be composed of very small, independent steps with a symmetric distribution of step lengths.

Following Einstein we consider a large ensemble of Brownian particles in

an element $x \rightarrow x + dx$ whose concentration at time t is f. The probability of a particle entering a neighbouring element of equal size, x, after a time interval τ is

$$\phi(x - x', \tau) = \phi(\Delta, \tau) \tag{2}$$

As the random walk is unbiased it follows that,

$$\phi(-\Delta, \tau) = \phi(\Delta, \tau) \tag{3}$$

The Smoluchowski integral equation is the sum over all neighbouring elements such that,

$$f(x, t + \tau) = \int_{-\infty}^{\infty} f(x + \Delta, t)\phi(\Delta, \tau)d\Delta. \tag{4}$$

$\phi(\Delta, \tau)$ must be defined, as it is the physical cause for the random process. In this case ϕ is defined such that the random walker moves a step Δ to the right or Δ to the left along the x-axis, where the duration of each step is τ. Both τ and Δ are small compared with the observation intervals and thus f can be expanded in Taylor series as:

$$\begin{aligned} \sum_{n=0}^{\infty} \frac{\tau^n}{n!} \frac{\partial^n f}{\partial t^n} &= \sum_{n=0}^{\infty} \left(\frac{\int_{-\infty}^{\infty} \Delta^n \phi(\Delta, \tau) d\Delta}{n!} \right) \frac{\partial^n f}{\partial x^n} \\ &= \sum_{n=0}^{\infty} \frac{\langle \Delta^{2n} \rangle}{(2n)!} \frac{\partial^{2n} f}{\partial x^{2n}} \end{aligned} \tag{5}$$

where on account of Eq.(3)

$$\langle \Delta^{2n+1} \rangle = 0 \tag{6}$$

If we now assume that we are considering tiny displacements in infinitesimally short times such that Δ and τ approach zero then we have,

$$\lim_{\substack{\Delta \to 0 \\ \tau \to 0}} \frac{\langle \Delta^2 \rangle}{2\tau} = D \tag{7}$$

and if all terms higher than τ^2 in Eq 5 vanish, the result is Fick's diffusion equation [13, 15, 16, 17],

$$\frac{\partial f}{\partial x} = D \frac{\partial^2 f}{\partial x^2} \tag{8}$$

Where f is the probability that, from a starting position of x_0 at t_0 the Brownian particle may be found in element $x \to x + dx$ at time t,

$$f dx = f(x, t | x_0, t_0) dx \tag{9}$$

The explanation for the omission of the higher order terms in Eq 5 is the following. The probability distribution of displacements for the random walker $\phi(\Delta, \tau)$ in a time τ stems from the ceaseless collisions with the particles of the surrounding fluid. Therefore the resulting net displacement, Δ of the Brownian particle is the sum of the statistically independent individual jumps arising from the collisions and so the central limit theorem can be applied.

The central limit theorem states that if $\{\xi_i\}$ is a sequence of n independent random variables, where each variable has a arbitrary distribution, then the total tends towards a normally distributed random variable (i.e. Δ) as $n \to \infty$

$$\xi = \frac{\xi_1 + \xi_2 + ... + \xi_n}{\sqrt{n}} \tag{10}$$

Given that ξ_i has a zero mean and a variance of $\langle \xi_i^2 \rangle = \sigma_i^2 < \infty$, the total, also has a zero mean and a variance σ^2 where:

$$\sigma^2 = \frac{1}{n} \sum_{i=1}^{n} \sigma_i^2 \tag{11}$$

Thus our particular random variable, the elementary displacement Δ, is Gaussian and so,

$$\langle \Delta^{2n} \rangle = (2n-1)!! \langle \Delta^2 \rangle^n \tag{12}$$

Returning again to Eq 8, the solution is a Gaussian (called the Green function),

$$f(x,t|x_0,t_0) = \frac{1}{\sqrt{4\pi D|t-t_0|}} e^{-\frac{[x(t)-x(t_0)]^2}{4D|t-t_0|}} \tag{13}$$

termed the Wiener process [18], and it describes the probability distribution of the displacements of a Brownian particle. It has a variance representing the mean-squared displacement along the x-axis:

$$\sigma^2 = \langle [x(t) - x(t_0]^2 \rangle = 2D|t - t_0| \tag{14}$$

and a characteristic function,

$$F_x(\kappa, t) = \int_{-\infty}^{\infty} e^{-\kappa x} f dx = e^{-\frac{\kappa^2 \sigma^2}{2}} \tag{15}$$

Where κ denotes the wave number. Eq. 15 is also known as the intermediate scattering function or structure function and processes with scattering functions of this form are known as Debye relaxation processes [19]. In the context of NMR, when transformed to the phase variable, this function produces a dephasing where the argument of the exponential is cubic in time.

Wiener showed that the sample paths $[x(t) - x_0]$ of the Brownian motion are almost everywhere continuous but nowhere differentiable. σ is not mean square differentiable, and therefore the velocity of the particles cannot be expressed. It must also be noted that the equality of Eqs (14) and (7) illustrate the self-similar or fractal nature of the random walk. In other words the Brownian paths appear to be the same on average.

Einstein determined the diffusion coefficient D by considering the random walk of a particle in a potential well $V(x)$, and placing the condition that the Boltzmann distribution of positions must prevail ($\dot{f} = 0$), so that the diffusion current j is zero. Thus the mean squared displacement of the particle along the x-axis would be,

$$\left\langle [x(t) - x(t_0)]^2 \right\rangle = \frac{2kT}{\zeta} |t - t_0| \tag{16}$$

where ζ is the vicsous drag force and is defined from Stoke's Law as $\zeta = 6\pi\eta a$, where the particle has a radius a and is moving in a fluid of viscosity η. Eq. (16) provides a method of experimental measurement of the diffusion coefficient. Eq.(16) illustrates the relationship, observed by Gouy [12], between the displacements of the Brownian particle and the thermal energy kT. In 1908, Perrin [14, 18, 20] successfully calculated the Avogadro number from observations of the mean square displacement of a Brownian particle so confirming Eq.(16).

The diffusion equation (Eq.(8)) in the presence of a potential $V(x)$ becomes the Smoluchowski differential equation,

$$\frac{\partial f}{\partial t} = \frac{\partial}{\partial x}\left(D\frac{\partial f}{\partial x} + \frac{f}{\zeta}\frac{\partial V}{\partial x}\right) = -\frac{\partial j}{\partial x} \tag{17}$$

When thermal equilibrium is established, the drift current due to the force of the potential V is exactly balanced by the diffusion current created by the Brownian motion, and the Boltzmann distribution in the well will be maintained.

Einstein's description of Brownian motion was not fixed to a detailed model, but rather based on general statistical assumptions [20]. Langevin's "infinitely simpler" approach used the fact that on average the motion of the random walker in a fluid is governed by Newtonian dynamics under friction, $m\dot{v} = -\zeta v$, where ζ once again is the viscous drag on the particle. This equation however leads to the continuous decay of the particles velocity. In order to include the observed unceasing and haphazard nature of the Brownian motion an additional fluctuating force or noise term must be added, $\lambda(t)$, due to the action of the molecules of the surrounding fluid [18, 20]. The fluctuating force is assumed to have zero mean so that on average it does not cause the overall

motion, and to be independent of x. Thus the stochastic differential equation for the random variables (x, v) may be written,

$$m\frac{dv}{dt} + \zeta v = \lambda(t), \qquad \frac{dx}{dt} = v \tag{18}$$

in which the noise term $\lambda(t)$ has the properties

$$\langle \lambda(t) \rangle = 0 \tag{19}$$

$$\langle \lambda(t_1)\lambda(t_2) \rangle = 2kT\zeta\delta(t_1 - t_2) \tag{20}$$

(δ denoting the Dirac–delta function) where the angular braces denote the statistical average of λ over its realizations. Setting $t_0 = 0$ and averaging over the realisations of the phase path $(x,\, v)$ then produces,

$$\left\langle [x(t) - x(0)]^2 \right\rangle = \frac{kTm}{\zeta^2}\left(\frac{\zeta|t|}{m} - 1 + e^{-\frac{\zeta|t|}{m}}\right) \tag{21}$$

Eq. (21) is equivalent to Einstein's result only for times $t >> m/\zeta$. Einstein assumed that the times scales for the motion of the particles under consideration were so long that the two latter terms of Eq.(21) were negligible. However by the introduction of the concept of random variables the result of Langevin (Eq(21)) was mean square differentiable, which makes possible the calculation of the r.m.s velocity of the Brownian particle [20]. At short times $t << m/\zeta$,

$$\left\langle [x(t) - x(0)]^2 \right\rangle = \frac{kT}{2m} t^2 \tag{22}$$

which is r.m.s. differentiable and represents the ballistic limit. Furthermore, the intermediate scattering function,

$$\exp\left\{ - \frac{\kappa^2 \langle [x(t) - x(0)]^2 \rangle}{2} \right\}$$

predicts a discrete set of Debye–like relaxation modes rather than the single Debye mode of the non-inertial limit [21].

B Anomalous Diffusion

The theories of Einstein and Langevin discussed in the above paragraphs are based on a discrete time random walk. The discrete time random walk can be schematically illustrated using Fig. 2(b) adapted from Metzler and Klafter[22].

The walker jumps at each waiting time step of $t = 0$, $t = \tau$, $t = 2\tau$ to its *nearest* neighbour in a randomly selected direction, thereby covering the distance Δ, the lattice constant. Thus, the only variable is the *direction* of the jump length vector, Δ and the motion is *local* in both space and time. The foregoing situation (which gives rise for a free Brownian particle to Eq. (14)) is in contrast to the continuous time random walk model (CTRW) first introduced by Montroll and Weiss [18, 22] in order to render time continuous in a random walk without appeal to the diffusion limit. The CTRW model which may be *nonlocal* in both space and time is based on the idea that the waiting time between jumps, as well as the length of a jump are now random variables which may be drawn from a joint probability distribution of

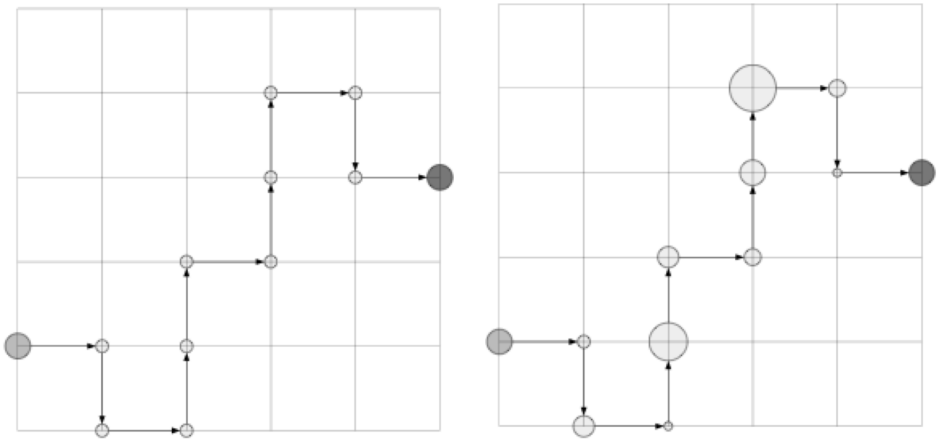

(a) Normal Diffusion (b) Anomalous Diffusion

Figure 2: Adapted from Metzler and Klafter [22]. The grid cross-sections represent the new random positions which the particle may jump to during a random walk. The circle diameter indicates the length of time spent at each position. For normal Brownian motion the jump lengths are equal, (as shown by the equal grid spacings), as are the times spent at each position. For a continuous time random walk, Fig.2(b), the jump lengths remain equal, while there is a distribution of waiting times after each jump, depicted by the varying sizes of circles.

jump times and jump lengths, in which either the mean waiting time or the jump length variance or indeed both may diverge giving rise to the nonlocal behaviour.

CTRW models with divergent mean waiting times (signifying the occurrence of deep traps which subsequently immobilise the diffusing particle) and finite jump length variance are called *fractal time random walks* while those with divergent jump lengths and finite waiting times are known as *Lévy flights*. The fractal time random walk always give rise to subdiffusion [18], as the random walker always risks being trapped at some site for an arbitrarily long time, before he can advance a distance proportional to the finite variance of the jump length distribution. This walk in the noninertial and diffusion limit always gives rise to a mean squared displacement of the form [23].

$$\langle x^2 \rangle = \frac{2}{\Gamma(1+\alpha)} D_\alpha t^\alpha, \quad 0 < \alpha < 1 \tag{23}$$

and an intermediate scattering function,

$$F_x(\kappa, t) = E_\alpha[-\kappa^2 D_\alpha t^\alpha] \tag{24}$$

where E_α is the Mittag–Leffler function [18] defined by,

$$E_\alpha(z) = \sum_{n=0}^{\infty} \frac{z^n}{\Gamma(1+n\alpha)} \tag{25}$$

which interpolates between initial stretched exponential (KWW) behaviour viz

$$E_\alpha[-\kappa^2 D_\alpha t^\sigma] \sim \exp\big(-\kappa^2 D_\alpha \frac{t^\alpha}{\Gamma(1+\alpha)}\big) \tag{26}$$

and long time inverse power law behaviour which represents a memory of the initial conditions.

$$E_\sigma[-\kappa^2 D_\alpha t^\alpha] = \frac{1}{\kappa^2 D_\alpha t^\alpha \Gamma(1-\alpha)} \tag{27}$$

The generalised diffusion coefficient above D_α in Eq.(23) has the dimension $[\mathrm{D}_\alpha]\mathrm{cm}^2\ \mathrm{s}^{-\alpha}$. When $0 < \alpha < 1$, the displacement is subdiffusive. In contrast to the fractal time random walk [24], the long jumps or Lévy flight model in particular the *Weierstrass random walk*, where all steps take the same average

time and the variance of the displacement diverges, leads to enhanced diffusion (where $1 < \alpha < 2$) and ultimately turbulence [22].

However, as mentioned in the Overview, rather than use any of the treatments of anomalous diffusion based on the CTRW we prefer to use (following [1]) instead, the concept of the fractional Langevin equation, as that equation allows us to treat anomalous diffusion by including memory effects in the normal Langevin equation. Thus, one may avoid the computational difficulties associated with random walk models where non-Gaussian random variables are always involved [23].

In order to illustrate the application of the theory of the Brownian motion to phase diffusion we must first review the phenomenological Bloch equations governing the behaviour of the magnetisation of the nuclear moments.

C The Bloch Equations

Nuclear spin has an associated nuclear magnetic moment, parallel to its own orientation [10, 25]. Felix Bloch in attempting to measure the magnetic moment of the free neutron accurately, using what was then known as the magnetic resonance method, developed a new phenomenological method for studying nuclear moments in any substance, for which he was awarded the Nobel Prize in physics (1952) jointly with Edward Mills Purcell. This method is the foundation of modern NMR spectroscopy and MRI techniques [26].

Bloch [10] considered the behaviour of an ensemble of non-interacting nuclei, in a macroscopic sample of matter, acted upon by two orthogonal external magnetic fields viz. a weak radio-frequency field superimposed on a strong constant field. To achieve magnetic resonance the changes of orientation of the nuclear moments must be detected. He proposed a simple method of detecting the reorientations through the use of radio reception, because a

voltage difference between the terminals of an external circuit would be induced as a result of the changing orientations of the magnetic moments [10], following of course from the dynamo equation,

$$\bigtriangledown \times \mathbf{E} = -\dot{\mathbf{B}} \tag{28}$$

$$\tag{29}$$

and the constitutive equation,

$$\mathbf{B} = \mu_0 \mathbf{H} + \mathbf{M}. \tag{30}$$

Next, Bloch proposed phenomenological equations [10, 19, 26] to calculate nuclear magnetization as a function of time. He assumed "that the changes of orientation of each nucleus are solely due to the presence of the external field" and secondly, "that the external fields are uniform throughout the sample" [10]. The first assumption implies that the system is closed; that is the effect of coupling of the moments to the surrounding heat bath is ignored. Under these assumptions he wrote down a set of simplified phenomenological equations for the time evolution of the magnetisation as follows. The static external magnetic field has components

$$\begin{aligned} H_x &= 2H_1 \cos \omega t \\ H_y &= 0 \\ H_z &= H_0 \end{aligned} \tag{31}$$

where, by convention, the constant field is taken to be in the z-direction with strength H_0 and the radiofrequency (rf) field in the x-direction with amplitude

$2H_1$ and angular frequency ω. The resultant angular momentum vector, $\mathbf{A}$, of all the nuclei contained in a unit volume satisfies the classical torque equation,

$$\frac{d\mathbf{A}}{dt} = \mathbf{T} \tag{32}$$

where $\mathbf{T}$ represents the total torque acting upon the nuclei and can be expressed as

$$\mathbf{T} = \mathbf{M} \times \mathbf{H} \tag{33}$$

Here the vector $\mathbf{M}$ is the nuclear magnetization, that is the resultant nuclear magnetic moment per unit volume. For each nucleus we have the relation,

$$\mu_e = \gamma_e J_e = \gamma I \hbar \tag{34}$$

with μ and J_e representing the magnitude of the magnetic moment and the angular momentum respectively, where γ is the gyromagnetic ratio and I is nuclear spin. This relation can be extended to the resultant quantities $\mathbf{M}$ and $\mathbf{A}$ such that

$$\mathbf{M} = \gamma \mathbf{A} \tag{35}$$

By combining Eqs (32), (33) and (35), an expression for the variation of magnetisation with time can be obtained:

$$\frac{d\mathbf{A}}{dt} = \mathbf{T}$$
$$\mathbf{A} = \frac{\mathbf{M}}{\gamma}$$

that is,

$$\frac{d\mathbf{M}}{dt} = \gamma[\mathbf{M} \times \mathbf{H}] \tag{36}$$

Bloch [10] further imposed a number of conditions in order to solve this equation. He asserted that $H_0 >> H_1$, and that both fields are positive and spatially uniform. He also assumed that the angular frequency of the weak field is close to the Larmor frequency of the system

$$\omega_0 = \gamma H_0 \tag{37}$$

Therefore the x-direction field can be replaced by a field which rotates about the z-axis,

$$H_x = H_1 \cos \omega t$$
$$H_y = \pm H_1 \sin \omega t$$

z is the direction of rotation as signified by the sign of the y-component. Bloch introduced a polar angle, θ, which has a constant value such that,

$$\tan \theta = \frac{\gamma H_1}{\gamma H_0 \pm \omega} \tag{38}$$

next by letting

$$\frac{\omega}{|\gamma|} = H^* \tag{39}$$

where H^* denotes the field at which the Larmor frequency is equal to the

frequency of H_1, such that,

$$\tan\theta = \frac{H_1}{H_0 - H^*} \tag{40}$$

and writing

$$M_x = M\sin\theta\cos\omega t; \qquad M_y = \pm M\sin\theta\sin\omega t; \qquad M_z \quad = M\cos\theta \tag{41}$$

it is clear that M, the magnitude of the magnetization, is constant. Eq.(41) demonstrates that the magnetization rotates about the z-axis, in the plane common to the rotating $x-y$ component and the z-component. By introducing,

$$\delta = \frac{H_0 - H^*}{H_1} = \cot\theta \tag{42}$$

where δ is the deviation between the static field H_0, and the resonance value of this field H^*, normalised with respect to the magnitude of the oscillating field H_1, Eq.(41) may be rewritten as,

$$M_x = M\frac{\cos\omega t}{\sqrt{1+\delta^2}}, \tag{43}$$

$$M_y = \pm M\frac{\sin\omega t}{\sqrt{1+\delta^2}}, \tag{44}$$

$$M_z = M\frac{\delta}{\sqrt{1+\delta^2}}. \tag{45}$$

In the original set of idealised Bloch equations (43)-(45) it is assumed that the system is closed, i.e. that there is no energy exchange between the magnetization and the surrounding heat bath. However, in practise energy exchange exists between the nuclei and their surroundings. This exchange causes relaxation leading to dephasing of the x-y components of the magnetization.

Bloch [10, 19] accounted for the effects of the heat bath by the introduction of two damping terms. The first was a longitudinal, or spin-lattice relaxation time, T_1. This is the characteristic time constant used to describe the exponential time rate of change of M_z, the z-component of magnetization, due to the thermal agitation (the interaction of the nuclei with the surroundings):

$$\frac{dM_z}{dt} = \frac{-(M_z - M_0)}{T_1} \tag{46}$$

where M_0 is the value of M_z at equilibrium and hence the stationary solution of Eq.(46). The second damping term describes the dephasing of the transverse magnetisation. Contributions to this relaxation effect include inhomogeneities in the H_0 field and intermolecular magnetic fields. Intermolecular magnetic fields cause individual spins to precess at slightly different frequencies, thus leading to dephasing. Consequently, Bloch [10] introduced the transverse or spin-spin relaxation time, T_2, which is the characteristic time constant of exponential decay of the transverse magnetisation.

The complete Bloch equation including the damping terms then becomes [10],

$$\frac{d\mathbf{M}}{dt} = \gamma \mathbf{M} \times \mathbf{H} - \frac{M_x}{T_2}\mathbf{i} - \frac{M_y}{T_2}\mathbf{j} - \frac{-(M_z - M_0)}{T_1}\mathbf{k} \tag{47}$$

where $\mathbf{i}$, $\mathbf{j}$ and $\mathbf{k}$ denote the usual triad of unit vectors. We remark in passing that this phenomenological equation may be justified on a microscopic basis by considering an assembly of non-interacting nuclei [27]. Now the external field has the form

$$\mathbf{H}(t) = H_0\mathbf{k} + \mathbf{H}_1(t) \tag{48}$$

where $\mathbf{H}_0$ is strong and constant while $\mathbf{H}_1$ is relatively weak and an arbitrary function of the time. To study relaxation we suppose that $\mathbf{H}_1$ is suddenly switched off, then the Bloch equations become,

$$\frac{d\mathbf{M}}{dt} = \gamma\big[H_0 M_y \mathbf{i} - H_0 M_x \mathbf{j}\big] - \frac{M_x}{T_2}\mathbf{i} - \frac{M_y}{T_2}\mathbf{j} - \frac{(M_z - M_0)}{T_1}\mathbf{k} \tag{49}$$

Clearly in the absence of H_1, the transverse and longitudinal components of $\mathbf{M}$ separate, and if we form the complex variable $M_\perp(t) = M_x(t) + iM_y(t)$, we then have,

$$\dot{M}_\perp = -i\gamma M_\perp H_0 - \frac{M_\perp}{T_2} \tag{50}$$

For a constant field H_0 the solution to this differential equation is simply,

$$M_\perp(t) = M_\perp(0) e^{-\frac{t}{T_2}} e^{-i\omega_0 t} \tag{51}$$

where the Larmor frequency is $\omega_0 = \gamma H_0$. This is a decaying oscillation. In reality, H_0 is not constant in space due to inhomogeneities in the field and the addition of gradient pulses so that a gradient field, $\mathbf{G}$ exists, defining the magnitude of the field at the site of a nucleus, given by the position vector, $\mathbf{r}$, such that

$$H(\mathbf{r}, t) = \mathbf{r}(t) \cdot \bigtriangledown H(z, t) = \mathbf{r}(t) \cdot \mathbf{G}(z, t), \tag{52}$$

Hence the transverse magnetisation, besides being a function of time, is also a function of position. Therefore the solution of Eq.(50) alters to

$$M_{\perp}(\mathbf{r},t) = M_{\perp}(\mathbf{r},0)\exp\left[-\frac{t}{T_2} - i\gamma\int_0^t \mathbf{r}(t')\cdot\mathbf{G}(z,t')dt'\right] \tag{53}$$

Thus the separated transverse component of the magnetisation is also a function of the position of the nucleus.

D The Bloch – Torrey Equation

Despite the inclusion of terms representing the interaction with the surroundings in the Bloch equations as illustrated above, Eq.(53), still ignores the fact that the nuclei are embedded in liquid particles so that the Brownian motion of the surroundings causes the position vector, $\mathbf{r}$, to fluctuate. Hence Eq.(53) becomes the stochastic differential equation [1],

$$\dot{M}_{\perp} = -(i\gamma\mathbf{r}\cdot\mathbf{G} + 1/T_2)M_{\perp} \tag{54}$$

Equation (54) now represents the Langevin equation of the process [1, 18]. We can simplify the problem so that the damping term is incorporated into the time derivative and simply calculate the dephasing effect. Hence we see that the dephasing due to the thermal motion of the nuclei bearing the magnetic moments is obtained by calculating the mean value of the functional $\langle e^{i\Delta\Phi}\rangle$ (essentially the intermediate scattering or structure function), where

$$\Delta\Phi = -\gamma\int_0^t \dot{\mathbf{r}}(t_1)\int_0^{t_1}\mathbf{G}(t')dt'dt_1 \tag{55}$$

is the instantaneous dephasing. Equation (55) is obtained by integration by parts from Eq. (1), by imposing the so-called rephasing condition $\int_0^t \mathbf{G}(t')dt' =$

0. Clearly, this calculation merely amounts to determining the characteristic function of the centred random variable, $\Delta\Phi$. This is particularly easy for centered Gaussian processes because then one may write [18] since Eq. (55) is simply a linear transformation of a Gaussian random variable and so is itself Gaussian.

$$\left\langle e^{i\triangle\Phi}\right\rangle = e^{-\frac{\langle\triangle\Phi^2\rangle}{2}} \tag{56}$$

Thus if we regard the particles carrying the nuclei as free Brownian particles, we can determine the dephasing by means of Eq. (56), which is the starting point of our Langevin equation method to be outlined later.

In contrast, the approach taken by Torrey [28] was to take the deterministic ordinary differential equation Eq. (50) and, following Einstein [18], to add a diffusion term, $D\bigtriangledown^2 M_\perp$ to account for the dephasing where D is the diffusion coefficient. Thus Eq. (50) becomes the partial differential equation,

$$\frac{\partial M_\perp(r,t)}{\partial t} = -i\gamma(\mathbf{r}\cdot\mathbf{G})M_\perp + D\bigtriangledown^2 M_\perp \tag{57}$$

now called the Bloch-Torrey equation. This equation has an advantage over previous approaches such as that of Carr and Purcell [29], in so far as it allows one to systematically study dephasing in the presence of a boundary [30]. The Bloch-Torrey equation may be solved for diffusion in an infinite reservoir by assuming the solution is of the form

$$M_\perp(\mathbf{r},t) = M_0 S(t)\exp\big[-i\gamma\mathbf{r}\cdot\int_0^t \mathbf{G}(t')dt'\big] \tag{58}$$

yielding,

$$\frac{1}{S}\frac{\partial S}{\partial t} = e^{i\gamma \mathbf{r}\cdot\int_0^t \mathbf{G}(t')dt'}.D.\bigtriangledown^2\left(e^{-i\gamma \mathbf{r}\cdot\int_0^t \mathbf{G}(t')dt'}\right) \tag{59}$$

so that,

$$\ln S(t) = -D\gamma^2\int_0^t\left(\Big[\int_0^t \mathbf{G}(t')dt'\Big]\Big[\int_0^t \mathbf{G}(t')dt'\Big]\right)dt + \ln S(0) \tag{60}$$

This expression can be used to determine the effect on the signal intensity of specific experimental design parameters for a gradient or spin echo experiments. Thus, Torrey [28] obtained the well-known Carr-Purcell [29] result, (originally obtained by them by considering the diffusion limit [13, 15, 16] of the discrete time random walk of the phase), for the dephasing following the application of a step gradient of magnitude G, in a liquid characterized by a diffusion coefficient D, namely,

$$\langle e^{i\Delta\Phi}\rangle = \frac{S(t)}{S(0)} = \exp\Big[-\frac{1}{3}D\gamma^2G^2t^3\Big] \tag{61}$$

It follows that the microscopic diffusion coefficient of a particle in a fluid can then be measured via the amplitude of the echo signal from nuclear spins subject to an appropriate sequence of magnetic field pulses. We recall that the diffusion coefficient is defined by the mean square displacement of the Brownian particle x coordinate (ignoring the inertia), in an elapsed time

interval t between observations,

$$\langle(\triangle x)^2\rangle = \langle[x(t) - x(0)]^2\rangle = 2Dt$$

In order to further utilize Eqs (55) or (60) we must first discuss diffusion sensitive pulse sequences.

E Diffusion Sensitive Pulse Sequences

Magnetic field gradients are employed not only to spatially encode but also to produce specific contrast within the magnetic resonance imaging signal. In order to sensitize an imaging sequence to molecular diffusion, a diffusion-weighting gradient must be included. Diffusion weighting gradients can be incorporated in any pulse sequence, however, spin echo sequences are traditionally favoured over gradient echo sequences [31]. The diffusion-weighting gradient typically consists of two lobes of equal area.

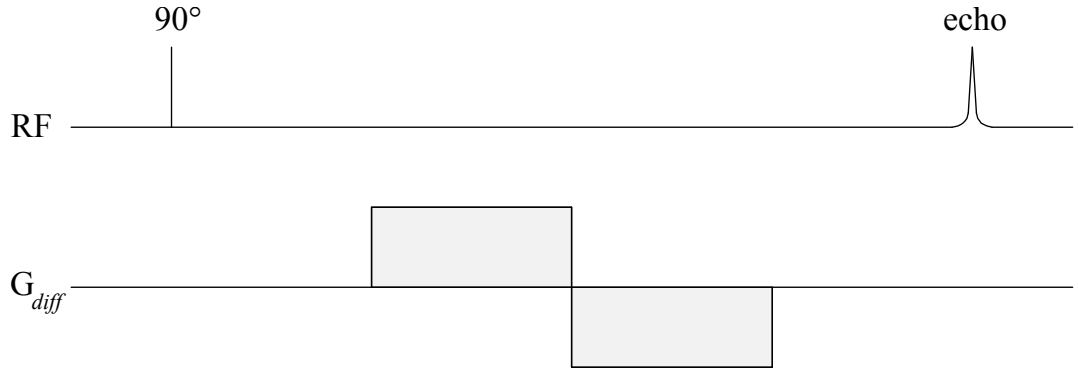

(a) The Gradient Echo Diffusion Weighted Pulse Sequence

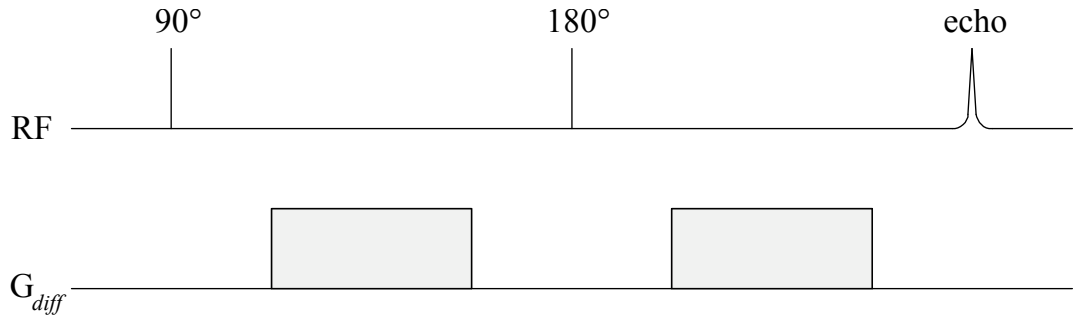

(b) The Spin Echo Diffusion Weighted Pulse Sequence

Figure 3: A simple timing diagram of the gradient echo and spin echo pulse sequences, showing the additional gradient pairs which sensitize them for diffusion.

When applied to a gradient echo sequence the lobes have opposite polarity,

creating the so-called *bipolar* gradient. In the spin echo sequence, the lobes have the same polarity, and are placed symmetrically on either side of the 180^o refocussing pulse. The refocussing RF pulse reverses the polarity of the second lobe in this sequence. The purpose of the gradients is to magnetically label the spins carried by the water molecules. The first gradient lobe causes a phase shift of the transverse magnetisation, ϕ_1 which depends on the spin position [32] viz.

$$\phi_1 = \gamma \int_0^{\delta} G x_1 dt = \gamma G \delta x_1 \tag{62}$$

where the field gradient is applied along the x-direction, and the duration of the gradient lobe is δ. The second gradient pulse produces a phase shift

$$\phi_2 = \gamma \int_{\delta}^{2\delta} G x_2 dt = \gamma G \delta x_2 \tag{63}$$

in the opposite direction. Hence the net dephasing is given by,

$$\triangle\phi = \phi_2 - \phi_1 = \gamma G \delta (x_2 - x_1) \tag{64}$$

Spins for whom no change in position occurs have $x_1 = x_2$, so that no net dephasing occurs. If the spin-carrying liquid molecules undergo translational motion during the application of the gradients, then there will be net dephasing which will affect the transverse magnetisation. In other words, static spins are rephased by the second gradient lobe, while spins diffusing along the direction of the applied gradient will experience a different magnetic field, they will

have a different precessional frequency and therefore they will not be rephased (Fig.4).

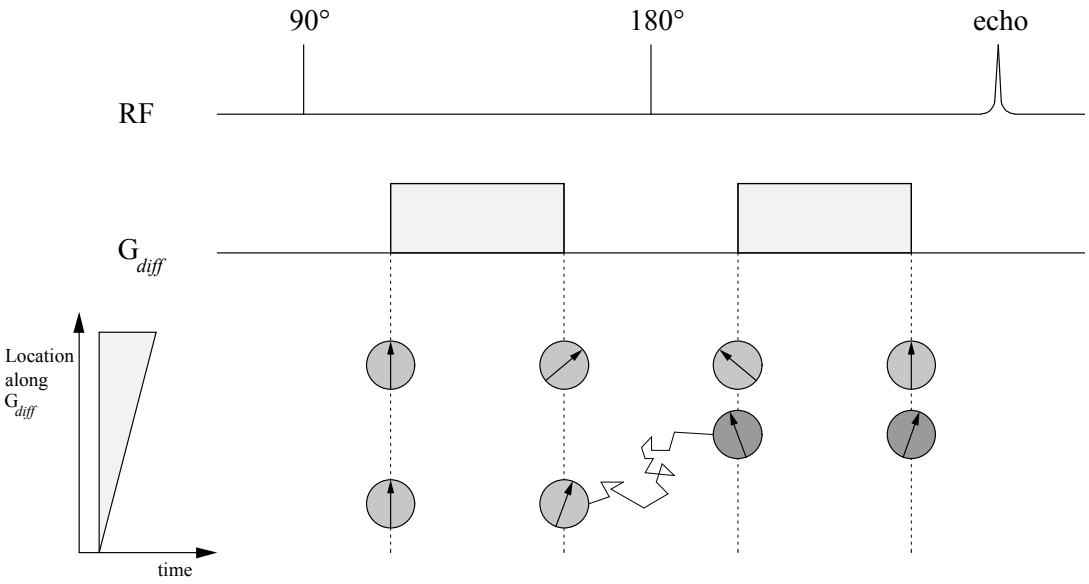

Figure 4: An illustration of phase loss due to thermal motion

This loss of transverse magnetisation results in a reduction of image signal. The attenuation of the measured signal, due to molecular diffusion for a gradient echo sequence can be described by [28, 29],

$$\frac{S}{S_0} = \exp\Big(-\frac{2}{3} D\gamma^2 G^2 \delta^3 \Big) = \exp\Big(-bD \Big) \tag{65}$$

where S_0 is the maximum signal intensity and D is the diffusion coefficient of the sample with units of $mm^2 s^{-1}$. The derivation of this equation is discussed in detail in Section F. It is clear from this expression which may be derived either from the Bloch-Torrey or Langevin equations that the degree of signal attenuation depends on the strength and duration of the applied diffusion-weighting gradients, gradient strength, G, and duration, δ, as well as the intrinsic diffusion coefficient of the water molecules in the sample. By

increasing the magnitude of G or δ, the b-value or degree of diffusion weighting of the applied imaging sequence is increased. Images with varying diffusion sensitivity are obtained by applying the diffusion-weighted sequence with a range of b-values. These images can then be combined, and an estimate of the diffusion coefficient in each voxel calculated from Eq.(65) (Fig. 5(a)). The results can be displayed as an image using a quantitative scale and thus form a map of the diffusion process throughout the sample (Fig. 5(b) & 5(c)).

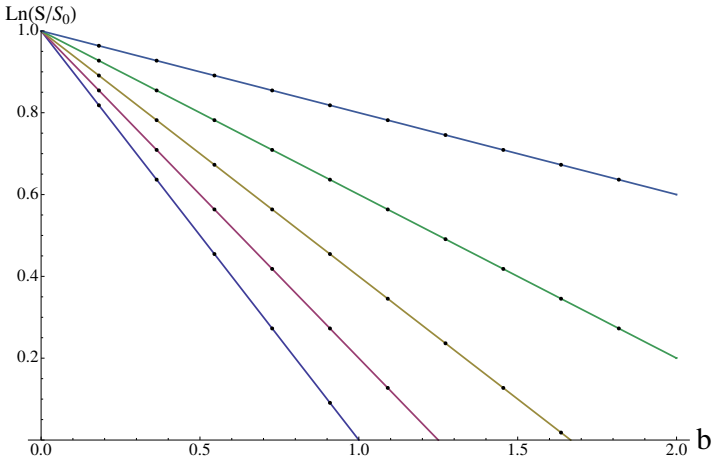

(a) Fitting a Simple Diffusion Model (e.g. Eq.(65)) to Experimental data.

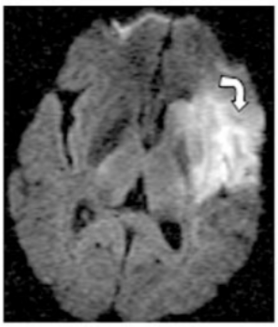

(b) Diffusion weighted image

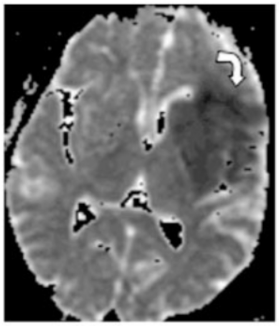

(c) ADC map

Figure 5: (a) plots of a simple diffusion decay, as might be seen in a water phantom experiment. The slope of the fitted line is the apparent diffusion coefficient. The diffusion coefficient is increasing from top to bottom fitted line.(b) reproduces a diffusion weighted image from [33] of an acute ischaemic lesion in an adult brain. (c) is an image composed of the calculated ADC's for each voxel of Fig.(b).

We remark that the use of MRI technology to encode Brownian motion is not without its own difficulties. Diffusion-weighting gradients also introduce sensitivity to other types of motion, such as bulk motion, into the imaging sequence. To eliminate the effects of bulk motion, single shot pulse sequences, such as single shot echo-planar imaging (EPI) , rapid acquisition with relaxation

enhancement (RARE) or spiral, are used [31]. The large magnetic field gradient amplitude required to achieve high b-values can induce significant eddy currents, which can cause geometric distortion in echo planar images.

Current hardware limitations mean only time averaged properties of the chemical and biological environments experienced by the water molecule during the acquisition time can be measured. Typical acquisition times are in the range of milliseconds, while fast processes such as rotational dynamics or exchange events occur on the microsecond timescale [34]. Early in the development of diffusion imaging it was suggested that the diffusion coefficient, D, should be replaced with another (statistical) parameter, the apparent diffusion coefficient (ADC) [35]. The ADC incorporates the averaging due to the experimental limitations of large voxel size (mm^3) and relatively long diffusion times.

F Evaluation of the dephasing for various gradients

Clearly, from the timing diagrams presented in Section E, the general Eq. (60) can be used to determine the effect on the signal intensity of specific experimental design parameters in gradient or spin echo experiments. For a simple bipolar gradient echo experiment with gradient strength, G, and gradient duration, τ, we easily find that from Eq.(60) that,

$$\ln \frac{S(2\tau)}{S(0)} = -D\gamma^2 \int_0^{2\tau} \left(\left[\int_0^t \mathbf{G}(t')dt' \right] \left[\int_0^t \mathbf{G}(t')dt' \right] \right) dt$$
$$\ln \frac{S(2\tau)}{S(0)} = -\frac{2}{3} D\gamma^2 G^2 \tau^3 \tag{66}$$

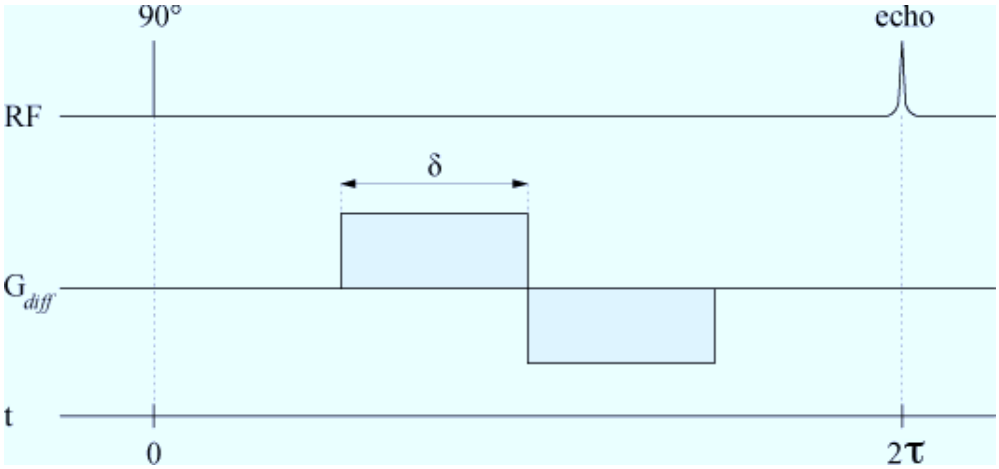

Figure 6: A timing diagram for the gradient echo experiment

The calculations for the spin-echo experiment are more involved. Stejskal and Tanner [36] further developed Eq. (60) to describe the effect of diffusive molecular motion in a spin echo experiment. Rewriting Eq. (60) in differential form and introducing the signum function, ξ, we have

$$\frac{dS}{dt} = -S.D\gamma^2\Big[F + (\xi - 1)f\Big]^2$$

$$\text{where } F(t) = \int_0^t \mathbf{G}(t')dt', \quad f = F(\tau), \quad \text{and} \quad \xi = \begin{cases} +1 & \text{for } 0 < t < \tau; \\ -1 & \text{for } t > \tau \end{cases}$$

$$\int_0^{2\tau} \frac{dS}{S} = -D\gamma^2 \int_0^{2\tau} \Big[F + (\xi - 1)f\Big]^2 dt$$

$$\ln S\Big|_0^{2\tau} = -D\gamma^2\Big[\int_0^{\tau} F^2 dt - 4f\int_{\tau}^{2\tau} F dt + 4f^2(2\tau - \tau)\Big] \tag{67}$$

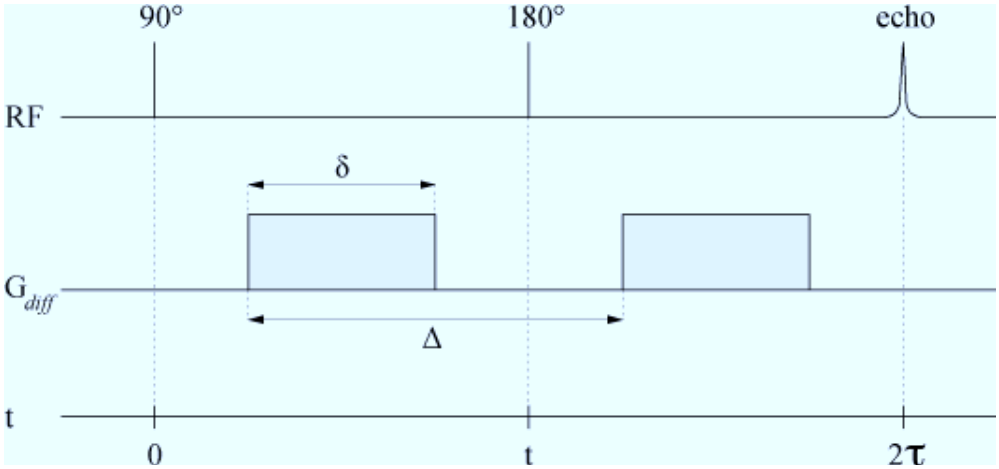

Figure 7: A timing diagram for the spin echo experiment

The expression must be calculated for each section of the gradient waveform (Fig. 7), from the application of the first diffusion weighting gradient to the echo acquisition. The phase effect is cumulative, and the state of the phase at the end of one segment must be included in the calculation for the next.

Beginning with the first term,

$$\int_0^{2\tau} F^2 dt = G^2 \int_0^{\delta} t^2 dt + (G\delta)^2 \int_{\delta}^{\Delta} dt + G^2 \int_{\Delta}^{\Delta+\delta} (t - \Delta + \delta)^2 dt + G^2 \int_{\Delta+\delta}^{2\tau} (2\delta)^2 dt$$

$$\int_0^{2\tau} F^2 dt = -\frac{1}{3} G^2 \delta^2 (7\delta + 9\Delta - 24\tau) \tag{68}$$

The remaining two terms are evaluated from τ to 2τ only. The second term can be evaluated as,

$$
\begin{aligned}
f &= F(\tau) = G\delta \\
-4f\int_{\tau}^{2\tau} F dt &= -4G\delta\Big[G\delta\int_{\tau}^{\Delta} dt + G\int_{\Delta}^{\Delta+\delta}(t-\Delta+\delta)dt + 2G\delta\int_{\Delta+\delta}^{2\tau} dt\Big] \\
-4f\int_{\tau}^{2\tau} F dt &= -4G\delta\Big[-\frac{1}{2}G\delta(\delta+2\Delta-6\tau)\Big] \\
-4f\int_{\tau}^{2\tau} F dt &= 2G^2\delta^2(\delta+2\Delta-6\tau) \qquad (69)
\end{aligned}
$$

The final term is simply,

$$4f^2\tau = 4G^2\delta^2\tau$$

These terms combine to produce the Stejskal-Tanner expression [36] for the spin echo experiment,

$$\ln\frac{S(2\tau)}{S(0)} = -D\gamma^2G^2\delta^2\big(\Delta-\frac{\delta}{3}\big) \qquad (70)$$

For gradient echo experiments with gradient shapes other than a simple rectangular gradient shape, the same technique must be applied where the phase state at the end of one integral must be taken into account in the calculation of the following integral. In the gradient echo case however, the contribution of the last two terms to the Stejskal-Tanner expression are zero. The experimental application of two other gradient configurations will be described in later chapters, and so their corresponding expressions for the reduction in magnetisation amplitude will also be outlined here.

The first was a ramped gradient configuration as illustrated in Fig. 8. The

gradient strength was increased from zero to the maximum at the beginning of the bipolar gradient, and decreased continuously, passing through the origin, to the same maximum value with the opposite polarity i.e. the gradient strength was zero at $t = \delta$. The slope of this gradient was therefore $G(t) = \frac{G}{\delta}(t - \delta)$.

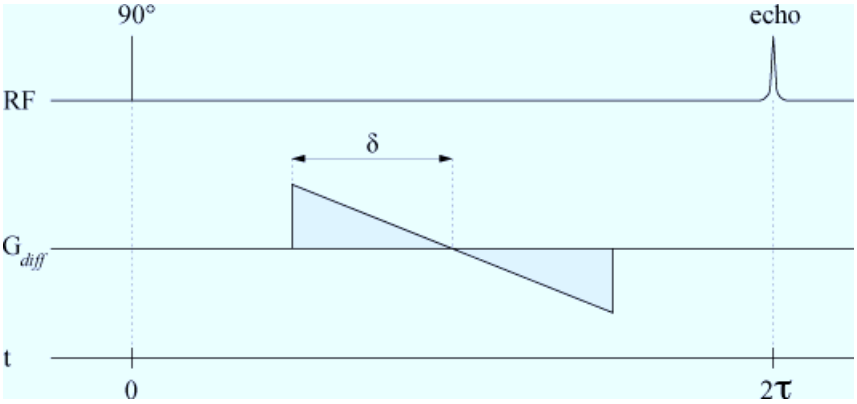

Figure 8: The ramped gradient diffusion experiment

As this is essentially one continuous gradient, the expression could be calculated using the single integral,

$$\ln \frac{S(2\delta)}{S(0)} = \int_0^{2\delta} F^2 dt = \int_0^{2\delta} \left(\int_0^t -\frac{G}{\delta}(t - \delta) dt \right)^2 dt$$
$$\ln \frac{S(2\delta)}{S(0)} = -\frac{4}{15} D\gamma^2 G^2 \delta^3 \tag{71}$$

The other gradient configuration considered used two triangular shaped gradients of opposite polarity, as shown in Fig.9. Intervals 2 and 3 are equivalent to the ramped gradient design, all intervals were of the same duration and each slope is identical.

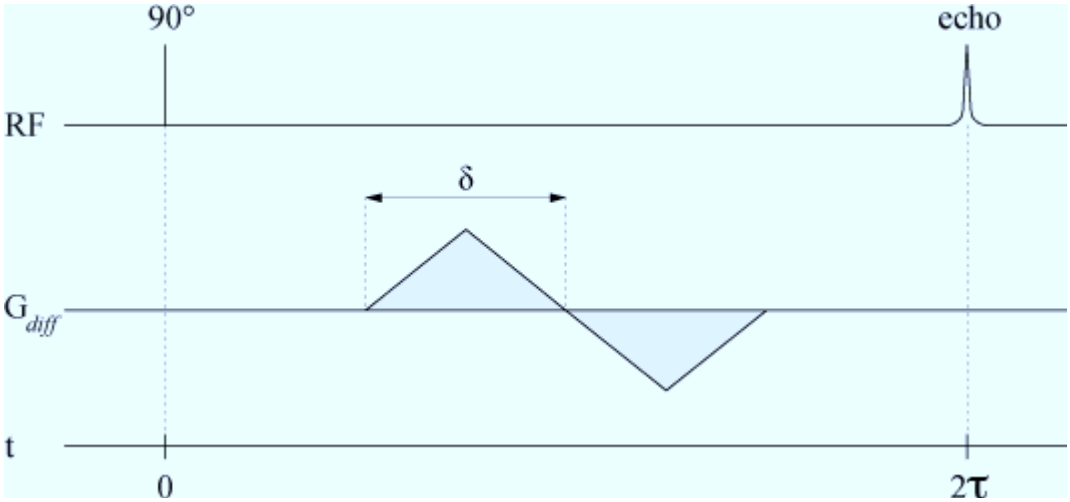

Figure 9: The diffusion experiment with triangular diffusion gradients

An equivalent expression was derived to describe the signal attenuation following the application of this gradient design.

$$\int_0^{2\delta} F^2 dt = \int_0^{\frac{\delta}{2}} \left(\frac{Gt^2}{\delta}\right)^2 dt + \int_{\frac{\delta}{2}}^{\delta} \left(G\big(2t - \frac{t^2}{\delta} - \frac{3\delta}{4}\big) + \frac{G\delta}{4}\right)^2 dt + \int_{\delta}^{\frac{3\delta}{2}} \left(G\big(3t - \frac{t^2}{\delta} - 2\delta\big) + \frac{G\delta}{4}\right)^2 dt + \int_{\frac{3\delta}{2}}^{2\delta} \left(G\big(\frac{t^2}{\delta} - 4t + \frac{15\delta}{4}\big) + \frac{G\delta}{4}\right)^2 dt \tag{72}$$

that is

$$\int_0^{2\delta} F^2 dt = -\frac{23}{120} D\gamma^2 G^2 \delta^3 \tag{73}$$

G Summary of the preceding classical results

We have seen in Sections C and D that the Bloch equations as originally formulated [10, 26] ignore the Brownian motion of the liquid nuclei and that numerous attempts to incorporate this phenomenon in them have been made

[11, 37], one of the best-known being that of Carr and Purcell [29] leading *inter alia* to Eqs (61) and (65). Their treatment (effectively Einstein's theory of the Brownian motion [14, 18] adapted to the phase variable $\Delta\Phi$ above) is based on the notion that a nucleus executes a discrete-time random walk. The walk is due to the cumulative effect of very large numbers of impacts of the surrounding particles on a nucleus, so that the fluctuating displacement $\mathbf{r}(t)$ and thus the phase is a sum of random variables each having arbitrary distributions. In other words, the random walker executes a *discrete* jump of *finite* jump-length variance in a *fixed* time interval, (i.e., the elementary steps of the walk are taken at *uniform* intervals in time to one of the *nearest* neighbour sites), so that the only random variable is the direction of the walker. The direction of the jump-length vector [18], has finite variance and the waiting time between jumps has a finite mean. The problem is always to find the probability that the walker will be in state n at some time t, given that it was in a state m at some earlier time, giving rise in general to a difference equation [13, 15, 16]. However, by the central limit theorem [18] (since one is dealing with a sum of centred random variables each having arbitrary distributions), the dephasing effect due to the Brownian motion may be calculated explicitly in the continuum limit of extremely small mean square displacements, in infinitesimally short times. In such a process, any jump-length distribution of *finite* jump-length variance and any jump-time, distribution with *finite* average jump-time will (in the continuum limit of a very large number of small steps of short duration) as a consequence of the central limit theorem, give rise to the same dephasing effect.

We have also seen that the above analysis was later much simplified by Torrey [28]. He avoided the problem, encountered by Carr and Purcell [29], of explicitly passing to the continuum limit of the discrete time random walk by

simply adding (adapting a method originally described by Einstein, see Ref. [18], Ch. 1) a magnetisation diffusion term to the transverse magnetisation in the Bloch equations, resulting in a partial differential equation. Boundary conditions may also be incorporated in this equation allowing one to study phase diffusion in a confined space [30]. The Bloch-Torrey equation may be easily solved [28, 38] for nuclei diffusing freely in an infinite reservoir (Section F). Thus he obtained the following expression for the dephasing following the application of a step gradient of magnitude G in a liquid characterised by a diffusion coefficient D

$$\langle e^{i\Delta\Phi}\rangle = \frac{S(t)}{S(0)} = \exp\Big[-\frac{1}{3}D\gamma^2G^2t^3\Big] \tag{74}$$

Proceeding for a simple bipolar gradient echo experiment with gradients of strength G and duration δ, the expression becomes,

$$\langle e^{i\Delta\Phi}\rangle_{GE} = \frac{S(2\delta)}{S(0)} = \exp\Big[-\frac{2}{3}D\gamma^2G^2\delta^3\Big] \tag{75}$$

We have also seen that the spin echo diffusion experiment case is slightly different [36], as the second gradient pulse has the effect of resetting the dephasing caused by the first pulse. By applying the 180^o pulse in the spin echo experiment, the phase is reset by double the extent to which it was advanced [18] so that,

$$\langle e^{i\Delta\Phi}\rangle_{SE} = \exp\Big[-D\gamma^2G^2\delta^2\Big(\Delta-\frac{1}{3}\delta\Big)\Big] = \exp\big[-bD\big] \tag{76}$$

Once again in Eq.(76), δ is the gradient spacing and Δ is the time interval from the starting time of the first gradient to the starting time of the rephasing gradient. The notation $b = \gamma^2 G^2 \delta^2 (\Delta - \delta/3)$ is traditionally used as in Eq.(76) for simplification, and the degree of diffusion weighting in an MRI acquisition is set using a b-value. The diffusion weighting or b-value is increased, typically by increasing the strength of the diffusion-weighting gradient, G.

Now Eqs. (74)-(76) describe precisely the signal loss due to the translational motion of the magnetic moments in unrestricted (free) water in a magnetic resonance experiment. However, we have already seen that difficulties arise when these equations are applied *in vivo*, because these simple single exponential equations fail to describe the diffusion of water in tissue. This added complexity of the signal decay in tissue is capable of characterisation which could improve sensitivity and specificity in the detection of diseases of the brain [39] and functional activation [40]. A number of empirical fitting functions (models) have been developed by various groups in an attempt to exploit these complex experimental findings which we shall now discuss.

H Deviations from exponential decay

The Biexponential Model

Once the development of the gradient hardware and sequence design allowed b-values greater than 1000 smm^{-2} to be attained experimentally, it became apparent that the diffusion decay was not monoexponential with cubic time at high b-values. An empirical approach to this problem has been to assume that fast and slow diffusion components exist [41] so that the decay may be described by the simple equation

$$\frac{S(t)}{S(0)} = V_1 e^{-bD_1} + V_2 e^{-bD_2} \tag{77}$$

Here V_1 and V_2 are considered as the volume fractions of protons in fast and slow diffusing pools within neuronal structures, with the distinct diffusion coefficients D_1 and D_2. Once again b contains the experimental parameters $\gamma^2 G^2 \delta^2 (\Delta - \delta/3)$. This equation, which is useful in practice [41, 42, 43, 44], has a simple theoretical explanation, namely, that the signal from two separate compartments is the sum of the signals from each compartment (although this statement should be regarded as approximate because of the presence of a boundary). The diffusion coefficients are thought to correspond to two compartments in slow exchange, one with a fast and one with a slow diffusion coefficient. The relative volume of each pool and their corresponding diffusion coefficients, have been consistently reported by many groups [42, 44, 45] to be 0.7/0.3 for the fast/slow diffusing pools, with corresponding diffusion coefficients of 1.3/0.3 $mm^2 s^{-1}$.

Neindorf *et al.* [41] performed diffusion weighted experiments in the rat brain with b-values up to 10,000 smm^2. The possibility of other causes for the observed non-monoexponential behaviour, such as internal gradients due to cross-terms, partial volume effects, vascular contributions, echo time (TE) dependence and diffusion time dependence, were eliminated experimentally in this study. It was thought that the fast and slow diffusing pools might correspond to the intracellular and extracellular compartments, where diffusion is expected to be faster in the extracellular compartment due to lower viscosity. However the volume fractions as noted above do not correspond to the known volume fractions for intra- and extracellular water, as intracellular water is known to account for $> 80\%$ of the total water volume. The magnitude of

the volume fractions changes in ischaemic tissue, as the space occupied by intracellular and extracellular water changes during cell swelling. It remains impossible however to assign the slow and fast diffusing pools to intracellular and extracellular compartments [39]. It is now widely accepted that biexponential behaviour can be observed in the intracellular environment independently [46, 47, 48, 49].

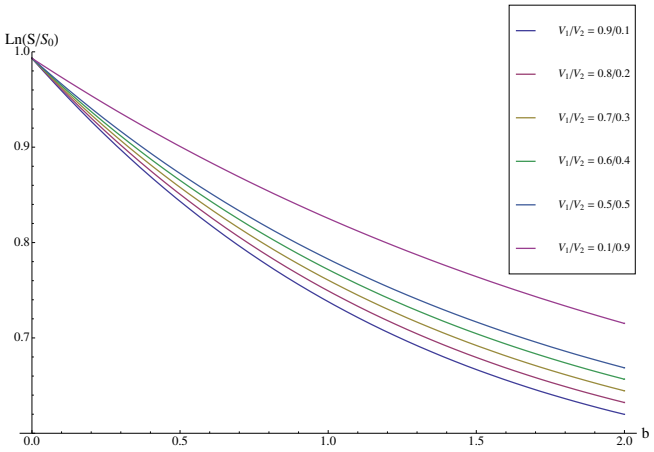

(a) Varying Volume Ratios

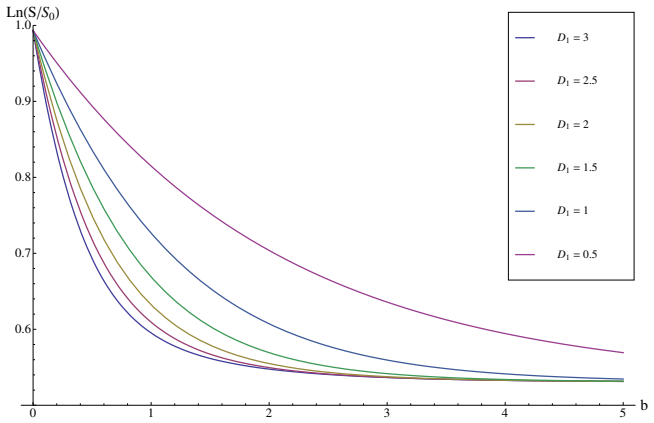

(b) Varying the value of the 1^{st} Diffusion Coefficient

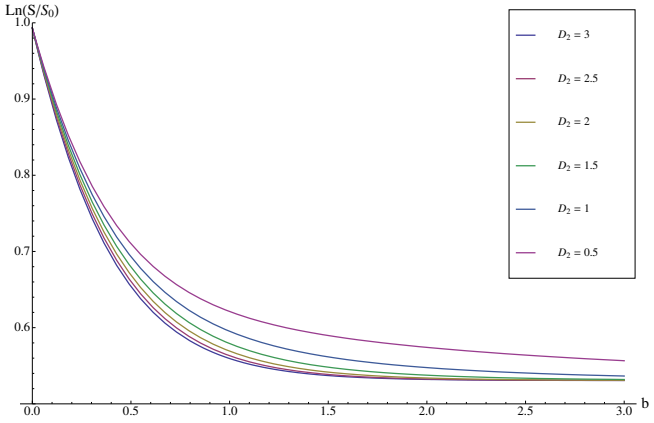

(c) Varying the value of the 2^{nd} Diffusion Coefficient

Figure 10: These plots show how varying the parameters V_1/V_2, D_1 and D_2 from the biexponential model $\left(\frac{A(t)}{A(0)} = V_1 e^{-bD_1} + V_2 e^{-bD_2}\right)$ influence the shape of the decay curve. The normalised signal intensity is plotted against the b-value.

A Statistical Model of Yablonskiy

The simplest and most logical extension of the Stejskal and Tanner expression Eq.(76), to account for the non-monoexponential behaviour observed in human neuronal tissue, resulted in the biexponential model above. While this expression contains *two* discrete diffusion coefficients, the majority of alternative fitting functions which have been proposed in the literature to date, suppose instead a distribution of diffusion coefficients. This hypothesis was clearly described by Yablonskiy *et al.* [50], when they proposed their "statistical model". These models i.e. empirical fitting functions, assume that the image signal from any voxel will originate from a variety of cells, and intracellular and extracellular spaces. The detected MR signal is the sum of contributions from groups of protons in different locations within the voxel, and each group will have a characteristic apparent diffusion coefficient. In the statistical model the signal decay is written as (in their notation),

$$S = S_0 \int_0^\infty P(D) \exp(-bD) dD \tag{78}$$

where $P(D)$ is the distribution function of the apparent diffusion coefficient which is defined using a Gaussian-like function,

$$\begin{aligned} P(D) &= B \exp\big[- \frac{(D - ADC)^2}{2\sigma^2} \big] \qquad \text{for } D > 0, \\ P(D) &= 0 \qquad\qquad\qquad\qquad\qquad\quad \text{for } D < 0 \end{aligned} \tag{79}$$

where B is a normalisation constant, the apparent diffusion coefficient (ADC) corresponds to the position of the distribution peak, and σ is its width.

Eq (78) and Eq. (79) then yield,

$$S = S_0 \exp\left(-bADC + \frac{1}{2}\sigma^2 b^2 \right) \tag{80}$$

Yablonskiy *et al.* found that this expression fitted experimental data from the human brain well, although the second parameter, the distribution width, σ, was not sensitive to different tissue types within the brain. Thus the potential benefit in using this model must simply arise from the possibility of measuring the ADC more accurately for each voxel.

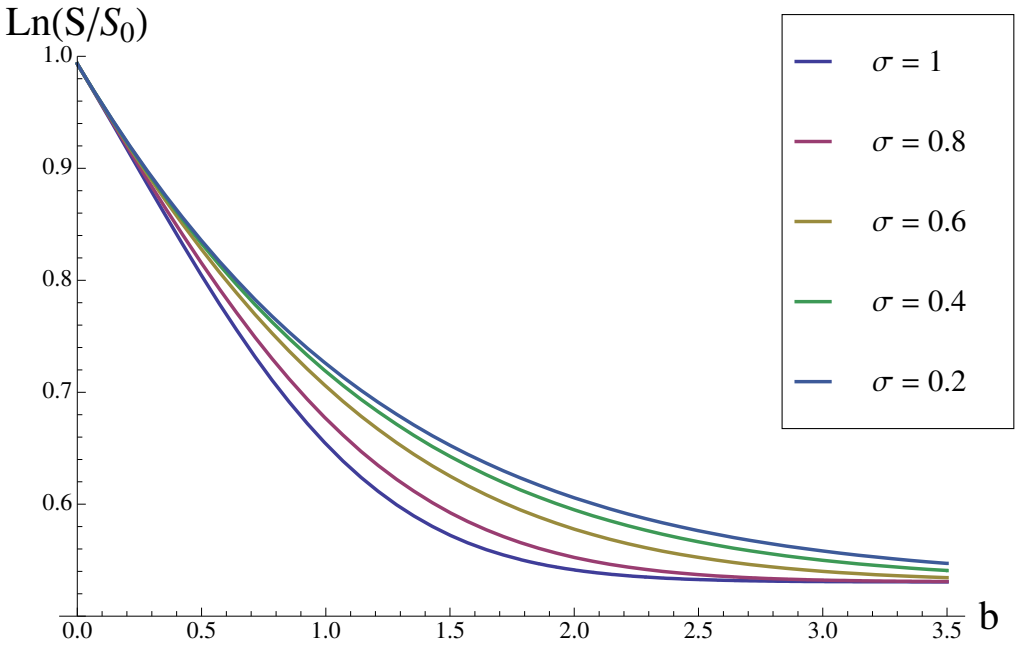

Figure 11: The statistical model

A Kurtosis Model

A method to quantify diffusion kurtosis in tissue using DWI was first proposed by Jensen *et al.* [51]. The aim was to measure the degree to which water

diffusion was non-Gaussian. Their fitting function, which is very similar to that presented later by Kiselev *et al.* [52], and like the statistical model of Yablonskiy [50], has only two fitting parameters compared to the biexponential model's four. They begin by writing $S = S_0 \exp(-bD)$, as a b^2 cumulant expansion, and truncated the expansion at the second term, leaving the quadratic function,

$$\ln S = \ln S_0 - bADC + \Big(\frac{K_{apparent} ADC^2}{6}\Big) b^2 + ... \tag{81}$$

where K is the apparent "kurtosis excess" factor and is a measure of the peakedness of a distribution. Kiselev explored the goodness-of-fit of this kurtosis model and the biexponential model in human brain diffusion data. The decay curves examined were grey matter, white matter, cerebrospinal fluid (CSF) and partial volume voxels, presumed to contain both grey matter and CSF. In grey matter the kurtosis model fits as accurately as the biexponential model, but the added parameters of the latter were required in order to best fit the voxels containing white matter and partial volume. The Authors did not include a study of directional dependence. In the earlier study of Jensen *et al.*, when three diffusion directions were applied, the diffusional kurtosis excess was found to be significantly higher in white matter than in grey matter. The Authors conjectured that this difference reflects the structural differences between the tissue types [51]. More recently, diffusion kurtosis imaging has been used to achieve increased sensitivity and directional specificity to microstructural changes associated with brain maturation in the rat [53], and to increased sensitivity to fibre directions in DTI.

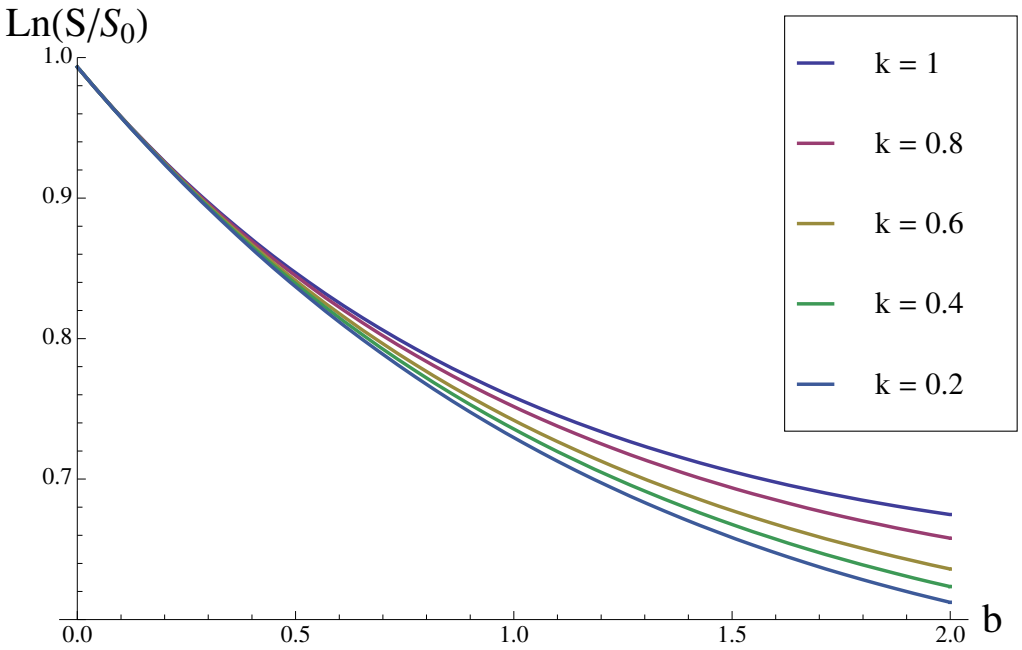

Figure 12: These plots of the kurtosis model show how the shape of the decay curves change with incremental steps of k.

The Stretched Exponential Model

Yet another approach is that of Bennett *et al.* [40], who showed that the stretched-exponential expression or Kohlrausch-Williams-Watts [54] form

$$\frac{S(t)}{S(0)} = \exp\big(-(bD_{DC})^{\alpha}\big) \tag{82}$$

where $\alpha \leq 1$ is the stretch parameter,and D_{DC} is the distributed diffusion coefficient arising from fitting Eq.(82) to data. The Authors suggest that fractional parameter α could be used to measure heterogeneity of the dephasing process in tissue which appears to exhibit anomalous diffusion behaviour, signified by a mean square displacement of the form t^{α}. In general, we saw that

the motion can be either subdiffusive ($\alpha < 1$) which signifies a slow relaxation process or superdiffusive ($\alpha > 1$) which leads to turbulence. Whereas the biexponential model has its basis in two proton pools, one fast and one slow, the stretched exponential model expects a "multiplicity of pools"[40]. It has a reduced number of parameters, just two, compared to the four fitting parameters of the biexponential model . The effect of the stretching parameter, α can be observed in Fig.12.

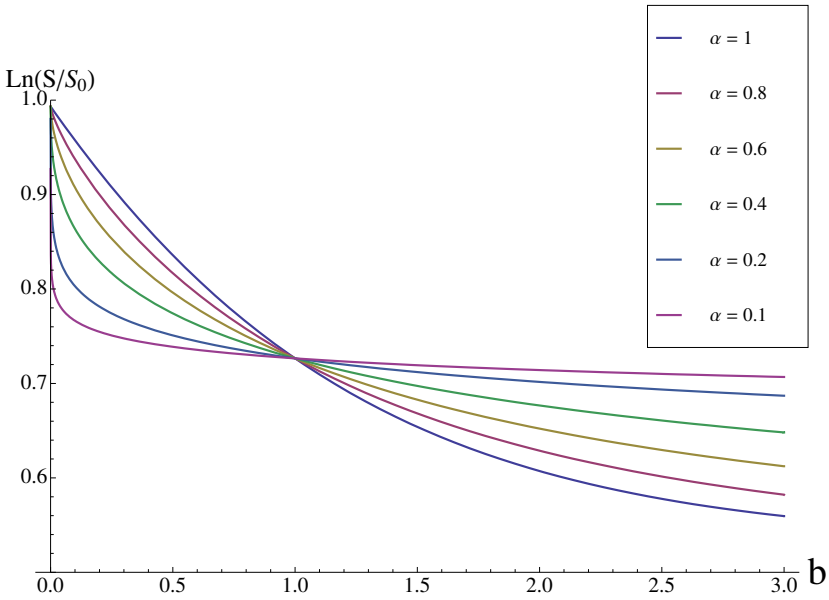

Figure 13: These plots of the stretched exponential model show how the shape of the decay curves change with incremental steps of α.

If the term $b \times D_{DC} > 1$, then the signal attenuation as a function of b-value decreases as α decreases. Conversely, when $b \times D_{DC} > 1$, lower values of α result in faster signal decay. The stretching parameter α is most effective at high values of b, where it slows the signal decay, implying that a diverse range of diffusion rates are present.

When the model was applied to free-diffusing protons in an ethanol phantom,

the value of α was close to one. However in the cerebral cortex of the rat, it was found to be significantly less. The Authors suggest that higher moments of the distribution of diffusion coefficients may have their origins in the cellular microenvironment. The concept of a distribution of diffusion coefficients is a very attractive one, given the averaged nature of the signal from each image voxel, which by necessity must contain a wide range of cell types and structures. While the so-called "heterogeneity index", α, appears insensitive to applied diffusion gradient direction [55], a more comprehensive diffusion measurement, the D_{DC} could facilitate improved fibre tracking in DTI [56].

Hall *et al.* [56], developed the stretched exponential model by introducing the hypothesis that the stretch parameter, is related to the fractal nature of the movement of the diffusing spins and therefore the complexity of the tissue environment. They related their stretching parameter to the fractal dimension and thus linked this model to the concept of anomalous diffusion.

An Anomalous Diffusion Model

One of the first experiments to measure anomalous diffusion in tissue using magnetic resonance methods was that by Özarslan *et al* [57]. Q-space spectroscopy data was obtained from human red blood cell ghosts, tissue from a human grade-4 astrocytoma and a human erythrocyte ghost model. Using a simple model which describes anomalous diffusion in disordered media, they found that water diffusion in the human tissue samples was anomalous, i.e. that the mean-square displacements varied more slowly than linearly with time.

Another group, Magin *et al.* [38], developed the idea of applying fractional diffusion in a phenomenological manner to the diffusion decay observed with DWI. Beginning with the Bloch-Torrey equation (Eq.(56)) [28], by simply

replacing $\frac{\partial M_\perp}{\partial t}$ and $\bigtriangledown^2 M_\perp$ by fractional time and space derivatives respectively (c.f. Eq 8 of their paper), they transformed it into a fractional order form. Hence they derived two functions, one which is fractional in space, and the other fractional in time. Their expression for diffusion decay due to fractional order dynamics in space, for the Stejskal-Tanner experiment, is their Eq. 16c

$$S(t) = S_0 \exp\left[- D\mu^{2(\beta-1)} \left(\gamma G_z \delta\right)^{2\beta} \left(\Delta - \frac{2\beta - 1}{2\beta + 1}\delta \right) \right] \tag{83}$$

where μ is a fractional order space constant, required to preserve units, and β is the order of the fractional spatial derivative and constrained to the values $(1/2 < \beta \leq 1)$.

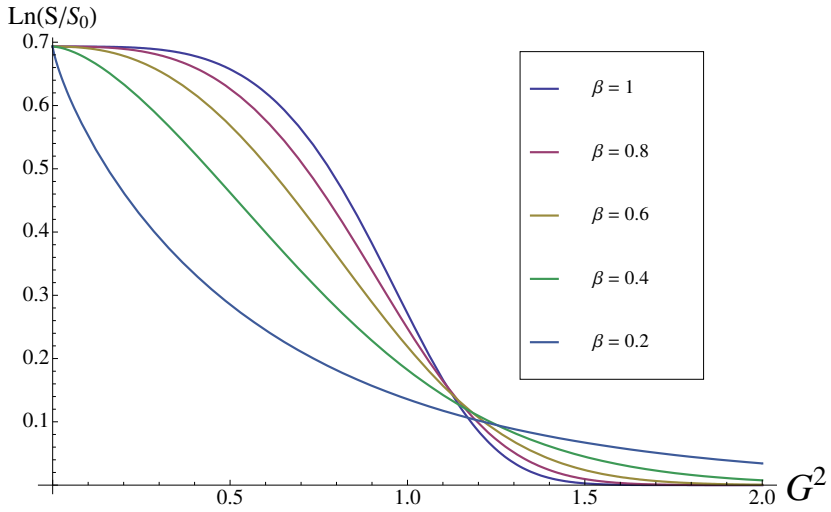

Figure 14: Plots of the fractional order model Eq.(83), with varying β.

Experimental data was acquired by the Authors in phantoms, human cartilage *in vitro*, and human brain *in vivo*. The diffusion coefficients calculated by fitting with the anomalous diffusion model above, were almost identical to those produced by fitting with the monoexponential function, $S = S_0 \exp[-bD]$.

The novel information was therefore provided by the other parameters, β and μ. As expected when the diffusion decay deviated from monoexponential behaviour, the values of β were found to be less than one.

Although an expression for the fractional order dynamics in time was derived, it was not investigated experimentally. For a constant field gradient, as considered by Carr and Purcell, the fractional time expression was given as,

$$S(t) = S_0 E_\alpha \left[-i\gamma G_z z \tau \left(\frac{t}{\tau}\right)^\alpha \right] \exp\left[-B\left(\frac{t}{\tau}\right)^{3\alpha} \right] \tag{84}$$

$$\text{where} \quad B = \frac{2\Gamma(2-\alpha) D \gamma^2 G_z^2 \tau^3}{3\alpha^2 \Gamma(2\alpha+1)}$$

Here the parameter τ is used simply to preserve units and E_α is the Mittag-Leffler function defined in Eq (25) [18, 58].

I Diffusion in Biological Tissue

Water is the primary constituent in living cells, providing both liquid support and creating the solvent environment for the majority of biochemical reactions [34]. Many pathologies lead to changes in water homeostasis, causing a buildup of intracellular ions and water, and subsequently cell swelling. Furthermore, observations suggest that changes in cell and organelle volume, which are directly linked to water homeostasis, play an important regulatory role in various aspects of cellular metabolism [59].

The metabolism of water in cells is a cyclical process. Water molecules can pass through the plasma membrane via two routes; diffusion across the phospholipid bilayer, or diffusion through water channels (aquaporins). Once carried into the cell it diffuses through the cytoplasm reaching various subcellular organelles such as mitochondria, nucleus and endoplasmic reticulum. The

water molecules can be transported inside these subcellular structures through further lipid bilayers or pores. While present in the intracellular space, water forms the fluid support for translational diffusion of biomolecules and is engaged in many exchange reactions with macromolecules or metabolites. Eventually, the cytosolic water molecules leave the subcellular organelle and the cell, employing the same transport mechanisms as used to enter it. Water transport is thought to be passive, reversible and directed by the osmotic gradient across the cellular membranes [34].

The diffusion of water molecules is well described for bulk water, which is a simple homogeneous system. The diffusion coefficient of cellular water is much reduced compared to the diffusion coefficient of bulk water. Diffusion coefficients measured using magnetic resonance methods are averaged measurements of the cellular water. Water which is bound to biomolecules dominates measurements of T_1 and T_2 relaxation times, whereas free cellular water dominates the measurement of diffusion coefficients. There are a number of factors which are thought to contribute to the reduction in the diffusion coefficient which is observed in biological tissue. The random walks of water molecules are hindered as they encounter macromolecules, organelles, cell membranes and other cellular and subcellular structures.

A diffusing particle in the living cell experiences a combination of forces that determine its characteristic motion. Collisions with solute and solvent molecules and other interactions modulate the path of such a biomolecule until it appears at first to behave as a Brownian particle [60]. Diffusion is a most efficient method of mixing, as without the expenditure of energy, it causes dispersion of the biomolecules throughout the available space. The mobility of a biomolecule limits its ability to participate in cellular interactions.

Diffusion is particularly critical in neuronal cells, and consequently in brain function. Although brain cells are densely packed, there is a small extracellular space between each cell membrane. The extracellular space comprises approximately 20% of the total volume of the brain [61]. The extracellular space is similar to the water phase of a foam and many substances are mobile within this complex region [62]. The most important role of the brain extracellular space is to facilitate the diffusion of nutrients for metabolism, such as glucose and oxygen, from the vasculature to the neuronal cells. Diffusive transport also facilitates volume transmission and is crucial in the delivery of many therapies that deliver pharmaceuticals to the brain. The distribution of observable molecules due to diffusion can be used to illustrate the structure of brain tissue. The structure has both volume fraction (empty space) and tortuosity characteristics (restricted diffusion due to local barriers or local viscosity). The cell cytoplasm is currently thought to form a gel-like structure through which pass a mesh of contractile filaments made of actin, tubulin and other proteins of the cytoskeleton [34, 63]. The major cytoskeleton networks are constructed of filamentous actin (F-actin) and microtubules. These form distinct while interconnected intracellular networks. F-actin is thought to maintain cellular shape and generate contractile forces. Microtubules provide additional mechanical rigidity, however they also form tracks along which motor proteins can travel, by converting chemical energy in the form of (adenosine-triphosphate) ATP into mechanical work.

The reduction of the water diffusion coefficient in tissue is not thought to be caused by the presence of cell membranes. The plasma membrane is so permeable that diffusion is not restricted. The obstruction caused by large molecules and subcellular organelles is thought to increase the diffusive

path length. Water molecules which are bound to macromolcules or other structures must also be considered, as these contribute to image signal, but are not free to diffuse. The characteristics of many subcellular structures are presumed to affect the motility of a significant fraction of the water. Three factors are thought to influence intracellular diffusion; fluid viscosity, binding to macromolecules and collisions between solutes and macromolecules. García-Pérez *et al.* [64] investigated the influence of molecular crowding and viscosity on the translational motion of metabolites in subcellular organelles using a pulsed gradient spin echo (PGSE) NMR technique. Their results indicated that the concentration of molecules of a similar size to the metabolites under study, had the greatest influence on their observed diffusion coefficients. These results could be explained by an intracellular environment more crowded, but not more viscous than the extracellular environment. Large static cellular structures did not significantly hinder the translational diffusion of water, but are found to obstruct the movement of larger biomolecules.

J Anomalous Diffusion in Tissue

As discussed in Section A of this chapter, in systems where particles or molecules diffuse freely via Brownian dynamics, the mean-square displacement of the particles is proportional to time. With more complex architecture, such as within living cells, diffusion may be hindered by various factors, such as interactions with obstacles, transient binding events or molecular crowding [65]. In such environments the motion of the molecules is often anomalous, with a distribution of diffusion times, and the mean square displacement does not therefore increase linearly with time.

Searching for a specific target is a universal process in living systems, and

this ranges from the macroscopic field of zoology (e.g. prey-predator), to the microscopic requirement for macromolecular binding in living cells [66]. It is assumed that the random encounter rate of two interacting bodies is determined by Brownian motion. The searching inside a living cell however is governed by both normal diffusion and subdiffusion. Indeed we have seen that subdiffusion is characterised a by mean-square displacement that grows like $\langle x^2(t)\rangle \sim t^\alpha$, $0 < \alpha < 1$, i.e. a slower spreading than for normal diffusion is observed due to the exponent $\alpha < 1$. Guigas and Weiss [67, 68] have shown, using fluorescence correlation spectroscopy, that diffusion in the cytoplasm and the nucleus of eukaryotic cells is subdiffusive, with values of α in the range 0.5-0.85. Golding found similar behaviour for bacteria [69]. The origin of the subdiffusive behaviour appears to arise from molecular crowding. Crowding in cells is thought to influence not only protein and nucleic acid diffusion, but also molecular recognition, protein assembly and protein folding [70]. A slow sampling process is implied by the slower spreading associated with subdiffusion. Molecules remain at their original position for a longer time. Using simulations to determine the probability of finding a molecular binding partner by diffusion, Guigas *et al.* [66] concluded that for an infinite search time anomalous subdiffusion is the optimum search strategy. While anomalous subdiffusion ($\alpha < 1$) is slower than normal diffusion ($\alpha = 1$), it is not slow enough to prevent the occurrence of biochemical reactions. In addition, due to its fractal nature, the subdiffusive random walk causes a particle to traverse (search) the available space most thoroughly. The anomalous diffusion exponent α is found to decrease continuously with increasing concentrations of obstacles and increasing molecular weight [70, 71].

Fluorescence correlation spectroscopy (FCS) is an optical method which

measures concentration fluctuations of molecules on a very short timescale. FCS detects fluorescence intensity fluctuations from a microscopic illuminated volume containing only a small number of fluorochrome molecules (a femtolitre or less) [72]. The molecules travel across the observed volume due to Brownian motion, and this leads to changes in detected fluorescence. The other source of variation in measured fluorescence is the switching of the fluorophore from its fluorescent to non-fluorescent state. Through the application of time correlation analysis, both the hydrodynamic and photophysical properties of the molecules can be assessed. As for diffusion MRI data, there is considerable debate concerning the analysis of FCS data, including the choice of mathematical model. The most commonly used model assumes a power law scaling as quoted in the previous paragraph and Eq. (87) below. Hypothetical mechanisms for this anomalous behaviour include corralling, immobile obstacles and binding with a distribution of binding durations. An alternative is the two component model, where one fraction of the sample molecules undergoes free Brownian motion with a diffusion coefficient approximately five times smaller than in bulk solution, and the second fraction diffuses one or two orders of magnitude slower.

Anomalous diffusion has been detected in biological tissue using a fringe field NMR technique [73]. Field gradients in the usual pulsed gradient stimulated echo method are relatively small, and as a result the corresponding observable length scale exceeds cellular dimensions. The influence of cellular structure may be approximated by solutions of the diffusion equation with boundary conditions. The field gradient in the superconducting fringe field method exceeds the field gradient of the pulsed-gradient stimulated-echo method by orders of magnitude, which leads to length scales within cellular regions. The

diffusion resolution of this method is approximately 1 to 15 μm. The term resolution implies the mean-squared distance a molecule must move to sense the gradient spatial encoding. The fringe field method was first developed by Kimmich *et al.* [74], to avoid some of the drawbacks encountered when large field gradients are applied in standard NMR experiments, such as heating, eddy currents and vibrations.

Fringe field diffusion measurements can be performed with a stimulated echo sequence with similar principles to pulsed-field gradient NMR experiments. Köpf *et al.* [75] used a 9.4T superconducting magnet with a bore of 9cm. At 26cm axial distance from the centre of the bore the magnetic flux density was 3.9T (giving a proton Larmor frequency of 162MHz), while the field gradient is at its maximum value of 50T/m. This gradient is almost constant over 2cm. A disadvantage of this method is that as the gradient is constant over such a large area, only the echo amplitude is recorded [76] and the spatial resolution is entirely lost. Thus all structural information is lost and distinction between the resonances of ^{1}H and ^{19}F is impossible. There is also the problem that the available RF pulses can excite only a thin slice of a sample in a strong gradient field. Therefore, the ensemble averaged mean square displacement can be measured, and while it is assumed to be moving along the contour of microscopic structure on a cellular length scale, it is not possible to be certain that the measured displacement is the actual displacement [75].

Köpf and Nonnenmacher [73, 75] performed fringe field experiments on a number of different tissue types, and discussed the use of three relaxation functions to describe the diffusion process therein. The functions they observed are of the form of the Debye and Kohlrausch-Williams-Watts (KWW) relations and a power law decay.

$$E = \exp(-Db) \qquad \text{(Debye)} \tag{85}$$

$$E = \exp -(Db)^{\alpha} \qquad \text{(KWW)} \tag{86}$$

$$E \sim (q^2)^{-\mu} \qquad \text{(Power Law)} \tag{87}$$

where D is the diffusion coefficient and,

$$b = 4\pi^2 q^2 T$$

q is a wave vector which describes the length scale, and T is the time scale of the measurement. α is again the anomalous exponent, with a range $0 < \alpha < 1$, while μ involves the fractal dimension of the underlying geometry and has values $\mu > 1$. Köpf *et al.* found that the observed relaxation function varied for short, intermediate and long time scales, and also for cellular structure. Pure fluids and fatty tissue are well described by a Debye relaxation function. Fatty tissue displays a low degree of compartmentation and few small cellular details. Glandular and fibrous tissues are more structured and crowded. Their diffusion process exhibits Debye relaxation only at very short times, due to contributions from free cellular water. At longer times, a combination of Eq. (85) and Eq. (86) is required to describe the relaxation,

$$E = C_1 \exp(-Db) + C_2 \exp(-Db)^{\alpha}. \tag{88}$$

At long times, the power law decay is the most suitable description of the diffusion and would seem to be consistent with the fractal time random walk picture of Section B above. This time dependence can be interpreted as follows:

for short diffusion times, T, there is not sufficient time for the water molecules to probe the cellular structure, so the diffusion relaxation has a Debye form [73]. At longer times, larger mean square displacements are superpositions of smaller ones, and it is this distribution function which is measured. Tumour tissue has similar characteristics to fibrous and glandular tissue, being highly structured. It has an irregular cell form, a higher rate of mitosis and a higher nucleus to plasma ratio. The similarities of structure between tumour and healthy tissue frustrate attempts to perform differentiation using this method.

K Applications of DWI

Changes in tissue water diffusion usually result from alterations or injuries to the circulation and blood brain barrier, as in ischemic stroke [77, 78, 79]. Diffusion behaviour is also modified by vasogenic, cytotoxic edema and breakdown of physiologic myelination. Acute ischemic stroke has been the most successful application of DWI, but infectious and inflammatory conditions as well as intracranial masses, epilepsy, white matter abnormalities, degenerative diseases and haemorrhage are also the subject of research with DWI [78]. Numerous pathologies involve a local or global increase in tissue water content. For example hepatic encephalopathy results in the formation of a cerebral oedema with water content changes of 1–3%, while white matter tumours can show an increase in excess of 20% [80]. Therefore measurement of changes in water content or local environment is of diagnostic value, and potentially useful for the monitoring of therapies.

Stroke

The clinical potential of diffusion-weighted magnetic resonance imaging (DW-MRI) in vivo became recognised when Moseley *et al.* [5] discovered, in animal experiments, that ischaemic stroke lesions in the acute phase could be visualised on the basis of a reduced apparent diffusion coefficient (ADC). This ADC reduction persists even in the sub-acute phase, for up to 7-16 days according to patient studies [79]. Today, DW-MRI of patients with ischaemic stroke is a well-established technique, valuable for prognosis and treatment in the acute as well as in the sub-acute stage. While the pathological process of an ischaemic lesion is relatively well understood, the biophysical mechanisms responsible for the reduction in ADC on a microstructural level remain somewhat unclear [81]. Hypotheses suggested to explain the reduction of the ADC include, for example, (i) an influx of fast diffusing extracellular water into the intracellular space [82], (ii) an increased tortuosity in the extracellular space [83], (iii) shrinking of neurons [84] or (iv) a failure of high energy dependent microcirculation (cytoplasmic streaming) [85]. Although the specific biophysical mechanisms in the proposed hypotheses differ, they are all based on the assumption that the ADCs are different in the intra- and extracellular spaces. This two-compartment (i.e. biexponential model Section H) interpretation of DW-MRI experiments was earlier suggested by Niendorf *et al.* [41]. Using very high diffusion sensitivities, a double-exponential relationship of the signal-versus-b curve was observed in rats, with one fast and one slow diffusion component.

Recent work by Lätt *et al.* [86] investigated the dependence on the diffusion time of a plot of image signal with b-value, based on the assumption that the curves originate from different compartments. This time-dependence should

be due to restricted diffusion within the compartments and/or water exchange between them through permeable membranes. Their study showed that the signal versus b curves in sub-acute ischaemic lesions show a diffusion time (T_D) dependence, as measured with a clinical MRI scanner. They conjecture that the observed signal curve split up (a reduced normalised signal intensity at the longer T_D) is an effect of exchange between different water pools with different ADCs. A similar result was observed by Pfeuffer *et al.* [87] in the rat brain in vivo.

[88] DWI has been extensively used to detect acute ischaemic brain injury much earlier after onset of the ischaemic injury than conventional MRI is capable of. It makes it possible to distinguish acute from chronic ischaemic changes, which may have an impact on treatment. In the acute phase, ADC are initially reduced by 30-50% within 30 min of the onset of focal ischaemia [89], more severely in the white than in the grey matter in acute and early subacute infarcts [90]. ADC threshold values are useful in predicting tissue viability and stroke outcome [91].

Diffusion Tensor Imaging (DTI)

The characterisation of tissue ADC depends both on experimental parameters and tissue microstructure. In tissue such as grey matter, the scalar magnitude of the ADC is independent of the direction in which the diffusion sensitising gradient is applied [31]. Other tissue types such as white matter or skeletal muscle, demonstrate anisotropic water diffusion and therefore a strong dependence on the direction of the applied gradient [7]. In white matter, the angle between the fibre tract axis and the applied field gradient is the critical factor in determining the magnitude of the ADC and the maximum ADC is measured

when the diffusion gradient is applied parallel to this axis.

Diffusion tensor imaging exploits this characteristic of white matter fibres, by measuring the proton diffusion along many different directions [92]. Diffusion weighted acquisitions along a minimum of six directions are required, and the tensor estimate is improved as the number of directions increases. Gradients with directions other than x, y and z are achieved by combinations of these three gradients. The diffusion tensor is a 3×3 matrix with six unique elements. The tensor values are used to determine the diffusion ellipsoid. From the knowledge of the directions applied, and the six or greater number of diffusion weighted images, the diffusion matrix can be calculated[7, 32].

For DTI, the Stejskal-Tanner equation for the dephasing due to diffusion becomes,

$$\frac{S}{S_0} = e^{-b\cdot D_{eff}} \tag{89}$$

where the effective diffusion coefficient, D_{eff}, is a symmetrical matrix,

$$D_{eff} = \begin{vmatrix} D_{xx} & D_{xy} & D_{xz} \\ D_{yx} & D_{yy} & D_{yz} \\ D_{zx} & D_{zy} & D_{zz} \end{vmatrix} \tag{90}$$

and therefore Eq.(89) becomes,

$$\frac{S}{S_0} = \exp(-b_{xx}D_{xx} - b_{yy}D_{yy} - b_{zz}D_{zz} - 2b_{xy}D_{xy} - 2b_{xz}D_{xz} - 2b_{yz}D_{yz}) \tag{91}$$

Both the diagonal and off-diagonal elements of the tensor must be measured in order to determine the principal direction of diffusivity. The values of D_{eff}

can be estimated from the diffusion weighted image data, by multiple linear regression of Eq.(91). On determining the frame of reference $[x', y', z']$ where the off-diagonal elements of D_{eff} are zero (i.e. by diagonalising the matrix), the direction of principal diffusivity can be determined for each voxel [93]. The resulting eigenvectors correspond to the main diffusion directions, and the eigenvalues, λ, correspond to the respective diffusivities. λ_1 , λ_2 and λ_3 correspond to $D_{x'x'}$, $D_{y'y'}$ and $D_{z'z'}$. These diffusivities are used to calculate the resultant diffusion ellipsoid, the principal axis of which indicates the dominant diffusion direction in the voxel, and the most likely direction of the white matter fibres. Two further measures are calculated once the diffusion ellipsoid has been determined for a voxel. The mean diffusivity is an average of the mean of the three ellipsoids [92],

$$\langle D \rangle = \frac{\lambda_1 + \lambda_2 + \lambda_3}{3}$$

The second is fractional anisotropy (FA) which determines the fraction of $|D_{eff}|$ that contributes to anisotropic diffusion. It is a dimensionless value between 0 and 1, where 0 represents perfectly isotropic diffusion.

$$FA = \frac{\sqrt{3[(\lambda_1 - \langle\lambda\rangle)^2 + (\lambda_2 - \langle\lambda\rangle)^2 + (\lambda_2 - \langle\lambda\rangle)^2]}}{\sqrt{2(\lambda_1^2 + \lambda_2^2 + \lambda_3^2)}}$$

Diffusion tensor imaging has been successfully applied to quantitatively evaluate the integrity of highly ordered tissue *in vivo* in both normal and diseased states [94]. One method by which the diffusion measurements obtained in DTI can be summarised is through the calculation of diffusivity and anisotropy. The ADC represents overall diffusivity and can be derived from the trace

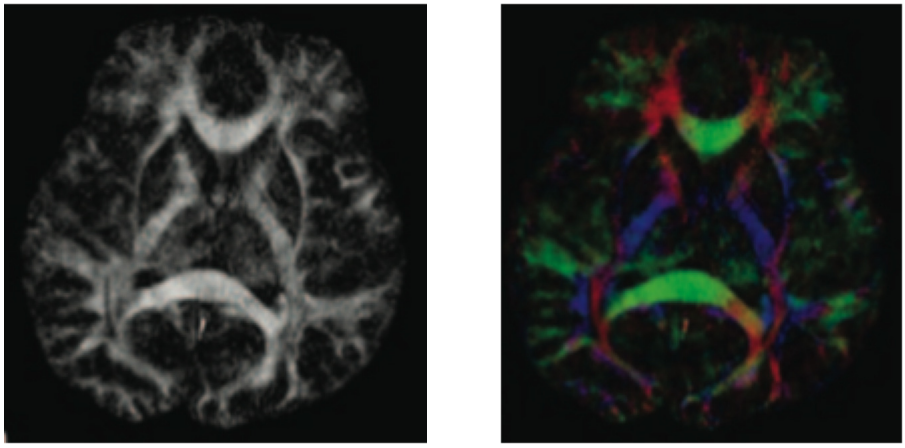

(a) High resolution DTI image (b) FA map

Figure 15: Reproduced from Bammer *et al.* [92]. Fig.15(a) is a high resolution DTI image. Fig.15(b) is a colour-coded fractional anisotropy map. The anterior-posterior direction is represented by red, left-right by green and cephalo-caudal by blue.

of the diffusion tensor. Anisotropy is represented by fractional anisotropy (FA) which is a measure of the degree of diffusion directionality in the tissue microstructure. Water ADC and FA in the white matter of the brain are found to change significantly from childhood to adulthood [95, 96]. Fibre tractography is another application of DTI. It involves the assignment of associations between neighbouring voxels based on eigenvalue and eigenvector information. In simple terms, it is assumed that the eigenvector associated with the largest eigenvalue is aligned with the direction of the white matter fibre bundle [97].

Functional Imaging

Contrast based on blood oxygenation level, volume and flow changes have been used to indirectly detect regional brain activation. Functional MRI (fMRI) provides maps of changes in cerebral blood flow which are interpreted in terms of regions being activated by sensory, motor, or cognitive tasks [98].

The acquired signals contain haemodynamic modulations which means that their spatial and temporal characteristics are biased by complex geometry and varying delivery rates of the vasculature. The resulting temporal delays create spatial dispersions of the detected brain activity using functional MRI [99]

In active regions of the brain an increase in blood flow results in an increase of oxygenated blood in the blood vessels. The magnetisation relaxation properties of the water molecules adjacent to the vasculature is modified and this change can be detected by the MRI scanner. This technique is referred to as blood oxygenation level dependent or BOLD . The local water molecules provide a non-invasive and indirect method to measure the changes in cerebral blood flow following activation.

It has been shown that the diffusion of water slightly slows down in the activated brain cortical areas [6]. This reduction in diffusion, which occurs several seconds before the haemodynamic response detected by BOLD fMRI, has been explained in terms of a phase transition of the water molecules from a somewhat fast to a slower diffusion pool in the cortex undergoing activation.

Ageing

Histological and neuroimaging data of brain tissue have revealed a wide range of age related changes in the brain. Morphological changes include a reduction in total brain volume, cortical thinning and gyral atrophy [100]. Many neuroimaging studies have shown white matter degradation, reduced white-matter integrity and volume loss [101, 102]. The hippocampal formation (associated with declarative memory) displays volume loss in ageing that is significantly accelerated in early stages of Alzheimer's disease [103, 104]. Normal ageing processes, neurodegenerative disorders and demyelinating diseases all exhibit structural

and molecular changes to brain tissue which can be visualised using MRI and in particular DWI techniques [77]. A decrease in the number of myelinated fibres, a reduction in capilliary wall thickness and a reduction in brain metabolism all associated with ageing have been reported [105]. There is a lack of agreement between studies which examined the trends of ADC with ageing. Some investigators found increases in ADC [106], others constant values [107] and further studies exhibited reduced ADCs [108].

Other Clinical Applications

Diffusion weighted MRI is a valuable diagnostic tool and has been shown to be sensitive to a range of pathologies and disease states, in addition to those already discussed above.

Traumatic brain injuries are classified as focal or diffuse. A focal head injury results from a direct impact (e.g. a haematoma). Diffuse injuries arise from shearing and tensile strain on the brain proceeding from rotation or deceleration of adjoining tissues that differ in density or rigidity. DWI can be used to diagnose shearing injuries not visible using other sequences or modalities [88, 109]. Bounding a focal brain lesion such as a contusion or a haematoma there is a region of tissue at risk, characterised by reduced diffusivity.

The diffusion behaviour of water in tumour tissue differs from that of healthy tissue, providing a mechanism for DWI contrast. The technique has been used to identify tumour components and differentiate between normal and tumour tissue in the brain. It has been shown that fractional anisotropy values are reduced in tumours, although they do not provide any further information of tissue differentiation [88]. DTI can be used to determine the effect of the

tumour on local white-matter fibre tracts which is valuable information for surgical planning. Some studies have shown that DWI is sensitive to the effects of therapy on tumours [110, 111]. An increase in ADC due to therapy may be related to tumour necrosis while a subsequent reduction in ADC to original levels within the tumour may be evidence of regrowth.

Lesions associated with multiple sclerosis observed on T_2-weighted images, exhibit mean diffusivity that is increased. The increase has been correlated with the progression of the disease [112, 113]. The highest values of mean diffusivity were found in the lesions with the most destructive pathology. DTI has also been used to investigate white matter abnormalities associated with MS . Increased diffusivity was also found to be present in areas of neuronal loss due to Parkinson's disease [114].

III A Langevin Equation Approach to Normal Diffusion

We have seen that the dephasing and subsequent signal decay observed in DWI is usually analyzed by means of a modification of the classical theory of Brownian motion due to Einstein [18]. This proceeds via the probability density diffusion equation for the phase and was originally formulated by Carr and Purcell [29], who essentially used a form of the central limit theorem of probability theory in order to use Einstein's theory transformed to the phase variable. However, since the diffusion of the phase is directly due to the Brownian motion of the positions of the nuclei, a more transparent approach, which is described here, is based on the Langevin equation for the displacement of the nuclei, which may be explained as follows [1].

A Noninertial Diffusion

In order to illustrate the calculation of the dephasing from the Langevin equation we consider for simplicity the Brownian motion of a free particle along the x-axis. We have seen in Chapter II that the Langevin equation for the random state variables $[X(t), \dot{X}(t)]$ is

$$m\ddot{X}(t) + \zeta\dot{X}(t) = \lambda(t) \tag{92}$$

$\lambda(t)$ is white noise, representing the rapidly fluctuating force on an individual particle, with autocorrelation function $\langle\lambda(t_1)\lambda(t_2)\rangle = 2\zeta kT\delta(t_1 - t_2)$, the angular braces denoting the average over the realisations of the random variable $\lambda(t)$, $2\zeta kT$ is the spectral density, δ is the Dirac delta function. $\zeta\dot{X}(t)$ is the viscous drag, or systematic friction force proportional to the velocity which

represents the average effect of the surroundings on the nucleus. $\lambda(t)$ represents the extremely rapid fluctuations about this average value due to molecular collisions which ensures the perpetual character of the Brownian motion.

In order to illustrate the Langevin equation method for the phase diffusion we shall first derive the Carr-Purcell equation [29] for the phase diffusion following the imposition of a step gradient (Eq. (61)), the original derivation using the Langevin equation has been given in [1]. In terms of the state variables this corresponds to using the non-inertial limit of Eq. (92). The Langevin equation for the random variable $X(t)$ is then simply

$$\dot{X}(t) = \frac{\lambda(t)}{\zeta} \tag{93}$$

with solution given by the stochastic process

$$X(t) = x_0 + \zeta^{-1} \int_0^t \lambda(t')dt' \tag{94}$$

which is commonly called [18] the Wiener process. Thus, dividing by $\triangle t$ we have in the language of infinitesimals,

$$\dot{\Phi}(t) = \gamma \dot{X}(t) \int_0^t G(t')dt' \tag{95}$$

or in the particular case of zero inertia,

$$\dot{\Phi}(t) = \gamma \zeta^{-1} \lambda(t) \int_0^t G(t')dt' \tag{96}$$

which is the noninertial Langevin equation for the phase. In the Brownian motion of a free particle, the phase $\Phi(t)$ (which is simply a linear transformation of the Gaussian random variables $(X(t), \dot{X}(t))$) is a centred Gaussian random variable with variance,

$$\sigma^2 = \langle \triangle \Phi^2 \rangle = \langle \Phi^2 \rangle \tag{97}$$

since $\langle \Phi \rangle = 0$ and $t_0 = 0$. Noting that in general

$$\begin{aligned} 2\int_0^t \Phi(t_1)\dot{\Phi}(t_1)dt_1 &= 2\int_0^t \Phi(t_1)\frac{d\Phi(t_1)}{dt_1}dt_1 \\ &= 2\int_0^t \Phi(t_1)d\Phi(t_1) \\ &= 2\frac{\Phi^2(t)}{2} \\ &= \Phi^2(t) \end{aligned} \tag{98}$$

because we may take $\Phi(0) = 0$, we have in the noninertial case for a step field gradient from Eqs(95) and (96),

$$\Phi^2(t) = 2\int_0^t \left[\frac{\gamma}{\zeta}\int_0^{t_1}\lambda(t_2)\int_0^{t_2} G(t'')dt''dt_2\right]\left[\frac{\gamma\lambda(t_1)}{\zeta}\int_0^{t_1} G(t'')dt''dt_1\right] \tag{99}$$

$$= \frac{2\gamma^2}{\zeta^2}\int_0^t\int_0^{t_1}\lambda(t_2)\int_0^{t_2} G(t'')dt''dt_2\lambda(t_1)\int_0^{t_1} G(t')dt'dt_1$$

$$= \frac{2\gamma^2}{\zeta^2}\int_0^t\int_0^{t_1}\int_0^{t_1} G(t')dt'\int_0^{t_2} G(t'')dt''\lambda(t_1)\lambda(t_2)dt_1dt_2 \tag{100}$$

Recalling the definition of $\lambda(t)$ and the fact that $G(t)$ is not stochastic,

$$\Big\langle \Delta\Phi^2 \Big\rangle = \frac{2\gamma^2}{\zeta^2}\int_0^t\int_0^{t_1}\int_0^{t_1} G(t')dt' \int_0^{t_2} G(t'')dt'' \big\langle \lambda(t_1)\lambda(t_2)\big\rangle dt_1 dt_2 \qquad (101)$$
$$= \frac{2\gamma^2}{\zeta^2} 2kT\zeta \int_0^t\int_0^{t_1}\int_0^{t_1} G(t')dt' \int_0^{t_2} G(t'')dt'' \delta(t_2 - t_1)dt_1 dt_2$$

Now the one-sided delta function has a sifting property such that,

$$\int_0^{t_2} f(t_1)\delta(t_2 - t_1)dt_1 = \frac{f(t_2)}{2}$$

thus for a rectangular field gradient pulse of strength G,

$$\langle \Delta\Phi^2 \rangle = 4\frac{\gamma^2}{\zeta^2} kT\zeta \int_0^t dt_2 \int_0^{t_1} G(t')dt' \int_0^{t_2} G(t'')dt''$$
$$= 2\gamma^2 G^2 \frac{kT}{\zeta} \int_0^t \Big[\int_0^{t_2} dt'' \Big]^2 dt_2$$

Hence,

$$\left\langle \frac{\Delta\Phi^2}{2} \right\rangle = \frac{1}{3}\gamma^2 G^2 D t^3 \qquad (102)$$

Thus we have the Carr-Purcell-Torrey Eq. (61) result for the dephasing [29] following the application of a single step gradient,

$$\big\langle e^{i\Phi} \big\rangle = e^{-\frac{\langle \Delta\Phi^2 \rangle}{2}} = \exp\Big[-\frac{1}{3} D\gamma^2 G^2 t^3 \Big] \qquad (103)$$

The gradient echo result Eq.(65) may be obtained in a similar manner. For

the spin echo case Eq.(70) may be obtained by writing the right hand side of Eq.(101) once again in the notation of Stejskal and Tanner [36]

$$\left\langle \triangle \Phi^2 \right\rangle(t) = 2kT\gamma^2\zeta^{-1} \int_0^{\tau'} [F^2(t_1) + 2(\xi - 1)\mathbf{f} \cdot \mathbf{F} + f^2]dt_1 \tag{104}$$

with $\xi = +1$ for $t < \tau$ and $\xi = -1$ for $t > \tau$, where $\mathbf{F}(t)$ is defined by

$$\mathbf{F}(t) = \int_0^t \mathbf{G}(t')dt'$$

and $\mathbf{f} = \mathbf{F}(\tau)$, where τ is the time of application of the 180^o pulse. Because

$$\int_0^{\tau'} \theta(t' - \tau)F(t')dt' = \int_\tau^{\tau'} F(t')dt'$$

where $\theta(t)$ denotes the initial step function. We have,

$$\begin{aligned}\left\langle \triangle \Phi^2 \right\rangle(t) &= 2\gamma^2 D\Bigg[\int_0^{\tau'} F^2(t')\theta^2(t')dt' - 4\Bigg(\int_0^{\tau'} \theta(t' - \tau)F(t')dt' \Bigg) F(\tau) + \\ &\qquad 4\Bigg(\int_0^{\tau'} \theta^2(t' - \tau)dt' \Bigg) F^2(\tau) \Bigg] \\ &= 2\gamma^2 D\Bigg[\int_0^{\tau'} F^2(t')(t')dt' - 4F(\tau)\Bigg(\int_0^{\tau'} F(t')dt' \Bigg) + 4(\tau' - \tau)F^2(\tau) \Bigg]\end{aligned} \tag{105}$$

B Diffusion equation for the phase

The diffusion equation for the evolution of the pdf $P(x, t|x_0, t_0)$ of the random variable representing the displacement $X(t)$ in Einstein's theory of the Brownian

motion is (Eq (8))

$$\frac{\partial P}{\partial t} = D\frac{\partial^2 P}{\partial x^2}. \tag{106}$$

The lower case letters $x(t)$ etc. denote the realisations of $X(t)$. By means of the usual transformation

$$\Delta\Phi(t) = \int_0^t \omega(t')dt' = \gamma \int_o^t \mathbf{r}(t') \cdot G(t')dt'$$

and the chain rule the corresponding equation for the diffusion of the phase Φ is

$$\frac{\partial f(\phi, t)}{\partial t} = D_\Phi \frac{\partial^2 f(\phi, t)}{\partial \phi^2}, \tag{107}$$

where we suppose that $\triangle\Phi$ and $\triangle t$ approach zero (extremely small displacements in infinitesimally short times) in such a way that [18]

$$D_\Phi = \lim_{\substack{\triangle\Phi\to 0 \\ \triangle t\to 0}} \frac{\left\langle \triangle \Phi^2 \right\rangle}{2 \triangle t} = D\Big(\gamma \int G dt\Big)^2. \tag{108}$$

The diffusion coefficient D_Φ in Eq.(107) is obtained as follows. The change in the phase $\triangle\Phi$ in an elapsed time interval $\triangle t$ is

$$\triangle\Phi = \gamma\Delta X \int_0^{\triangle t} G(t')dt'$$

so that

$$\Phi(t) = \gamma\zeta^{-1}\int_0^t \lambda(t_1)\int_0^{t_1} G(t')dt'dt_1, \tag{109}$$

assuming that $\Phi(0) = 0$. This equation simply expresses the fact that the only way the phase can change is via the equation of motion of $X(t)$. In general, taking account of inertia we would have

$$\Phi(t) = \gamma\int_0^t \dot{X}(t_1)\int_0^{t_1} G(t')dt'dt_1. \tag{110}$$

In order to see how Eq.(109) leads to the correct result for the diffusion coefficient D_Φ namely Eq.(108) we consider (following Wang and Uhlenbeck[15]) the change $\Delta\Phi^2(t)$ in a small time $\triangle t$, then

$$\triangle\Phi = \gamma\int_t^{t+\triangle t}\frac{\lambda(t_1)}{\zeta}dt_1\int_0^{t_1} G(t')dt', \tag{111}$$

so that

$$\begin{aligned}(\triangle\Phi)^2 &= \frac{\gamma^2}{\zeta^2}\int_t^{t+\triangle t}\lambda(t_1)dt_1\int_t^{t+\triangle t}\lambda(t_2)dt_2\Big(\int G(t')dt'\Big)^2 \\ &= \frac{\gamma^2}{\zeta^2}\int\int_{\triangle t}\lambda(t_1)\lambda(t_2)\Big(\int G(t')dt'\Big)^2 dt_2dt_1.\end{aligned} \tag{112}$$

In taking expectation values we have, again remembering that $G(t)$ is not a stochastic variable and using the definition of $\lambda(t)$,

$$\begin{aligned}\left\langle (\triangle\Phi)^2 \right\rangle &= \frac{2\zeta kT\gamma^2}{\zeta^2}\int\int_{\triangle t}\delta(t_1-t_2)dt_1dt_2\Big(\int G(t')dt'\Big)^2 \\ &= \frac{2kT\gamma^2\triangle t}{\zeta}\Big(\int G(t')dt'\Big)^2\end{aligned}$$

or

$$\frac{\left\langle (\triangle\Phi)^2 \right\rangle}{2\triangle t} = \frac{kT}{\zeta}\Big(\int G(t')dt'\Big)^2. \tag{113}$$

Hence the desired result is

$$D_\Phi = D\Big(\int G(t')dt'\Big)^2. \tag{114}$$

Now, in order to solve the diffusion equation, we first calculate the characteristic function

$$\bar{f}(u,t) = \int_{-\infty}^{\infty} e^{iu\phi}f(\phi,t)d\phi = \langle e^{iu\Phi}\rangle. \tag{115}$$

We have

$$\begin{aligned}\frac{\partial\bar{f}(u,t)}{\partial t} &= -u^2D\gamma^2\Big(\int G(t')dt'\Big)^2\bar{f} \\ &= -Dk^2(t)u^2\bar{f}.\end{aligned} \tag{116}$$

For a delta function initial distribution of phases at $t=0$ we then have

$$\bar{f} = \exp\Big(- Du^2 \int_0^t k^2(t')dt' \Big) \tag{117}$$

or

$$\langle e^{iu\Phi} \rangle \equiv \exp \frac{-u^2}{2\sigma^2}.$$

We see from this characteristic function that the phase Φ is a centred Gaussian random variable with variance

$$\sigma^2 = 2D \int_0^t k^2(t')dt' = \langle \triangle \Phi^2 \rangle \tag{118}$$

since we have set $\Phi = 0$ at $t = 0$. Proceeding, we have for a step field gradient

$$\sigma^2 = 2D\gamma^2 G^2 \int_0^t \Big(\int_0^{t'} dt_1 \int_0^{t'} dt_2 \Big) dt' = \frac{2}{3} D\gamma^2 G^2 t^3 \tag{119}$$

which obviously yields the result (see Eq.(103)) obtained from the Langevin equation. The above derivation is simply a special case of a Lemma due to Chandrasekhar [115].

C Phase Diffusion Including the Inertia

The analysis given above ignores the inertia of the Brownian particles. If the inertial effects are included the translational process, $X(t)$, now possesses *two* characteristic times as discussed in Chapter II Section A, one characterizing the

slow diffusion associated with the non-inertial motion which we have already analyzed and the other is the correlation time, $\tau_v = m/\zeta$, of the velocity correlation function. It is of interest to include these in the phase diffusion and therefore we show how the calculation just outlined using the non-inertial Langevin equation, Eq.(93), may be extended for a free particle of mass m as in [1].

For the inertial motion of a Brownian particle an explicit formula for the displacement $X(t)$ is available from the Ornstein-Uhlenbeck theory [18, 116]. This theory is simply the Einstein or Langevin theory with the inertia of the particles included. We start once again by writing again the full Langevin equation in phase space,

$$m\dot{v}(t) = -\zeta v + \lambda(t).$$

It is assumed that the particle starts off at a definite phase point (x_0, v_0) such that the state vector becomes,

$$X(t) = x_0 + \frac{v_0}{\beta}\big(1 - e^{-\beta t}\big) + \frac{1}{m\beta}\int_0^t \big(1 - e^{-\beta(t-t')}\big)\lambda(t')dt' \qquad (120)$$

where $\beta = \zeta/m$. It follows that,

$$v(t) = \dot{X}(t) = v_0 e^{-\beta t} + \frac{1}{m}\int_0^t (1 - e^{-\beta(t-t')})\lambda(t')dt'. \qquad (121)$$

As far as our calculation is concerned the instantaneous displacement Eq.(121) consists of a deterministic term and a random term. x_0 and t_0 may be set to

zero without loss of generality and so therefore on squaring

$$X^2(t) = \frac{v_0^2}{\beta^2}\big(1 - e^{-\beta t}\big)^2 + \frac{1}{(m\beta)^2}\int_0^t \int_0^t \big(1 - e^{-\beta(t-t'')}\big)\big(1 - e^{-\beta(t-t')}\big)\lambda(t')\lambda(t'')dt'dt'' + CC. \tag{122}$$

If we now average this random variable over its realisations and assume a Maxwellian distribution of velocities for the initial velocity v_0, so that it is no longer a point value but has the Gaussian distribution wih $\sigma^2 = \frac{kT}{m}$ we find

$$\begin{aligned}
\langle X^2(t)\rangle &= \frac{kT}{m\beta^2}(1 - e^{-\beta t})^2 + \frac{1}{(m\beta)^2}\int_0^t \int_0^t \big(1 - e^{-\beta(t-t'')}\big)\big(1 - e^{-\beta(t-t')}\big)\langle\lambda(t'')\lambda(t')\rangle dt'dt'' \\
&= \frac{kT}{m\beta^2}(1 - e^{-\beta t})^2 + \frac{2\zeta kT}{(m\beta)^2}\int_0^t \int_0^t \delta(t'' - t')\big(1 - e^{-\beta(t-t'')}\big)\big(1 - e^{-\beta(t-t')}\big)dt'dt'' \\
&= \frac{kT}{m\beta^2}(1 - e^{-\beta t})^2 + \frac{2kT}{(m\beta)}\int_0^t \big(1 - e^{-\beta(t-t')}\big)^2 dt'.
\end{aligned}$$

Examining the second term,

$$\begin{aligned}
\frac{2kT}{(m\beta)}\int_0^t \big(1 - e^{-\beta(t-t')}\big)^2 dt' &= \frac{2kT}{(m\beta)}\int_0^t \big(1 - 2e^{-\beta t}e^{\beta t'} + e^{-2\beta t}e^{2\beta t'}\big)dt' \\
&= 2\frac{kT}{m\beta}\bigg(\big(t - \frac{2}{\beta} + \frac{1}{2\beta}\big) - \big(-\frac{2}{\beta}e^{-\beta t} + \frac{1}{2\beta}e^{-2\beta t}\big)\bigg).
\end{aligned}$$

Reintroducing the first term leads to,

$$\langle X^2(t)\rangle = \frac{kT}{m\beta^2}\big(1 - 2e^{-\beta t} + e^{-2\beta t} + 2\beta t - 3 + 4e^{-\beta t} - e^{-2\beta t}\big).$$

Thus we have the Ornstein-Uhlenbeck [18, 116] result exactly for the mean square displacement of a Brownian particle including the inertia.

$$\left\langle X^2(t)\right\rangle = \frac{2kT}{m\beta^2}\left[\beta t - 1 + e^{-\beta t}\right]. \tag{123}$$

Einstein concluded since the inertial time β^{-1} is of the order of 10^{-7}s for Brownian particles [18] that the inertial effects could be ignored (cf. Eq. 3.1.11 of Ref.[18]). We remark that the characteristic function (corresponding of course to the intermediate scattering function [54]) of $X(t)$ is simply

$$F_x(\kappa, t) = \exp\Big(- \frac{\kappa^2 kT}{\beta^2 m}\left[\beta t - 1 + e^{-\beta t}\right]\Big), \tag{124}$$

where κ denotes the wave number. Clearly this equation is characterised by the times $(\kappa^2 D)^{-1}$ and β^{-1} and its double transcendental nature gives rise to an infinity of exponential decay modes [18] similar to those encountered in the dielectric relaxation of a fixed axis rotator. Moreover, for small inertial effects, Eq.(124) is effectively the sum of two exponential decays, again as in dielectric relaxation. Now

$$\dot{\Phi}(t) = \gamma \dot{X}(t) \int_0^t G(t')dt' \tag{125}$$

and

$$\Phi(t) = \int_0^t \dot{\Phi}(t_1)d(t_1) = \gamma \int_0^t \dot{X}(t_1) \int_0^{t_1} G(t')dt'dt_1. \tag{126}$$

Furthermore we have for sharp initial conditions,

$$\dot{X}(t) = v_0 e^{-\beta t} + \frac{1}{m}\int_0^t e^{-\beta(t-t')}\lambda(t')dt' \tag{127}$$

yielding the velocity correlation function

$$\left\langle \dot{X}(t_1)\dot{X}(t_2)\right\rangle = \frac{kT}{m}e^{-\beta|t_1-t_2|} \tag{128}$$

which of course becomes a delta function in the noninertial limit. Equations (126) to (128) may be used to calculate the mean square value of the phase. We again define a step field gradient where

$$\Phi(t) = \gamma G\int_0^t t_1\dot{X}(t_1)dt_1 \tag{129}$$

and

$$\dot{\Phi}(t) = \gamma G t\dot{X}(t). \tag{130}$$

Hence, noting once again that,

$$\begin{aligned}\Phi^2(t) &= 2\int_0^t \Phi(t_1)\dot{\Phi}(t_1)dt_1 \\ &= 2\int_0^t \left[\gamma G\int_0^{t_1} t_2\dot{X}(t_2)dt_2\right]\left[\gamma G t_1\dot{X}(t_1)\right]dt_1 \\ &= 2\gamma^2G^2\int_0^t\int_0^{t_1} t_1t_2\dot{X}(t_1)\dot{X}(t_2)dt_2dt_1 \\ &= 2\gamma^2G^2\int_0^t\int_0^{t_1} t_1t_2\dot{X}(t_1)\dot{X}(t_2)dt_2dt_1\end{aligned} \tag{131}$$

we have the mean square value of the phase in terms of integrals involving the velocity correlation function and field gradient only

$$\begin{aligned}\langle\Delta\Phi^2\rangle(t) &= 2\gamma^2G^2\int_0^t\int_0^{t_1} t_1t_2\big\langle\dot{X}(t_1)\dot{X}(t_2)\big\rangle dt_1dt_2 \\ &= \frac{2\gamma^2G^2kT}{m}\int_0^t\int_0^{t_1} t_1t_2e^{-\beta(t_1-t_2)}dt_1dt_2 \\ &= \frac{\gamma^2G^2kT}{3\beta^4m}\big[6+t^2\beta^2(2t\beta-3)-6e^{-\beta t}(1+t\beta)\big]\end{aligned} \tag{132}$$

which reduces to the Carr-Purcell-Torrey result, Eq. (61), for long times specified by $t\beta \gg 1$. For short times, such that $t\beta \ll 1$ we have the purely kinematic result

$$\langle\Delta\Phi^2\rangle(t) = \frac{\gamma^2G^2kT}{4m}t^4. \tag{133}$$

Again $\triangle\Phi$ is a linear transformation of a Gaussian random variable so that by the properties of characteristic functions

$$\left\langle e^{i\triangle\Phi}\right\rangle = e^{-\frac{\langle\triangle\Phi^2\rangle}{2}}. \tag{134}$$

Hence Eq (132) yields the inertia corrected dephasing [1] for a step gradient. In general an infinity of fast relaxation modes will be generated due to the double transcendental nature of this function and one dominant much slower mode that is associated with the slow diffusive motion c.f. Eq. (101). An obvious generalisation of the right hand side of Eq.(101) for arbitrary gradient shapes defined by

$$\mathbf{F}(t) = \int_0^t \mathbf{G}(t')dt' \tag{135}$$

is

$$\left\langle \triangle\Phi^2\right\rangle(t) = 2\gamma^2 \int_t\int_{t_1} \left\langle \dot{X}(t_1)\dot{X}(t_2)\right\rangle F(t_1)F(t_2)dt_1dt_2. \tag{136}$$

Hence, in order to calculate the dephasing for a Gaussian process all that is required is a knowledge of the velocity correlation function and the precise form of the field gradients.

We have shown in this chapter how the dephasing magnetisation in magnetic resonance imaging, arising from the Brownian motion of the nuclei, may be determined by simply writing the Langevin equation for the phase random variable and then calculating its characteristic function. The method yields in transparent fashion, from the properties of the characteristic function of Gaussian random variables, the classical dephasing results of Carr-Purcell [29],

Torrey [28], and Stejskal-Tanner [36] for normal diffusion, which are based on the diffusion limit of the discrete time random walk proposed by Einstein [13, 18]. Furthermore it is easily generalised to include the inertia of the nuclei, that is where the underlying statistics are governed by the Ornstein-Uhlenbeck process [116] and to other more complicated situations where the nuclei move in a field of force of potential $V(r)$. Therefore we have a microscopic explanation of the dephasing process in free water; namely it results from the nucleus behaving as a random walker, executing a jump of finite mean square length at uniform time intervals of finite mean duration, so that the *only variable is the orientation of the walker*.

IV Fractional Diffusion: Possible Explanations of the Stretched Exponential Behaviour using the Fractional Langevin equation

As far as one possible explanation of the stretched exponential model proposed by Bennett *et al.* [40] (Eq.(82)) based on the microscopic origins of anomalous diffusion is concerned, we note that the finite jump-length variance and finite average jump-time, in the theory of the normal Brownian motion, define a physical length scale and a physical timescale [21]. Here the ordinary central limit theorem applies. We have mentioned that in anomalous diffusion, however, either the second moment of the jump-length distribution or the first moment of the jump time distribution diverges, or both of them. We have seen that such motions are characterised by heavy tailed probability distributions (i.e., power law tails), so that the central limit theorem no longer applies [23, 117]. They are known by the generic title of continuous time random walks (CTRW) [24, 22, 118]. Examples are the Lévy stable motion for which the mean square displacement diverges due to the occurrence of very long jumps [118]. Such a nonlocal walk in space leads to enhanced diffusion and ultimately turbulence, as the overall displacement is dominated by the largest jumps without any time cost, that is, jumps of arbitrary length all take the same time if the jump length is a Lévy process. On the other hand, processes that are nonlocal in time consequently exhibit memory effects, i.e., the so-called long rests or fractal-time random walk model (fractus *latin* - broken). Here, in contrast to the continuum limit of the discrete time random walk considered by Einstein, in which the time intervals between jumps are uniform, the walker may remain in a given configuration for an arbitrarily long period before undertaking a jump. The fractal time random walk invariably leads to subdiffusion as the

random walker always risks being trapped in some site for an arbitrarily long time before advancing a distance equal to the finite jump length variance. As usual α is the fractal dimension of the set of waiting times [18, 21], which is the scaling of the waiting time segments in the random walk with magnification.

It is clear that both jump times and jump lengths may exhibit *chaotic* behaviour. Thus, it is impossible to attribute underlying physical scales to such processes. For example, the origin of the chaotic set of jump times may be due to a random distribution of impurities within a matrix. Such a distribution will give rise to an extremely broad range of microscopic transition rates. Hence, a *spatial* disorder corresponding to a chaotic energy landscape (energetic disorder) will give rise to a *temporal* disorder because of the very large ranges of chaotic barrier heights involved, resulting in anomalous diffusion [18, 21]. Another microscopic explanation (the one which will be used in this chapter as it lends itself to analysis using the Langevin equation) is that the anomalous behaviour simply arises from the inclusion of memory effects [18] in the normal Brownian motion, so destroying its Markovian character as highlighted by Mandelbrot and van Ness [3] (see [4] for a recent review).

The use of anomalous diffusion to describe relaxation behaviour is very well established in many fields of physics, including biophysics and physics in medicine [73]. In the particular case of sub-diffusive transport, for example, we mention [73, 117, 119, 120] such diverse phenomena as charge carrier transport in amorphous semiconductors, diffusion in percolative or porous systems, transport in fractal geometries as well as protein conformational dynamics. We have also mentioned that in the NMR context the anomalous diffusion approach was used in phenomenological fashion by Magin *et al.*[38], where the Bloch-Torrey equation was converted to fractional form.

However in using random walk models in the context of microscopic

explanations, it should be noted that if diffusion in tissue is *restricted* or hindered, i.e. it does not take place in an infinite reservoir, then it may lead to very different signal attenuations [30]. For example, Robertson [121] described motional narrowing long-time regime for diffusion between parallel planes when the signal decays exponentially in time, unlike t^3 as it is for unrestricted diffusion. Stejskal and Tanner [122] showed that the signal has oscillatory behaviour for narrow gradient pulses and the related diffusion-diffraction patterns were observed by Callaghan *et al.* [123]. The localisation regime predicted by Stoller *et al.* [124] exhibits a stretched-exponential behaviour. In these and many other cases [30, 125], diffusion may be considered as normal, and it is a geometrical restriction alone which may lead to deviations from the classical unrestricted diffusion.

Virtually all the microscopic approaches above, ultimately rely on the probability density function of the phase, a notable exception being that of Chen and Widom [126] who used a frequency domain analysis based on the spectral function, characterizing fractal Brownian motion. However, since the random variable underlying the process is the position of a nucleus, we have seen that a much more transparent treatment of the phase diffusion could be achieved by means of the Langevin equation. We have also seen that for normal diffusion, this is simply the Newtonian equation of motion of the nucleus, augmented by a systematic frictional force proportional to the velocity, superimposed on which is a very rapidly fluctuating random force, both representing the effect of the surrounding heat-bath on the nucleus.

A Fractional Diffusion

Here the objective is to provide a microscopic basis for the empirical stretched exponential Eq.(82) of Bennett *et al* [40]. Our particular hypothesis is [1]

that it may be explained via memory effects giving rise to fractional Brownian motion (which preserves a few of the features of the continuous time random walk). In order to achieve this via the Langevin equation, we note that Lutz [2] following the analysis of fractional Brownian motion given by Mandelbrot and van Ness has introduced a fractional Langevin equation for the translational motion of a free Brownian particle viz.:

$$m\frac{d}{dt}v(t) + m\beta_{\alpha 0}D_t^{\alpha-1}v(t) = \lambda(t) \tag{137}$$

where (as in the normal Langevin equation) $v(t) = \dot{X}(t)$ is the velocity of the particle, β_α is the friction coefficient, $m\beta_{\alpha 0}D_t^{\alpha-1}v(t)$ and $\lambda(t)$ are respectively the generalised frictional and random forces with the properties

$$\big\langle \lambda(t) \big\rangle = 0, \quad \big\langle \lambda(t')\lambda(t) \big\rangle = \frac{mkT\beta_\alpha}{\Gamma(1-\alpha)}|t-t'|^{-\alpha}$$

(Γ denotes the gamma function). The Riemann-Liouville fractional derivative [58] is defined by

$${}_0D_t^{-\sigma}g(t) = \frac{1}{\Gamma(\sigma)}\int_0^t \frac{g(t')}{(t-t')^{1-\sigma}}dt', \quad 0 < \sigma < 1 \tag{138}$$

has the form of a memory function so that Eq.(137) may be regarded as a generalised Langevin equation [2, 18] describing subdiffusion.

The memory function $K\alpha(t)$ is given (in accordance with the fluctuation dissipation theorem [19, 54]) by the autocorrelation function

$$K_\alpha(t) = \frac{1}{kT}\big\langle \lambda(0)\lambda(t) \big\rangle \tag{139}$$

and thus the fractional Langevin equation Eq.(137) can be written in the form

[1],

$$m\frac{dv(t)}{dt} + \int_0^t K_\alpha(t-t')v(t')dt' = \lambda(t). \tag{140}$$

If α equals unity, then Eq.(140) becomes the normal Langevin equation, in which case the noise function becomes white, and its correlation function is a delta function.

B Solution of the Generalised Langevin Equation

Lutz [2] also supposed that the random force $\lambda(t)$ is Gaussian. Thus the fractional Brownian motion, typified by Eq.(137) which is simply a linear transformation of a Gaussian random variable, describes Gaussian transport. However, it is still capable of reproducing the stretched exponential behaviour associated with anomalous diffusion and has the merit unlike CTRW treatments that Eq.(56) still applies, i.e. a knowledge of the first two moments is sufficient to calculate all the higher order moments and so the characteristic function. Nevertheless, the process described by the Langevin equation has a mean square displacement which is the same as that ensuing from the CTRW and reproduces some of its features, however failing to reproduce many others such as weak ergodicity breaking [22]. It should be noted that the fractional Langevin equation (137) may also be used to study both subdiffusion and superdiffusion of a particle coupled to a fractal heat bath [2].

The *formal* exact solution of Eq.(137) may be obtained using Laplace transforms [18]. We have (c.f. Eq. (11.76) of [18])

$$\begin{aligned} v(t) &= \dot{X}(t) \\ &= \dot{X}(0)E_{2-\alpha,1}\big(-\beta_\alpha t^{2-\alpha}\big) + \frac{1}{m}\int_0^t E_{2-\alpha,1}\big(-\beta_\alpha (t-t')^{2-\alpha}\big)\lambda(t')dt' \end{aligned} \tag{141}$$

and

$$X(t) = X(0) + \int_0^t \dot{X}(t')dt'$$
$$= X(0) + \dot{X}(0)tE_{2-\alpha,2}\big(-\beta_\alpha t^{2-\alpha}\big) + \frac{1}{m}\int_0^t \int_0^{t''} E_{2-\alpha,1}\big(-\beta_\alpha (t-t')^{2-\alpha}\big)\lambda(t')dt'dt'' \tag{142}$$

where $E_{\alpha,\beta}(z)$ is the generalised Mittag-Leffler function defined by [2, 18]

$$E_{\alpha,\beta}(z) = \sum_{k=0}^{\infty} \frac{z^k}{\Gamma(\beta + k\alpha)},\ (\alpha, \beta > 0)$$

Here the Mittag-Leffler function $E_\alpha(z)$ is $E_{\alpha,1}(z)$, furthermore

$$\int_0^t E_{2-\alpha,1}\big(-\beta_\alpha t'^{2-\alpha}\big)dt' = tE_{2-\alpha,2}\big(-\beta_\alpha t^{2-\alpha}\big)$$

Thus we have from Eq.(141) the angular velocity correlation function for fractional Brownian motion,

$$\big\langle \dot{X}(0)\dot{X}(t)\big\rangle = \left(\frac{kT}{m}\right) E_{2-\alpha}\big(-\beta_\alpha t^{2-\alpha}\big) \tag{143}$$

where E_α interpolates between the initial stretched exponential form

$$E_{2-\alpha}\big(-\beta_\alpha t^{2-\alpha}\big) \sim \exp\left(\frac{-\beta_\alpha t^{2-\alpha}}{\Gamma(3-\alpha)}\right) \tag{144}$$

and the long time inverse power law behaviour

$$\frac{1}{\beta_\alpha t^{2-\alpha}\Gamma(\alpha-1)}. \tag{145}$$

Thus in contrast to the purely exponential decay predicted by Eq.(128) the angular velocity correlation function has initial stretched exponential behaviour,

accompanied by a slowly decaying long time tail representing a memory of the initial conditions. Noting that $X^2(t)$ is given by

$$X^2(t) = X^2(0) + 2\int_0^t X(t')\dot{X}(t')dt',$$

we have (for $X(0) = 0$),

$$\begin{aligned}\left\langle X^2(t)\right\rangle &= \frac{2kT}{m}\int_0^t\int_0^{t'} E_{2-\alpha}\big(-\beta_\alpha(t'-t'')^{2-\alpha}\big)dt''dt' \\ &= \frac{2kT}{m}t^2 E_{2-\alpha,3}\big(-\beta_\alpha t^{2-\alpha}\big) \\ &\simeq \frac{2kT}{m\beta}\frac{t^\alpha}{\Gamma(1+\alpha)}\end{aligned} \tag{146}$$

in the long time limit $\beta t \gg 1$, because for large z the generalised Mittag-Leffler function $E_{a,b}(z)$ has the inverse power law behaviour (long time tail) [2, 126]

$$E_{a,b}(z) \sim \frac{1}{z\Gamma(b-a)}.$$

According to the definition, the range $0 < \alpha < 1$, corresponds to subdiffusion in configuration space signifying a slow relaxation process. Eq.(143) for the velocity correlation function for fractional Brownian motion is identical to the velocity correlation function rendered by the diffusion limit of the CTRW with a power law distribution of waiting times [18]. Lutz [2] has also shown that these completely different forms of non-Markovian anomalous diffusion share some common characteristics. In particular, they satisfy the same generalized Einstein relation and their lowest moments are all equal with the exception of the second moment of the velocity [2, 18].

C Extension to Fractional Diffusion for the Gradient Echo Case

Proceeding for a step field gradient and noting Eq.(131), we have the mean square phase,

$$\begin{aligned}\langle \Delta\Phi^2(t)\rangle &= 2\gamma^2 G^2 \int_0^t \int_0^{t_1} t_1 t_2 \big\langle \dot{X}(t_1)\dot{X}(t_2)\big\rangle dt_1 dt_2 \\ &= 2\gamma^2 G^2 \frac{kT}{m} \int_0^t \int_0^{t_1} t_1 t_2 E_{2-\alpha}\big[-\beta_\alpha (t_1-t_2)^{2-\alpha}\big] dt_1 dt_2\end{aligned} \tag{147}$$

In the noninertial limit, i.e., at long times, $t\beta \gg 1$, again noting the asymptotic behaviour of the Mittag-Leffler function

$$E_{2-\alpha}\big(-\beta_\alpha t^{2-\alpha}\big) \sim \frac{1}{\beta_\alpha} t^{2-\alpha}\Gamma(\alpha-1), \tag{148}$$

we have

$$\begin{aligned}\langle \Delta\Phi^2(t)\rangle &= 2\gamma^2 G^2 \frac{kT}{m} \int_0^t \int_0^{t_1} t_1 t_2 \frac{1}{\beta_\alpha (t_1-t_2)^{2-\alpha}\Gamma(\alpha-1)} dt_1 dt_2 \\ &= 2\gamma^2 G^2 \frac{kT}{m\beta_\alpha} \frac{1}{\Gamma(\alpha-1)} \int_0^t \int_0^{t_1} \frac{t_1 t_2}{(t_1-t_2)^{2-\alpha}} dt_1 dt_2.\end{aligned} \tag{149}$$

The value of the first integral is,

$$\int_0^{t_1} \frac{t_2}{(t_1-t_2)^{2-\alpha}} dt_2 = \frac{t_1^\alpha}{\alpha(\alpha-1)},$$

while,

$$\int_0^t \frac{t_1^\alpha}{\alpha(\alpha-1)} t_1 dt_1 = \frac{1}{\alpha(\alpha-1)} \frac{t^{\alpha+2}}{(\alpha+2)}.$$

By substituting this result back into Eq.(149) we obtain,

$$\langle \Delta\Phi^2(t) \rangle = 2\gamma^2 G^2 \frac{kT}{m\beta_\alpha} \frac{1}{\Gamma(\alpha-1)} \frac{1}{\alpha(\alpha-1)} \frac{t^{\alpha+2}}{(\alpha+2)} \tag{150}$$

Now using the property of the gamma function, that $\Gamma(z+1) = z\Gamma(z)$, Eq.(150) may be simplified to,

$$\langle \Delta\Phi^2(t) \rangle = \gamma^2 G^2 \frac{kT}{m\beta_\alpha} \frac{2(\alpha+1)}{\Gamma(\alpha+3)} t^{\alpha+2} \tag{151}$$

$$\langle e^{i\triangle\Phi} \rangle = e^{-\frac{\langle \triangle\Phi^2 \rangle}{2}} = \exp\left(-\gamma^2 G^2 \frac{kT}{m\beta_\alpha} \frac{(\alpha+1)}{\Gamma(\alpha+3)} t^{\alpha+2} \right). \tag{152}$$

For the *bipolar* gradient echo experiment (consisting of two step functions, with opposite polarity), the normalised signal decay becomes,

$$ln\left[\frac{S(t)}{S_0}\right] = \exp -\left(2\gamma^2 G^2 \frac{kT}{m\beta_\alpha} \frac{(\alpha+1)}{\Gamma(\alpha+3)} t^{\alpha+2} \right) \tag{153}$$

which can be rewritten as,

$$ln\left[\frac{S(t)}{S_0}\right] = \exp -\left(2\gamma^2 G^2 D \frac{t^{\alpha+2}}{(2+\alpha)\Gamma(1+\alpha)} \right). \tag{154}$$

In the normal diffusion limit, $\alpha \to 1$, Eq.(154) reduces to Eq.(66), viz.,

$$ln\left[\frac{S(t)}{S_0}\right] = -\frac{2}{3}\gamma^2 G^2 t^3. \tag{155}$$

For short times ($t\beta \ll 1$), we have

$$\langle \Delta\Phi^2(t) \rangle \approx \frac{\gamma^2 G^2 kT}{4m} t^4 \Big[1 - \frac{8\beta_\alpha t^{2-\alpha}}{(6-\alpha)\Gamma(5-\alpha)} + ... \Big]. \tag{156}$$

The leading term of the expansion (156) coincides with the purely kinematic

result Eq.(132). Again $\triangle\Phi$ is a linear transformation of a Gaussian random variable so that the characteristic function Eq.(134) yields the dephasing.

The fractional Brownian motion we have just discussed assumes that the driving force $\lambda(t)$ is Gaussian so that the characteristic function Eq.(134) still applies as in the normal Brownian motion. Hence the decay of the phase remains (albeit stretched) exponential. Thus the phase as calculated from the fractional Brownian motion, unlike fractal time relaxation (more precisely the diffusion limit of the continuous time random walk, where unlike the discrete random walk considered by Einstein [18] no mean waiting time between jumps of the walker exists) does not exhibit the characteristic long time tail often associated with anomalous diffusion processes signifying that the diffusion process depends strongly on the initial conditions. If this phenomena is included, it appears no longer possible to treat the dephasing process using the Langevin equation and a fractional diffusion equation similar to that treated in Refs[2, 23] adapted to the phase must be used rendering the solution much more complicated.

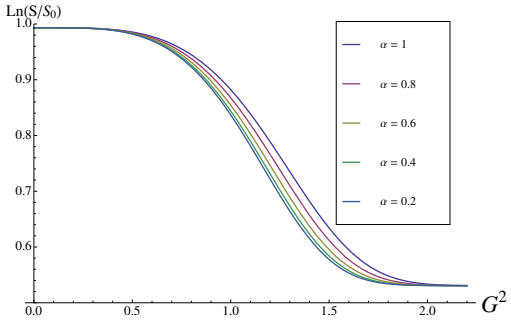

(a) Varying Gradient Strength, G

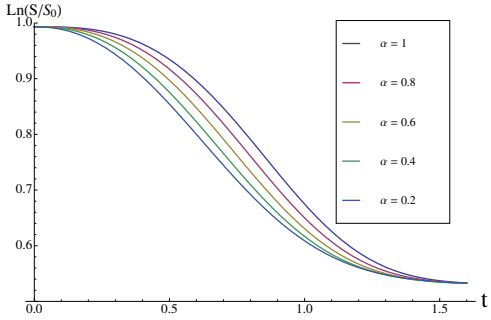

(b) Varying Gradient Duration, δ

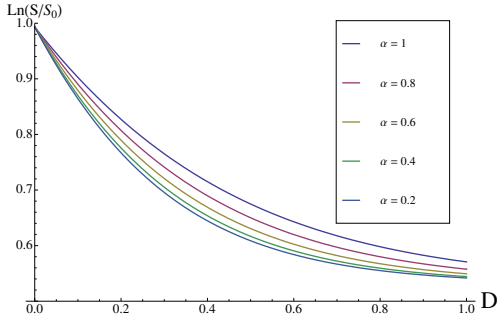

(c) Varying the Diffusion Coefficient

Figure 16: Plots of varying parameters in the anomalous diffusion equation for the spin echo experiment. The effects of varying the gradient strength, G, the gradient duration, δ and the diffusion coefficient, D are shown.

D The Spin Echo Calculation

The most significant difference between the spin echo and simple bipolar pulse sequences is the timing gap between the first and second rectangular gradients. We follow the Stejskal and Tanner method [36]once again and employ,

$$\frac{dS}{dt} = -\gamma^2 D\big[F(t)\theta(t) - 2\theta(t-\tau)F(\tau)\big]^2 S \tag{157}$$

where $\mathbf{F}(t) = \int_0^t \mathbf{G}(t')dt'$ and $\theta(t)$ is the unit step function. The 180^o refocussing pulse is placed midway between the two gradient pulses, at $t = \tau$. Each of the gradient functions has duration τ and the second pulse begins at $t = \Delta$. The solution of Eq.(157) is

$$S(t) = S(0)\exp\Big[-\int_0^t g(t')dt'\Big], \tag{158}$$

where

$$\int_0^{\tau'} g(t')dt' = -\gamma^2 D\Bigg[\int_0^{\tau'} F^2(t')dt' - 4F(\tau)\int_0^{\tau'} F(t')dt' + 4(\tau'-\tau)F^2(\tau)\Big]. \tag{159}$$

The fractional evaluation becomes more complicated, as we must integrate over two arbitrary time intervals t_1 and t_2, and therefore must define the two gradient integrals, $F(t_1)$ and $F(t_2)$.

$$\begin{aligned} F(t_1) &\rightarrow F(t_1)\theta(t_1) - 2\theta(t_1-\tau)F(\tau) \\ F(t_2) &\rightarrow F(t_2)\theta(t_2) - 2\theta(t_2-\tau)F(\tau). \end{aligned} \tag{160}$$

Recalling Eq.(147), we have

$$\langle \Delta\Phi^2(t) \rangle = 2\gamma^2 \frac{kT}{m\beta_\alpha} \frac{1}{\Gamma(\alpha-1)} \int_0^t dt_2 \int_0^{t_1} \frac{1}{(t_1-t_2)^{2-\alpha}} F(t_1)F(t_2)dt_1 \quad (161)$$

Here the product of $F(t_1)$ and $F(t_2)$ can be presented as

$$\begin{aligned} F(t_1)F(t_2) =& \big[F(t_1)\theta(t_1) - 2\theta(t_1-\tau)F(\tau)\big]\big[F(t_2)\theta(t_2) - 2\theta(t_2-\tau)F(\tau)\big] \\ =& F(t_1)F(t_2)\theta(t_1)\theta(t_2) - 2F(\tau)F(t_2)\theta(t_2)\theta(t_1-\tau) \\ & - 2F(t_1)F(\tau)\theta(t_1)\theta(t_2-\tau) + 4F^2(\tau)\theta(t_1-\tau)\theta(t_2-\tau). \end{aligned} \quad (162)$$

The evaluation of integrals in Eq.(161) can then be performed in piecewise fashion provided we can write $F(t)$ explicitly in four intervals of integration, viz.,

$$(0,\delta), (\delta,\Delta), (\Delta,\Delta+\delta), (\Delta+\delta,2\tau).$$

The contribution of each term of Eq.(162) in Eq.(161) must be evaluated separately for all intervals of integration. We take, as an example, the first term only, viz., $F(t_1)F(t_2)\theta(t_1)\theta(t_2)$; other terms can be evaluated in a similar manner. The first interval of integration $(0,\delta)$ in Eq.(161) falls over the first rectangular gradient pulse and, hence,

$$F(t_1)F(t_2)\theta(t_1)\theta(t_2) = G^2 t_1 t_2 \theta(t_1)\theta(t_2). \quad (163)$$

Inserting Eq.(162) into Eq.(163) and performing the integrations yields

$$\left\langle \triangle \Phi^2 \right\rangle(t)\Big|_{1(1)} = \frac{2kT\gamma^2}{m\beta_\alpha \Gamma(\alpha-1)} \int_0^\delta dt_2 \int_0^{t_2} \frac{G^2 t_1 t_2 dt_1}{(t_2-t_1)^{2-\alpha}}$$
$$= \frac{2kT\gamma^2}{m\beta^\alpha} \frac{(G^2\delta^{2+\alpha})}{(2+\alpha)\Gamma(1+\alpha)}. \tag{164}$$

During the second time interval from δ to Δ, $G = 0$ and thus $F(t_1)$ and $F(t_2)$ remain constant, so that $F(t_1)F(t_2)\theta(t_1)\theta(t_2) = G^2\delta^2\theta(t_1)\theta(t_2)$ and

$$\left\langle \triangle \Phi^2 \right\rangle(t)\Big|_{1(2)} = \frac{2kT\gamma^2}{m\beta_\alpha \Gamma(\alpha-1)} \int_\delta^\Delta dt_2 \int_\delta^{t_2} \frac{G^2\delta^2 dt_1}{(t_2-t_1)^{2-\alpha}}$$
$$= \frac{2kT\gamma^2}{m\beta^\alpha} G^2\delta^2 \frac{(\Delta-\delta)^\alpha}{\Gamma(1+\alpha)}. \tag{165}$$

The third time interval includes the second gradient pulse, from Δ to $\Delta+\delta$. Here

$$F(t_1)F(t_2)\theta(t_1)\theta(t_2) = (Gt_1 - G\Delta + G\delta)(Gt_2 - G\Delta + G\delta)\theta(t_1)\theta(t_2)$$

and

$$\left\langle \triangle \Phi^2 \right\rangle(t)\Big|_{1(3)} = \frac{2kT\gamma^2 G^2}{m\beta_\alpha} \int_\Delta^{\Delta+\delta} (t_2 - \Delta + \delta) dt_2 \int_\Delta^{t_2} \frac{(t_1 - \Delta + \delta) dt_1}{\Gamma(\alpha-1)(t_2-t_1)^{2-\alpha}}$$
$$= \frac{2kT\gamma^2 G^2}{m\beta^\alpha} \frac{(5+2\alpha)\delta^{2+\alpha}}{(2+\alpha)\Gamma(1+\alpha)}. \tag{166}$$

Finally, in the interval from the end of the second gradient at $t = \Delta+\delta$ to 2τ, $G = 0$ and $F(t_1)$ and $F(t_2)$ are constant, so that $F(t_1)F(t_2)\theta(t_1)\theta(t_2) =$

$4G^2\delta^2\theta(t_1)\theta(t_2)$ and

$$\left\langle \triangle \Phi^2 \right\rangle(t)\Big|_{1(4)} = \frac{2kT\gamma^2}{m\beta_\alpha \Gamma(\alpha-1)} \int_{\Delta+\delta}^{2\tau} dt_2 \int_{\Delta+\delta}^{t_2} \frac{(2G\delta)^2 dt_1}{(t_2-t_1)^{2-\alpha}}$$
$$= \frac{8kT\gamma^2}{m\beta_\alpha} \frac{G^2\delta^2(2\tau-\delta-\Delta)^{2-\alpha}}{\Gamma(1+\alpha)}. \tag{167}$$

The sum of Eqs.(164),(165),(166), and (167) yields the contribution of the first term.

$$\left\langle \triangle \Phi^2 \right\rangle(t)\Big|_1 = \frac{2kT\gamma^2}{m\beta_\alpha} \frac{G^2\delta^2}{\Gamma(1+\alpha)} \left\{ \frac{2(3+\alpha)\delta^\alpha}{(2+\alpha)} + (\Delta-\delta)^\alpha + 4(2\tau-\delta-\Delta)^\alpha \right\}. \tag{168}$$

Each of the other three terms in Eq.(162) must be treated in a similar manner, but only from τ to 2τ, as these terms are zero for $t < \tau$. The results are, respectively,

$$\left\langle \triangle \Phi^2 \right\rangle(t)\Big|_2 = \left\langle \triangle \Phi^2 \right\rangle(t)\Big|_3$$
$$= -\frac{4kT\gamma^2}{m\beta_\alpha} \frac{G^2\delta^2}{\Gamma(1+\alpha)} \left\{ \frac{(1+2\alpha)\delta^\alpha}{(1+\alpha)} + (\Delta-\tau)^\alpha + 2(2\tau-\delta-\Delta)^\alpha \right\}. \tag{169}$$

$$\left\langle \triangle \Phi^2 \right\rangle(t)\Big|_4 = \frac{8DG^2\delta^2\gamma^2}{\Gamma(1+\alpha)} \left\{ \delta^\alpha + (\Delta-\tau)^\alpha + (2\tau-\delta-\Delta)^\alpha \right\}. \tag{170}$$

When all these terms have been evaluated and summed, the resulting equation for the fractional diffusion spin echo experiment is given by,

$$\left\langle \triangle \Phi^2 \right\rangle = 2\gamma^2 D \frac{G^2\delta^2}{\Gamma(1+\alpha)} \left[\frac{2\delta^\alpha}{2+\alpha} + (\Delta-\delta)^\alpha \right]. \tag{171}$$

In the normal diffusion limit ($\alpha = 1$) this reduces to the Stejskal-Tanner Eq.(76).

E The Ramp and Triangular Gradient Shapes

The technique can easily be applied to any other gradient configuration. The two gradient shapes mentioned in Chapter II were a ramped and triangular gradient design.

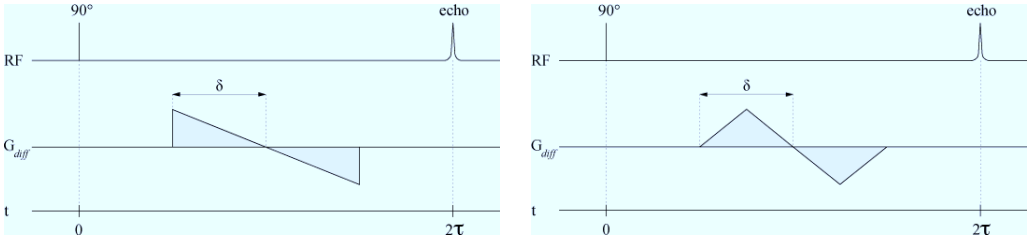

(a) Ramped Gradient Shape (b) Triangular Gradient Shape

Figure 17: Timing diagrams for the alternative gradient shape designs

We have in general c.f. Eq.(161),

$$\langle \Delta\Phi^2(t) \rangle = 2\gamma^2 \frac{kT}{m\beta_\alpha} \frac{1}{\Gamma(\alpha-1)} \int_0^t dt_2 \int_0^{t_1} \frac{1}{(t_1-t_2)^{2-\alpha}} F(t_1)F(t_2)dt_1.$$

For the ramped gradient shape (c.f. Eq. (71)),

$$F(t_1) = \int_0^{t_1} \Big(-G\frac{t-\delta}{\delta} \Big) dt \tag{172}$$

so that

$$F(t_1)F(t_2)\theta(t_1)\theta(t_2) = \Big(Gt_1 - \frac{Gt_1^2}{2\delta} \Big) \Big(Gt_2 - \frac{Gt_2^2}{2\delta} \Big). \tag{173}$$

Thus,

$$\Big\langle \Delta\Phi^2 \Big\rangle (t) = \frac{2kT\gamma^2}{m\beta_\alpha} \int_0^{2\delta} \Big(Gt_2 - \frac{Gt_2^2}{2\delta} \Big) dt_2 \int_0^{t_2} \frac{dt_1}{\Gamma(\alpha-1)} \frac{1}{(t_2-t_1)^{2-\alpha}} \Big(Gt_1 - \frac{Gt_1^2}{2\delta} \Big) \tag{174}$$

that is

$$\left\langle \frac{\Delta\Phi^2}{2} \right\rangle(t) = D\gamma^2 G^2 \frac{(2\delta)^{2+\alpha}\alpha(\alpha+3)}{\Gamma(5+\alpha)}. \tag{175}$$

When $\alpha \to 1$, the expression becomes the normal diffusion case Eq. (71)

Now for the triangular configuration,

$$\left\langle \Delta\Phi^2 \right\rangle_{0\to\frac{\delta}{2}} = \frac{2kT\gamma^2}{m\beta_\alpha} \int_0^{\frac{\delta}{2}} \left(\frac{Gt_2^2}{\delta} \right) dt_2 \int_0^{t_2} \frac{dt_1}{\Gamma(\alpha-1)} \frac{1}{(t_2-t_1)^{2-\alpha}} \left(\frac{Gt_1^2}{\delta} \right) \tag{176}$$

$$\left\langle \Delta\Phi^2 \right\rangle_{\frac{\delta}{2}\to\delta} = \frac{2kT\gamma^2}{m\beta_\alpha} \int_{\frac{\delta}{2}}^{\delta} \left(\frac{Gt_2}{2}\left(4 - \frac{2t_2}{\delta}\right) + \frac{G\delta}{2} \right) dt_2 \times \int_{\frac{\delta}{2}}^{t_2} \frac{dt_1}{\Gamma(\alpha-1)} \frac{1}{(t_2-t_1)^{2-\alpha}} \left(\frac{Gt_1}{2}\left(4 - \frac{2t_1}{\delta}\right) + \frac{G\delta}{2} \right) \tag{177}$$

$$\left\langle \Delta\Phi^2 \right\rangle_{\delta\to\frac{3\delta}{2}} = \frac{2kT\gamma^2}{m\beta_\alpha} \int_{\delta}^{\frac{3\delta}{2}} \left(\frac{Gt_1}{2}\left(6 - \frac{t_1}{\delta}\right) - 4G\delta + \frac{G\delta}{2} \right) dt_2 \times \int_{\delta}^{t_2} \frac{dt_1}{\Gamma(\alpha-1)} \frac{1}{(t_2-t_1)^{2-\alpha}} \left(\frac{Gt_1}{2}\left(6 - \frac{t_1}{\delta}\right) - 4G\delta + \frac{G\delta}{2} \right) \tag{178}$$

$$\left\langle \Delta\Phi^2 \right\rangle_{\frac{3\delta}{2}\to 2\delta} = \frac{2kT\gamma^2}{m\beta_\alpha} \int_{\frac{3\delta}{2}}^{2\delta} \left(\frac{G}{2\delta}\left(15\delta^2 - 8\delta t_1 + t_1^2\right) + \frac{G\delta}{2} \right) dt_2 \times \int_{2\delta}^{t_2} \frac{dt_1}{\Gamma(\alpha-1)} \frac{1}{(t_2-t_1)^{2-\alpha}} \left(\frac{G}{2\delta}\left(15\delta^2 - 8\delta t_1 + t_1^2\right) + \frac{G\delta}{2} \right). \tag{179}$$

Thus,

$$\left\langle \frac{\Delta\Phi^2}{2} \right\rangle(t) = \frac{2D\gamma^2 G^2 \delta^{2+\alpha}}{8\Gamma(5+\alpha)}(3+\alpha)(12+\alpha(24+9\alpha+\alpha^2)) \tag{180}$$

which yields Eq.(73) in the normal diffusion limit $\alpha \to 1$.

F Conclusion

We have shown that the method outlined in Chapter III viz. [1], the application of the Langevin equation to the dephasing of the magnetisation due to diffusion, may also be extended to anomalous diffusion in a transparent fashion, in order to provide a possible microscopic justification for the use of stretched exponentials to describe the dephasing in tissue. Specifically we suggest that the anomalous diffusion may ultimately have its origin in memory effects giving rise to fractional Brownian motion. This process naturally introduces the new fitting parameter, α, related to the Hurst index [3], indicating the role played by fractional dynamics in the time for the complex diffusion which is observed in human neuronal tissue. In normal diffusion, $\alpha = 1$, so that we regain the classical expressions of Carr and Purcell etc. once more.

V Magnetic Resonance Imaging Methods

It is a well established fact that water in neuronal tissue does not diffuse freely. In magnetic resonance imaging, the application of diffusion weighting gradients in an imaging sequence, causes a loss in signal intensity. As the degree of diffusion weighting is increased during a series of image acquisitions, the signal intensity decreases with a monoexponential decay for freely diffusing water, while the decay in neuronal tissue can be described empirically with a biexponential model. This deviation from free diffusion arises from the complexity of the cellular environment, with factors including molecular crowding and transient binding events thought to play important roles.

Diffusion MRI is a non-invasive technique, and as such we cannot expect to determine a 'correct' diffusion coefficient in *in vivo* experiments, hence we cannot hope to determine which mathematical model is the most suitable. As we have seen, many empirical expressions have been proposed which fit the diffusion weighted MRI data. The principal aim to create a more sensitive tool for the detection of abnormal pathology, functional activation or functional connectivity.

The aim of the experimental component of this work was to attempt to determine if the diffusion of water in the brain is fractional in nature, using diffusion weighted magnetic resonance imaging. The diffusion imaging sequences were designed to vary the diffusion weighting gradients in a number of ways, to test thoroughly the ability of the fractional diffusion model to describe the diffusion process in the brain. To this end a number of experimental designs were applied in both human and rat brain, and the resultant data was analysed using the expressions developed in the previous chapters.

A 3T Gradient Echo experiments

Instrumentation

The experiments with human subjects were carried out using a Philips Achieva (Philips Medical Systems, Eindhoven NL.) wholebody clinical MRI scanner, with a static magnetic field of 3T, created by a liquid helium cooled superconducting magnet. The scanner is equipped with a gradient coil system capable of producing linear field gradients up to 50 mT/m. The coil system can produce gradients in three orthogonal directions. A sensitivity encoding head RF transceiver coil was used. The homogeneity of the static field was optimised for each subject using an automatic shimming routine.

Subjects

The experiments were performed on healthy human volunteers. The studies were approved by the institutional ethics committee, and written informed consent was obtained. The total scan time did not exceed 1 hour. The volunteers were shielded from the acoustic noise using earplugs and headphones. The headphones also facilitated communication between the subject and the control room at all times. The subject was provided with an alarm button which could be activated at any time to signal that they wished to terminate the experiment.

Sequence Design

Numerous sophisticated diffusion imaging sequences have been developed since the original experiments of Stejskel and Tanner [36]. The typical method employed to increase diffusion weighting (or b-value see Eq.(65)), is to increase the diffusion gradient strength, G. In order to sample the hypothesized fractional nature of the water diffusion in the brain, diffusion sequences were designed

where the increasing diffusion weighting was achieved by increasing the duration of the diffusion gradient. Diffusion gradient shapes other than simple trapezoidal gradients were also incorporated in the customized sequence design. For the same subjects the measured diffusion coefficients should be the same for experiments with varying diffusion gradient strength, duration and shape, if the fractional diffusion model is to be a good fit of the experimental data.

Four customized pulse sequences were prepared, to fully explore the suitability of the anomalous diffusion model, to describe the diffusion behavior in human brain tissue. Each employed a gradient echo multi-shot echo-planar imaging sequence with a repetition time of 2s and an echo time of 64.2 ms. While a spin-echo sequence would be preferred for diffusion imaging due to improved image quality, time was a limiting factor in these experiments. To minimize the echo time while applying diffusion gradients with a large enough duration to produce a high diffusion weighting, required the minimum achievable time for the other sequence components. The gap required between the diffusion gradient lobes in the spin echo sequence would have resulted in an unacceptably long echo time and severe degradation of image quality. A sensitivity encoding factor of two was also employed to minimize the echo time. Ten 4 mm axial slices with a field-of-view of 23 cm x 23 cm were acquired to encompass the whole brain. 10 diffusion weightings were repeated sequentially a total of 30 times for each slice for averaging purposes. Inversion recovery images of each subject were also acquired as a map of grey and white matter, from which regions of interest could be chosen for analysis. The diffusion weighting gradients were applied in the axial direction only, thus the directional sensitivity of white matter was not explored.

The first sequence applied a bipolar diffusion weighting gradient, with

trapezoidal gradient shape. After acquiring a b_0 image, each gradient lobe increased in duration from 12 to 24ms in steps of 1.5ms. With a gradient strength of 50mT/m used for each gradient, this produced an effective range of b-values of 200 - 1600 s mm^{-2}.

The second sequence also used a customized gradient echo EPI sequence, however the bipolar diffusion weighting gradients now had a fixed duration of 24ms and the gradient strength was varied over eights steps from 8 mT/m to 48mT/m, producing a maximum b-value of 1440 s mm^{-2}.

The third customized sequence used ramped shape gradients, as described in earlier chapters. The duration of these gradients was varied over the same range as the trapezoidal gradients, from 12 ms to 24ms after the acquisition with no diffusion weighting (b_0). A maximum gradient strength of 50mT/m was also chosen. However in this case, due to the gradient shape, a much lower range of b-values was achieved, 90 - 670 s mm^{-2}.

The fourth experiment was designed to include the triangular gradients described in the previous chapter. The maximum gradient strength of these gradients was also 50 mT/m and the duration of the gradients varied over the range used for the previous experiments. Due to the requirement that human subjects should spend no more than 1 hour in the scanner, it was not possible to include this sequence design in the data acquisition, and it was applied to the water phantom experiments only.

To assess the performance of the fractional expressions in measuring mono-exponential behaviour, each customized sequence was used to acquire diffusion image data with a spherical phantom filled with water, before use on human subjects. These images were analyzed to ensure that expected values for the fitting parameters (D and α) were obtained. It was predicted that the value of $\alpha \approx 1$ and $D \approx 2.4 \times 10^{-3} mm^2 s^{-1}$ would be measured. These measurements

were used to validate each step of the process from the sequence programming, to the curve fitting, and the derivation of the fitting expressions.

Analysis

Post-processing and fitting were performed using IDL 7.0 (ITT Visual Information Solutions, Boulder, CO, USA). Before fitting was performed the average of the 30 repetitions of each diffusion weighting value was calculated. The signal decay curves created by the increasing gradient duration in each pixel, were fitted to the appropriate fractional diffusion expression, as well as the Bennett stretched exponential equation for comparison. Bounds were placed on the parameter α such that $0 < \alpha < 1$. The fitting was performed using the Levenberg-Marquardt algorithm [127] as implemented in IDL to provide values for D and α. This algorithm minimises the cost function

$$C = \sum_{i=1}^{n} (y_i - f(\vec{x}_i, \vec{a}))^2, \tag{181}$$

where y_i is the experimental diffusion data of length n, $f(\vec{x}_i, \vec{a})$ is the fitting function to evaluate the variables $\vec{a} = [D, \alpha]$. The parameters returned for each diffusion weighted image pixel were then displayed as an image. A fit was rejected which did not achieve a chi-squared goodness-of-fit of < 0.001.

B 7T Spin Echo experiments

All animal imaging was performed on a Bruker Biospin animal MR system with a 7T static magnetic field and a 30cm bore (Bruker Biospin, Ettlingen, Germany). Male Wistar rats (n=3), one aged 4 months, (young) and two aged 20-24 (aged) months were used for these experiments in accordance with

the protocols approved by the Trinity College Dublin ethics committee and the Irish Department of Health. The animals were anaesthetized using isoflurane gas (1.5-2% at 1L min $^{-1}$ of oxygen) administered via a facemask during each experiment. The rat was placed on a fibreglass cradle and the animal's temperature was monitored with a rectal thermometer. The temperature was maintained by application of a warming surface, controlled by a water pump driven temperature regulator (SA Instruments Inc., Stony Brook, NY, USA). A mechanical ventilator (Ugo Basile, Comerio, VA, Italy) was used to provide adequate inflowing gas to the facemask and the respiration signal was monitored using custom hardware and software (SA Instruments Inc., Stony Brook, NY, USA).

Imaging Sequence

Due to the higher gradient capability it was possible to perform diffusion imaging with increasing gradient duration on the Bruker system using a spin-echo sequence. Spin-echo sequences have the advantage of reducing the effects of static field inhomogeneities. Using a much higher gradient strength, *b*-values over 2000 s mm^{-2} could be achieved while maintaining a very short echo time of 20.2 ms. These factors resulted in the appearance of significantly higher image quality in the animal experiments.

Diffusion weighting was achieved using a Stejskal-Tanner spin echo preparation with two trapezoidal gradients, one on each side of the 180^o refocussing pulse. Seven separate diffusion weighted acquisitions were performed, each with an increasing *b*-value. The strength of the diffusion gradients was maintained at 90mT/m, while the duration of the gradients was increased from 0 s to 6 s in steps of 1s. This created an effective range of *b*-values of 0 - 2177 s mm^{-2}. The acquisition was performed with a repetition time of 1.2 s , an echo

time of 20.2 ms and an RF flip angle of 90^o. The gradients were separated by 9.5 ms. The diffusion weighting was applied in all three directions at once. A 3 cm $\times$ 3 cm field-of-view was chosen, and six 1.5 cm slices were acquired.

The IDl implementation of the Levenberg-Marquardt algorithm was also used for the fitting of these acquisitions to the fractional spin-echo diffusion equation.

VI Results of experimental investigation

A Water phantom assessment

The assessment of the performance of the fractional expression in the analysis of monoexponential behaviour was carried out using the images acquired with the spherical water phantom. Each of the customized imaging sequences were applied, and subsequently five regions-of-interest were chosen and the appropriate version of the anomalous diffusion expression was used to fit the diffusion decay;

$$\ln\left[\frac{S(t)}{S_0}\right] = -2\gamma^2 G^2 D \frac{t^{\alpha+2}}{(2+\alpha)\Gamma(1+\alpha)} \quad \textit{(Rectangular)} \tag{182}$$

$$\ln\left[\frac{S(t)}{S_0}\right] = -D\gamma^2 G^2 \frac{(2\delta)^{2-\alpha}\alpha(\alpha+3)}{\Gamma(5+\alpha)} \quad \textit{(Ramped)} \tag{183}$$

$$\ln\left[\frac{S(t)}{S_0}\right] = -\frac{D\gamma^2 G^2 \delta^{2+\alpha}}{8\Gamma(5+\alpha)}(3+\alpha)(12+\alpha(24+9\alpha+\alpha^2)) \quad \textit{(Triangular)} \tag{184}$$

Values of α and D were obtained. A sample image of the water phantom with no diffusion weighting is shown in Fig.18.

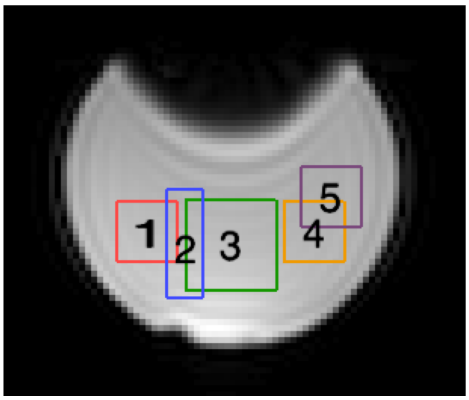

Figure 18: A b_0 image of the spherical water phantom with regions-of-interest which were used for fitting purposes highlighted and labelled 1-5.

The fit of the logarithm of the normalized signal to the fractional diffusion equation showed monoexponential signal attenuation in every region of interest. The mean value of α over all three experiments and all four fitted functions was 0.997, with a standard deviation of 0.005. A typical attenuation curve can be seen in Fig. 19 and 20, along with the fractional fit to the data. The water molecules are experiencing free diffusion, unhindered by any boundaries or collisions with large molecules. Fig. 19 and 20 shows the fit using the bipolar Eq. (182) which in the case of free diffusion ($\alpha = 1$), reduces to Eq. (65).

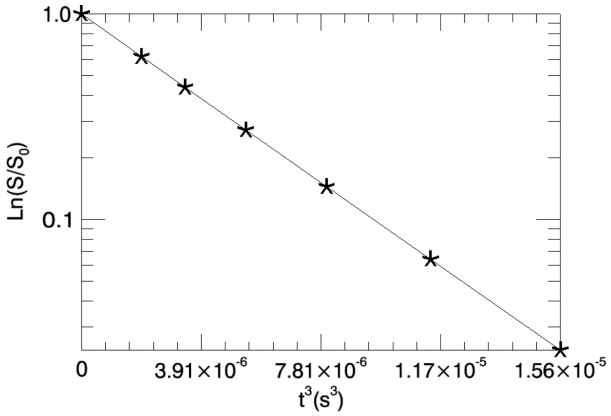

Figure 19: The diffusion decay observed in the water phantom with the application of the diffusion sequence with the bipolar rectangular gradients of increasing duration. $*$ represents the data points, the solid line shows the fit of Eq. (182)

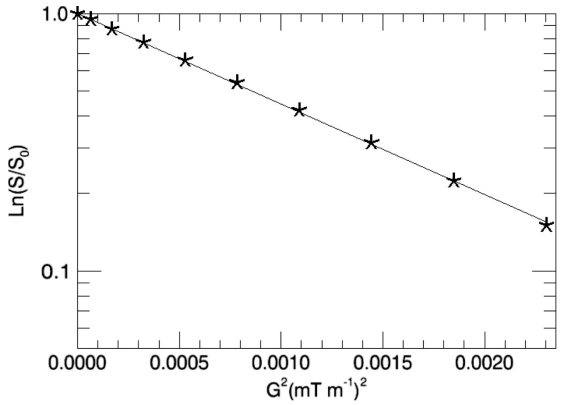

Figure 20: The $*$ represent the diffusion decay in the diffusion experiment where once again rectangular gradients were employed but their strength was increased instead of their duration. The solid line represents the fit using the gradient echo fractional diffusion expression Eq (182).

Table 1 and Fig. 21 show the values of α obtained for each region of interest, for each experimental design. A fit of the stretched exponential expression [40] against the increasing gradient duration experiment with the rectangular gradient shape was also calculated for comparison.

$$\frac{S(t)}{S(0)} = \exp\big(- (bD_{DC})^{\alpha}\big) \tag{185}$$

The value for α is ~ 1, as expected for free diffusion.

ROI	1	2	3	4	5	Average
Rectangular	1.000	0.984	1.000	0.982	1.000	0.992
Triangular	0.998	0.997	0.999	0.999	1.0	0.999
Ramped	0.999	0.999	0.999	0.999	0.999	0.999
Stretched Exp.	1.002	0.995	1.004	0.995	1.000	0.999

Table 1: Fitted values of the parameter α for the 5 regions in the water phantom

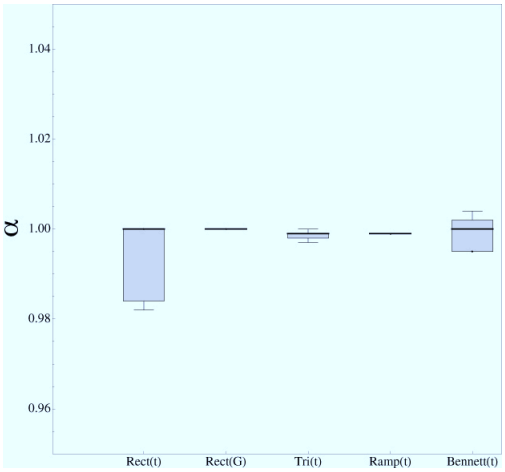

Figure 21: A boxplot illustrating the values of α as listed in Table 1

Table 2 shows the values of the diffusion coefficient from the fitting of the water phantom data. The diffusion coefficient of pure water at 25°C is 2.4 $\times 10^{-3} mm^2 s^{-1}$. The average chi-squared goodness-of-fit value for these results (Tables 1 and 2) was 4.6 $\times 10^{-5}$.

ROI	1	2	3	4	5	Average
Rectangular	2.11	1.97	2.11	1.99	2.12	2.06
Triangular	2.14	2.15	2.14	2.15	2.15	2.146
Ramped	2.14	2.14	2.12	2.13	2.12	2.13
Stretched Exp.	2.18	2.08	2.25	2.07	2.15	2.15

Table 2: Fitted values of $D \times 10^{-3}(mm^2 s^{-1})$ for the 5 ROIs in the water phantom.

B Investigation of fractional diffusion equation *in vivo*

In diffusion weighted MRI we assume that the diffusion coefficient of the sample under investigation is constant throughout the experiment. In neuronal tissue we can be reasonably confident that while on a microscopic level, small changes in D are occurring, when averaged over the voxel dimensions, the changes may be negligible. It follows that the only cause of the variation in the magnitude of the acquired signal are the experimental parameters i.e. the magnitude, duration or shape of the diffusion weighting gradients. Thus it should be possible to vary any of the characteristics of the diffusion gradients and, if the appropriate mathematical expression is applied, a similar value of the diffusion coefficient for the same sample should be obtained.

The sequence designs for the experiments in human neuronal tissue were intended to vary the diffusion weighting in a variety of ways, while employing simple methods. All components of the sequences with the exception of diffusion gradient design were identical. Grey and white matter tissue was differentiated using inversion recovery images. An example of an inversion recovery image is shown in Fig. 22. An inversion recovery sequence provides strong contrast between tissues with different T_1 relaxation times, such as grey and white matter.

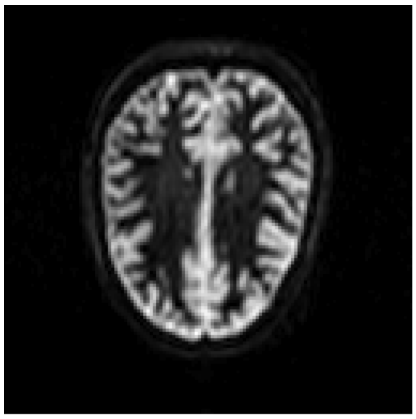

Figure 22: An inversion recovery image contrasting grey and white matter.

In Figs 23 – 28, maps of the fitted parameters (D and α) from the fit of the fractional equation (Eq. (182)) are shown for every tissue voxel in an image slice. The same slice in the same subject was chosen across each of the three experiments, with variable duration, variable strength and variable shaped diffusion weighting gradients. Next to each map is a histogram displaying the frequency of occurrence of particular values of the parameters, as a percentage of the total fitted voxels. The fractional diffusion equations fitted the majority of the voxels containing tissue, with a chi-squared goodness–of–fit of < 0.001. The broadness of the distributions of the fitted parameters for grey and white matter can be attributed to the relatively crude tissue differentiation provided by the inversion recovery image. The image voxels would contain both cerebrospinal fluid (CSF) and partial volume effects (multiple tissue types in the same voxel). The mean values of the distributions are collated in Table 3. It was conjectured that the non-monoexponential behaviour might not be observed in the ramped gradient experiments, due to the much lower b-values which were achieved. Published literature suggests that the deviation from monoexponential behaviour is observed only at much higher b-values, > 2000 s mm^2.

	grey Matter		White Matter	
	$D \times 10^{-3}$ (mm^2 s^{-1})	α	$D \times 10^{-3}$ (mm^2 s^{-1})	α
Rectangular with increasing duration	0.48 ± 0.16	0.79 ± 0.07	0.39 ± 0.18	0.75 ± 0.09
Rectangular with increasing strength	0.45 ± 0.19	0.8 ± 0.11	0.37 ± 0.2	0.76 ± 0.12
Ramped with increasing duration	0.49 ± 0.16	0.55 ± 0.16	0.40 ± 0.17	0.58 ± 0.17

Table 3: A summary of the mean values of the histograms of D and α displayed in Figs 23 – 28

The mean diffusion coefficients from each experiment are in good agreement. The coefficient α is consistent between the increasing duration and increasing strength experiments, but significantly lower in the ramped gradient experiment. As discussed above, a much lower range of diffusion weightings was achieved in this experiment, as a result of gradient shape. Thus the extent of the diffusion decay curve which was sampled using this gradient design, was much reduced in comparison to the other two experiments. The fit of Eq.(182) to the increasing duration rectangular gradients was repeated, using only the images with the same degree of diffusion weighting as the ramped experiment. In this case a lower range of α was also obtained; 0.59 ± 0.1. While this is a good indication that the lower α-values in the ramped experiment are due to the lower diffusion weighting, the broader distribution could also indicate that such a gradient shape is more sensitive to eddie current or partial volume effects.

It is interesting that this sequence design can produce the same calculated value of the diffusion coefficient by means of a lowered α coefficient, without the requirement for very high b-values. The results of these experiments validate

the application of the fractional diffusion equations to describe the signal decay observed in the diffusion weighted imaging of human neuronal tissue. Overall the diffusion coefficients calculated were in very good agreement across each experiment, producing similar values of D irrespective of whether gradient duration, strength or shape was varied.

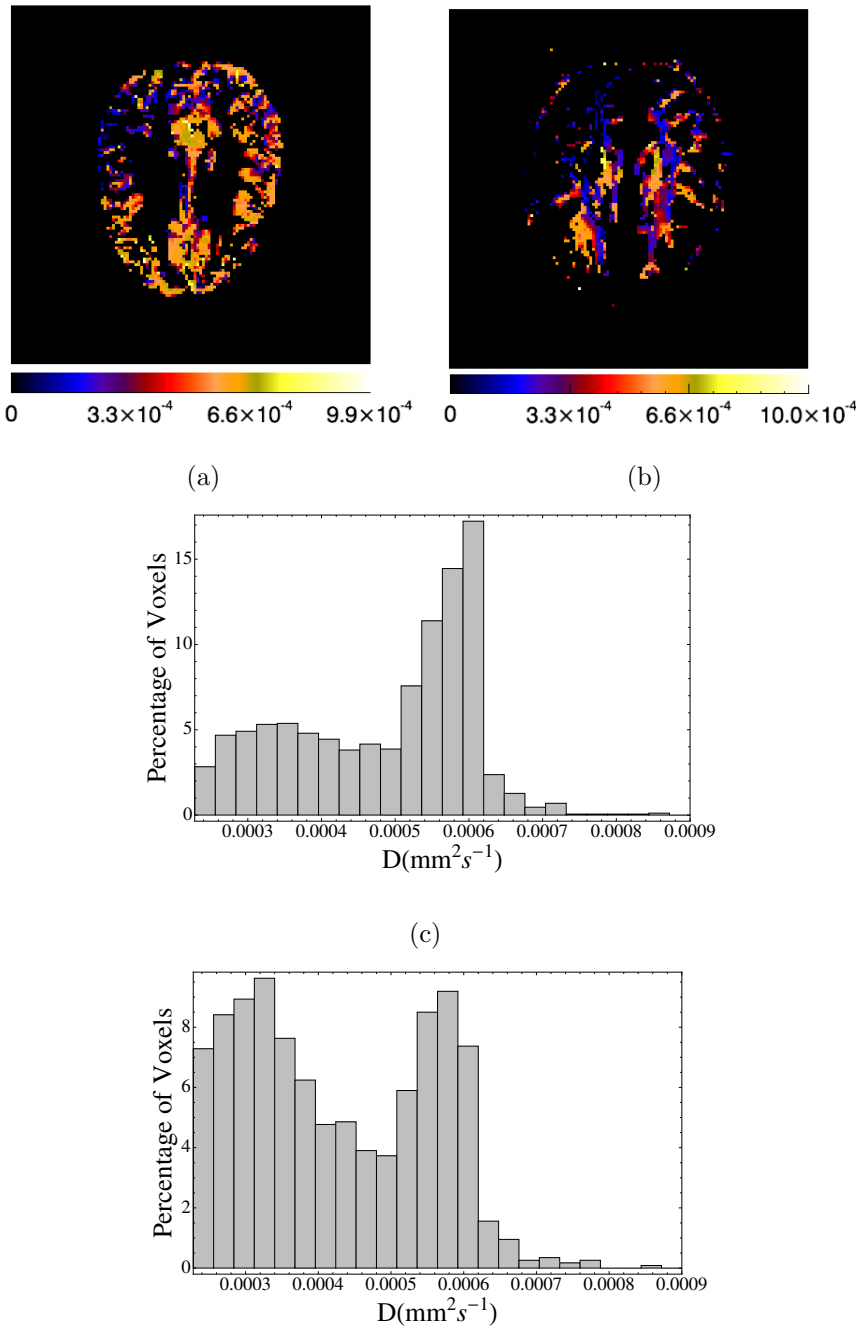

Figure 23: (a) A map of the diffusion coefficients in grey matter for the gradient echo experiment with rectangular gradients where t was the variable, fit using the anomalous diffusion equation. (b) A map of the diffusion coefficients in white matter for the same experiment. (c) A histogram plot of the distribution of diffusion coefficients in the map, with a mean of $0.0.48 \pm 0.16 \times 10^{-3}$ mm^2 s^{-1}. (d) A histogram plot of (b) with a mean of $0.39 \pm 0.18 \times 10^{-3}$ mm^2 s^{-1}.

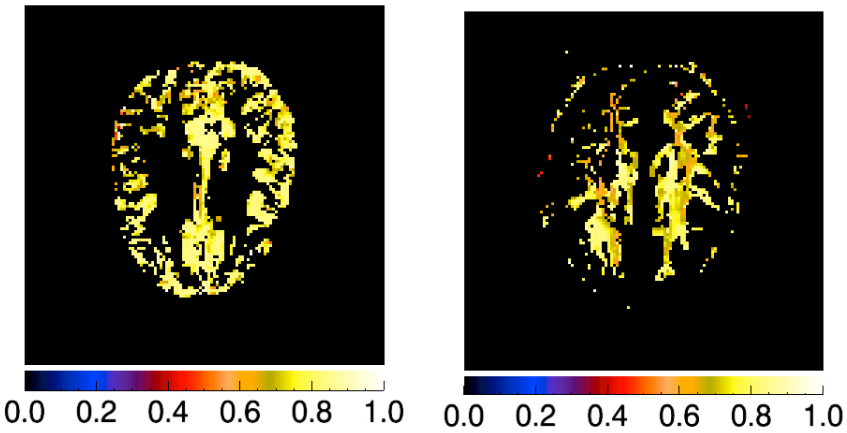

(a) (b)

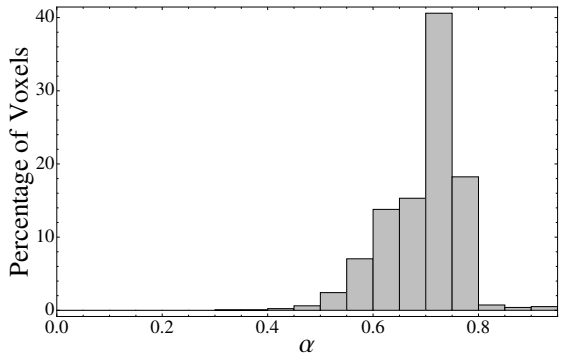

(c)

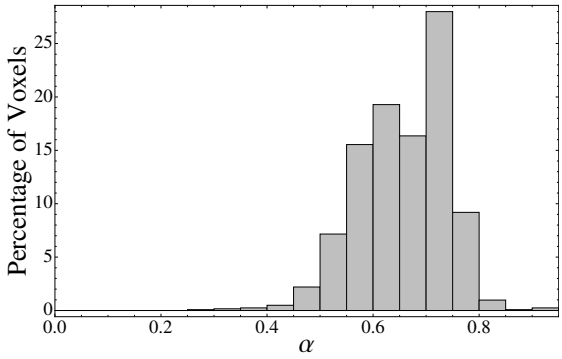

(d)

Figure 24: (a) A map of α for the varying duration experiment with rectangular gradients. (b) The distribution of α in white matter elements of the brain tissue for the increasing duration rectangular diffusion gradient design. (c) A frequency distribution of the values of α in (a) with a mean of 0.79 ± 0.07. (d) A histogram plot of (a) with a mean of 0.75 ± 0.09

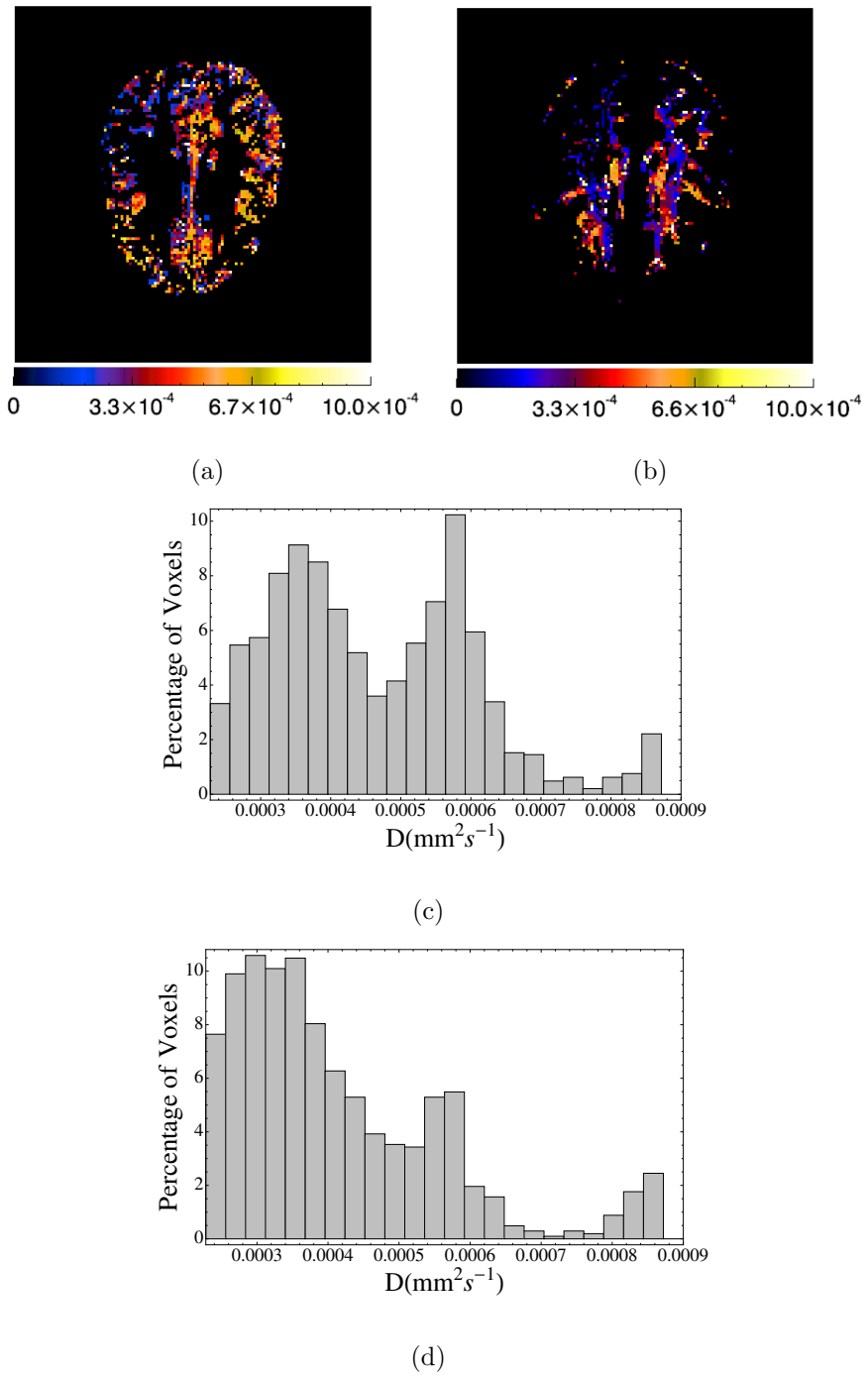

Figure 25: (a) A map and histogram plot of the diffusion coefficients obtained in grey matter for each voxel, from the gradient echo experiment with rectangular gradients where the gradient strength was the variable.(b) The fitted diffusion coefficients for the increasing gradient strength experiment in the white matter regions of the brain. (c) A histogram plot of the distribution of diffusion coefficients in (a) with a mean of $0.45 \pm 0.19 \times 10^{-3}$ mm^2 s^{-1}. (d) A frequency distribution of the values in (b) with mean $0.37 \pm 0.2 \times 10^{-3}$ mm^2 s^{-1}.

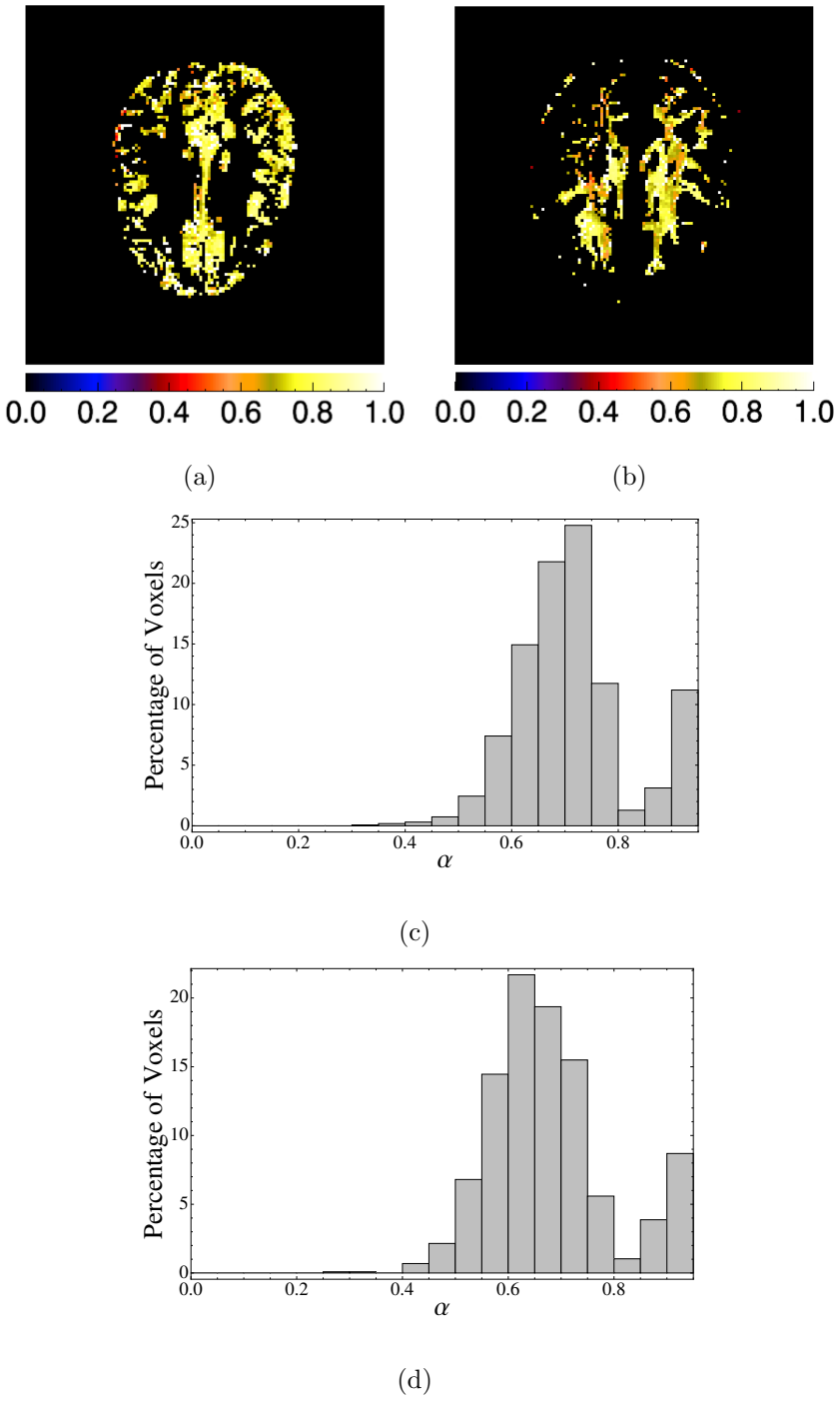

Figure 26: (a) The fitted parameter α for the increasing gradient strength experiment in grey matter. (b) A map of α from the increasing gradient strength experiment in white matter. (c) A histogram of the distribution of alpha coefficients in the map with a mean of 0.8 $\pm$ 0.11. (d) A frequency distribution of (b) with a mean of 0.76 $\pm$ 0.12.

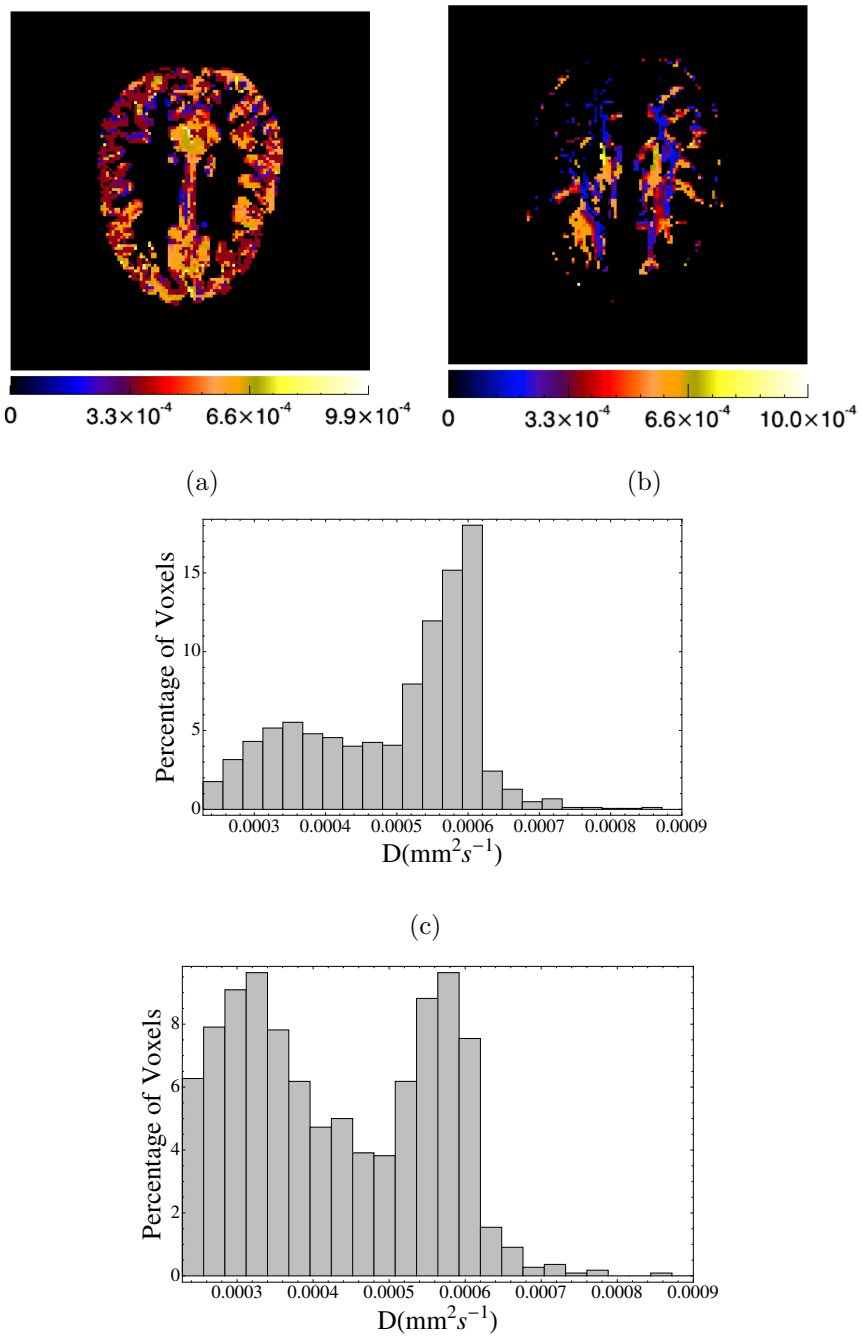

Figure 27: (a) A map of the parameter D for grey matter, and a histogram of the distribution from the gradient echo experiment with the ramped gradient shapes with variable duration. (b) The distribution of diffusion coefficients in white matter in the ramped gradient experiment. (c) A histogram of the distribution of diffusion coefficients in (a) with a mean of $0.49 \pm 0.16 \times 10^{-3}$ mm^2 s^{-1}. (d) A histogram plot of (b) with mean $0.4 \pm 0.17 \times 10^{-3}$ mm^2 s^{-1}.

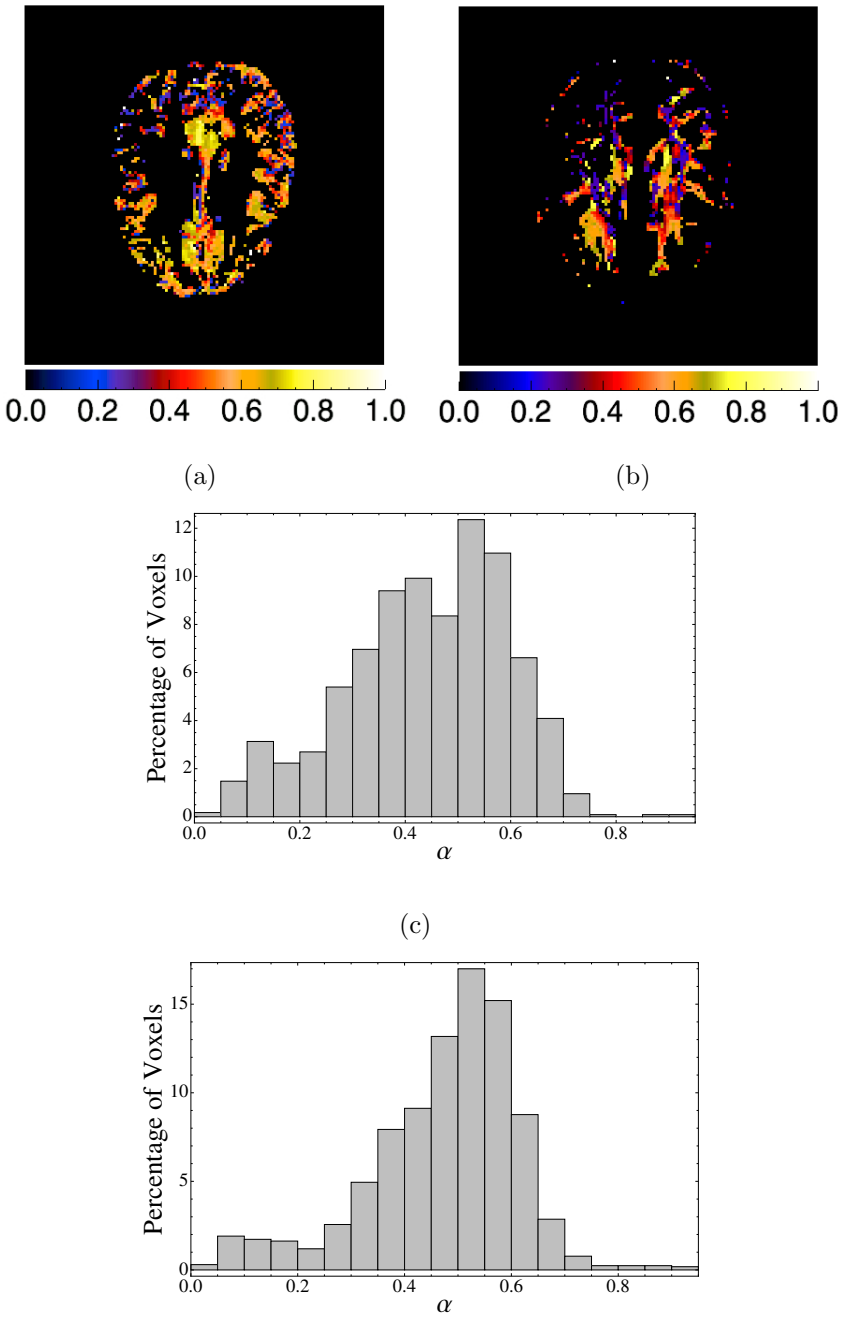

Figure 28: (a) The distribution of α in the ramped gradient experiment in grey matter. (b) The distribution of α in the ramped gradient experiment in the white matter regions of the brain. (c) A histogram of (a) with a mean of 0.55 ± 0.16 (d) A frequency distribution of (b) with mean value of α 0.58 ± 0.17.

Spin Echo DW experiments at 7T

These experiments were performed to assess the suitability of the anomalous expression for the spin-echo experiment to describe the diffusion process in the rat brain at 7T. The rat brain is a simpler structure than the human brain, being composed primarily of grey matter. Due to the improved gradient capability of the 7T scanner, it was possible to apply stronger gradients for a shorter time than was available on the human scanner. These factors, in conjunction with the use of the spin-echo sequence, resulted in improved quality of the images, when compared to the human experiments. The spin-echo version of the fractional diffusion equation was applied in this case,

$$\ln\left[\frac{S(t)}{S_0}\right] = \gamma^2 D \frac{G^2\delta^2}{\Gamma(1+\alpha)}\left[\frac{2\delta^\alpha}{2+\alpha} + (\Delta-\delta)^\alpha\right] \tag{186}$$

In each of the three animal experiments a mid-brain slice was chosen. Fig. 29 is an example of a spin-echo image from the experiment on the young rat, with no diffusion weighting i.e. the b_0 image. A summary of the fitted parameters for each animal is shown in Table 4

	D $\times 10^{-3}$ mm^2 s^{-1}	α
1	0.67 ± 0.12	0.63 ± 0.2
2	0.59 ± 0.18	0.72 ± 0.28
3	0.7 ± 0.18	0.7 ± 0.24

Table 4: Mean values of the fitted parameters D and α for the three experiments performed on the 7T animal scanner.

Further maps of the fitted parameters for the two additional animal acquisitions can be found in Appendix **??**. The maps in Fig 30 show low heterogeneity

in the cortex, in agreement with the results of Bennett *et al* [40]. Some subtle heterogeneity is observed in the maps of the diffusion coefficients. It would be of interest for future work to investigate if there is a trend in the values of the fitted parameters between young and aged animals. Significantly larger numbers of animals would be required for such a study. The narrower distribution of fitted parameter values, when compared to the human experiments, is likely to be partially due to the reduced complexity of the rat brain, but also a result of the superior image quality.

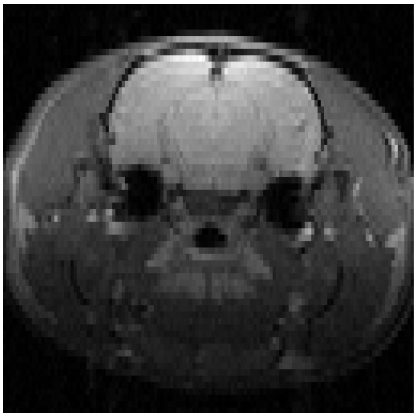

Figure 29: A midbrain slice from the first animal with no diffusion weighting.

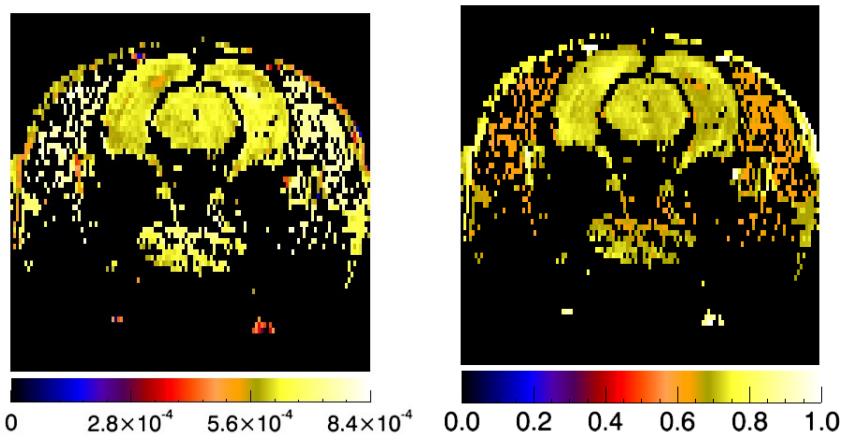

(a) Map of D (b) Map of α

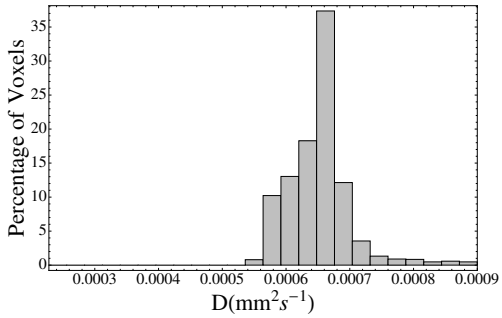

(c) Histogram of D

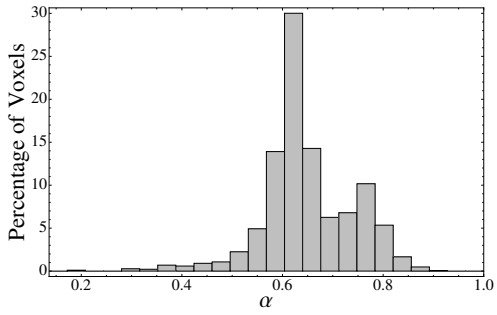

(d) Histogram of α

Figure 30: (a) A map of the diffusion coefficients obtained from fitting the spin-echo expression to the image data acquired on the animal imaging system. (b) An image distribution illustrating the values of α obtained when fitting the anomalous expression to the spin-echo diffusion decay. (c) A plot of the frequency distribution of the values in (a) with mean $0.67 \pm 0.12 \times 10^{-3}$ mm^2 s^{-1}. (d) A plot of the frequency distribution of the values displayed in (b) with mean 0.63 ± 0.2.

C Comparison of fractional diffusion equations to a classical approach

In order to compare the results of the fractional diffusion equations with a method of analysis based on the classical (i.e. normal diffusion) approach, the stretched exponential expression was fitted to the image data from the experiment which employed rectangular gradients with increasing gradient duration. It is apparent that the fractional Langevin equation could form a possible microscopic basis for the results observed with the stretched exponential expression. The maps and frequency distributions of the fitted parameters D and α from the stretched exponential expression and the fractional diffusion equation are compared for grey matter in Figs 31 and 32. The Figs comparing the equations in white matter can be found in Appendix **??**.

	D $\times 10^{-3}$ mm^2 s^{-1}
Bennet Eq. Grey Matter	0.42 $\pm$ 0.14
Fractional Eq. Grey Matter	0.48 $\pm$ 0.19
Bennett Eq. White Matter	0.37 $\pm$ 0.14
Fractional Eq. White Matter	0.39 $\pm$ 0.17

Table 5: Mean values of the fitted parameters D and α obtained by fitting the stretched exponential expression and the fractional diffusion equation (Eq. (182)) to the first experiment i.e. rectangular gradients of increasing duration.

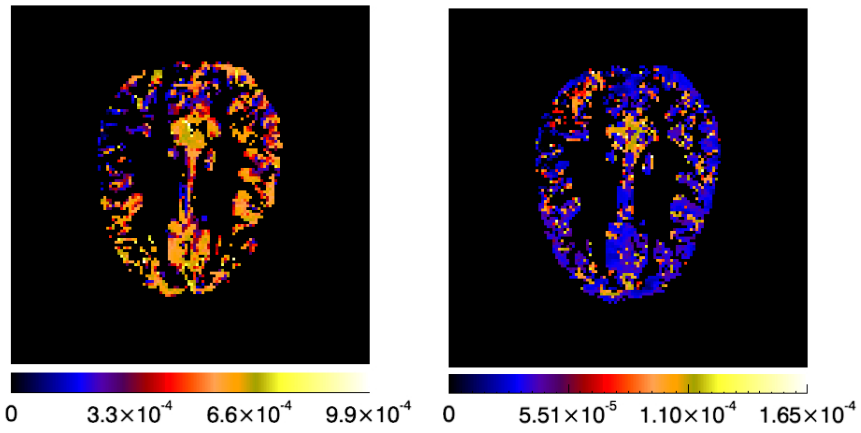

(a) Map of D, fractional eq. (b) Map of D, stretched exponential.

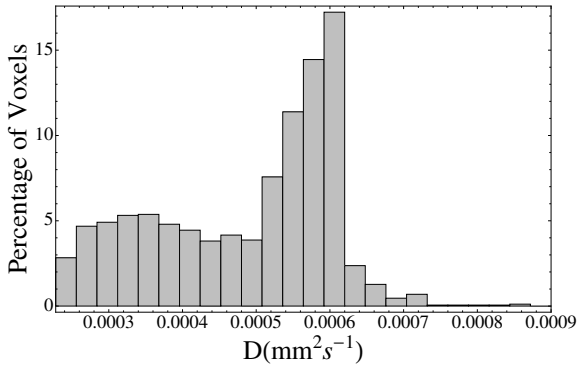

(c) Histogram of D, fractional fit.

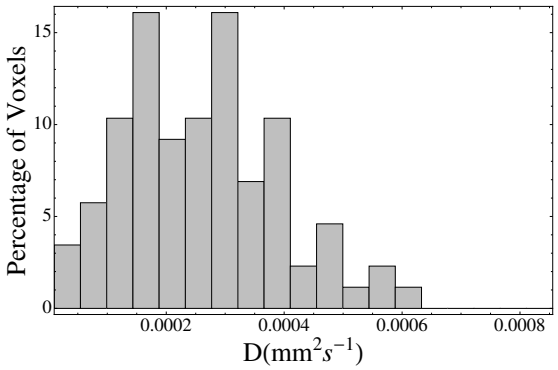

(d) Histogram of D, stretched exp.

Figure 31: A comparison (in grey matter) of the calculated diffusion coefficients using 31(a) the fractional diffusion equation and 31(b) the stretched exponential equation. (a) shows a map of the parameter D using the fractional diffusion equation (b) shows a map of the parameter D using the stretched exponential equation (c) is a frequency distribution of the values displayed in (a) with a mean of $0.48 \pm 0.19 \times 10^{-3}$ mm^2 s^{-1} (d) is a histogram of the mapped values in (b) with a mean of $0.42 \pm 0.14 \times 10^{-3}$ mm^2 s^{-1}.

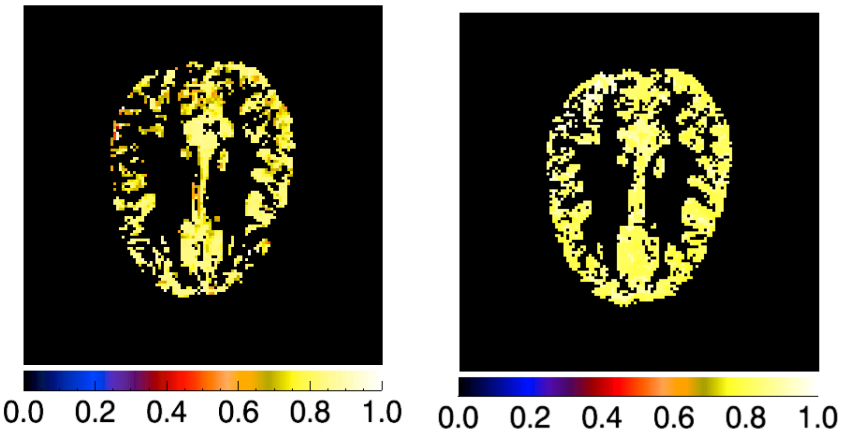

(a) Map of α, fractional fit (b) Map of α, stretched exponential

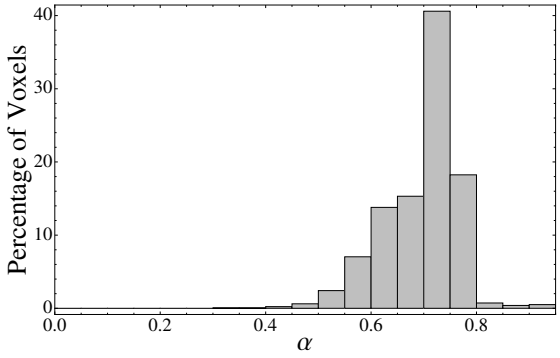

(c) Histogram of α, fractional fit

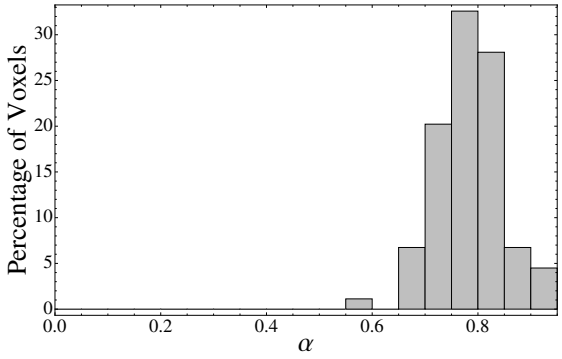

(d) Histogram of α, stretched exp

Figure 32: (a) A map of α (in white matter) for fractional equation fit. (b) The α parameter for each voxel as estimated from the Bennett stretched exponential expression (c) A frequency distribution of the values of α in (a) with a mean of 0.79 $\pm$ 0.07. (d) The frequency distribution for (b) has a mean of 0.87 $\pm$ 0.07.

These results provide additional validation of the fractional diffusion equations, as another more classical approach produces similar diffusion coefficients from the same image data. The values of α produced by the fitting of the stretched exponential expression were in general higher than those obtained with the fractional equation, but these parameters are not directly comparable.

In order to compare the goodness-of-fit of the stretched exponential, fractional diffusion and biexponential (Eq.(77) the most widely used equation in the literature) equations, analysis was performed on the sum of the squared residuals for fitted regions of interest in all nine subjects. Ten 2 voxel $\times$ 2 voxel ROIs were chosen, 5 in grey matter and 5 in white matter, throughout the ten brain slices of the nine subjects. The stretched exponential, fractional and biexponential equations were fitted to each region and the sum of the squared residuals or standard error (SE) was calculated. Two examples are shown (Fig. 33) of the three equations fit to the same ROI.

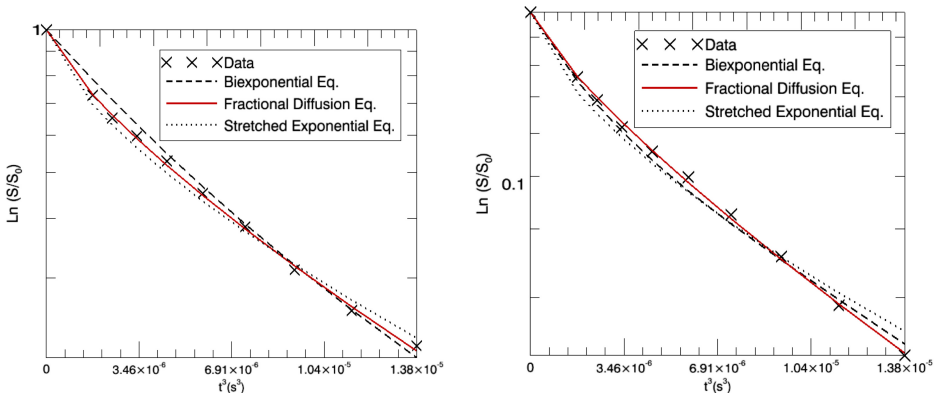

(a) Sample ROI 1.

(b) Sample ROI 2.

Figure 33: Two sample plots of the signal decay in two ROI's, with each of the three equations fitted to the data.

In Fig 34 (a) – (f) frequency distributions of the difference between the sums of the squared residuals for the various equations are displayed. In Figs 34(a) – 34(d), negative values indicate that the sum-of-squared residuals was

lower for the fits with the fractional diffusion equation. In Figs 34(e) and 34(f) the negative values indicate a better fit by the biexponential equation. 91% of grey matter voxels and 92% of white matter voxels had lower standard errors with the fractional diffusion fit when compared to the bexponential fit. 68% of grey matter and 84% of white matter voxels had lower sum-of-squared residuals when compared to the stretched exponential equation. The biexponential and stretched exponential were also compared using this image data, and 56% of grey matter and 55% of white matter were better fitted with the biexponential equation than the stretched exponential.

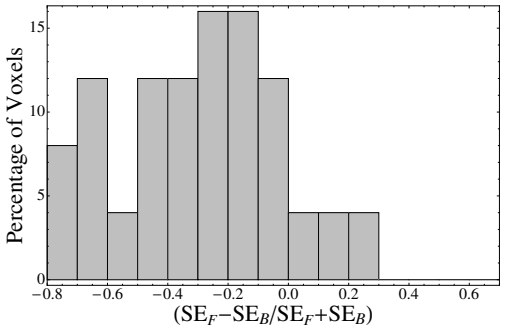

(a) Fractional *vs* biexponential fit in GM

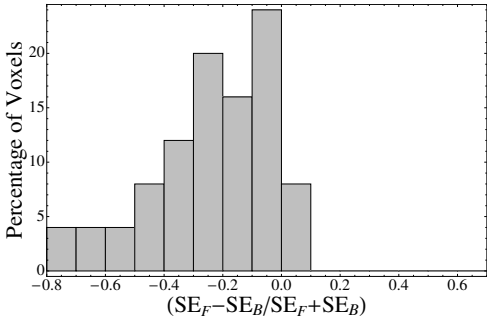

(b) Fractional *vs* biexponential fit in WM

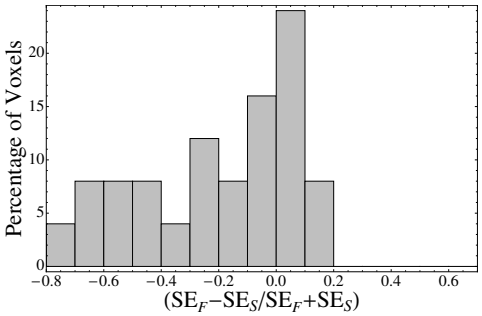

(c) Fractional *vs* stretched exp. fit in GM

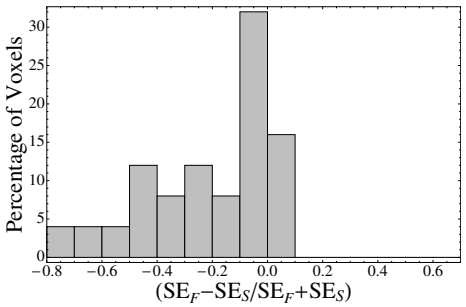

(d) Fractional *vs* stretched exp. fit in WM

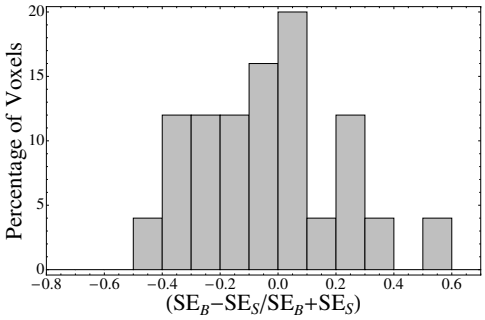

(e) Biexp. *vs* stretched exp. fit in GM

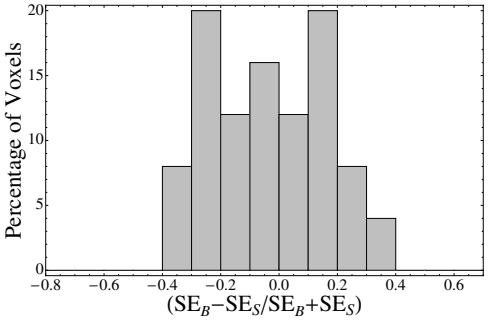

(f) Biexp. *vs* stretched exp. fit in WM

Figure 34: Frequency distributions for a comparison of goodness-of-fit of the fractional, stretched and biexponential equations to the image data from nine human subjects, where SE_F is the sum of the squared residuals for the fractional equation, SE_B is the standard error for the biexponential equation and SE_S is that for the stretched exponential model. Negative values indicate lower sum-of-squared residuals for the first quoted equation.

D Conclusions

The sequence design, and fitting of the fractional diffusion equation were validated using a phantom containing freely diffusing water which produced acceptable values of the diffusion coefficients and a value of $\alpha = 1$, which is the expected value for freely diffusing protons. The application of the fractional equation to the description of water diffusion in neuronal tissue was further justified by the variation of the diffusion weighting gradients. Despite the much lower diffusion weighting achieved with the ramped gradient shape, consistent values of the diffusion coefficient were calculated for the same signal decay for each experiment. The fractional diffusion equation was found to fit the experimental data very accurately and when compared with two other equations, performed significantly better. The spin-echo version of the fractional diffusion equation (Eq.(186)) was successfully fitted to rat neuronal tissue images from a 7T MRI scanner.

This study has shown that the fractional equation will fit experimental data robustly in healthy human and animal subjects, future work must include an assessment of its performance in clinical and neuroscientific studies when compared to the equations which are currently favoured.

VII Discussion

In this thesis it has been shown how the magnetization dephasing in magnetic resonance imaging arising from the Brownian motion of the nuclei in a reservoir of infinite extent may be determined by simply writing the Langevin equation for the phase random variable and then calculating its characteristic function [1]. The method yields in transparent fashion, from the properties of the characteristic function of Gaussian random variables, the classical dephasing results of Carr and Purcell [29], Torrey [28], and Stejskal and Tanner [36] for normal diffusion, which are based on the diffusion limit of the discrete time random walk proposed by Einstein [18]. Moreover it is easily generalized to include the inertia of the nuclei, in which the underlying statistics are governed by the Ornstein-Uhlenbeck process [116] and to other more complicated situations where the nuclei move in a field of potential $V(r)$. Hence we have a microscopic explanation of the dephasing process in free water, namely it results from the nucleus behaving as a random walker executing a jump of finite mean square length, at uniform time intervals, so that the only variable is the orientation of the walker.

The method may also be extended to anomalous diffusion in a transparent fashion, in order to provide a possible microscopic justification for the use of stretched exponentials to describe the dephasing in tissue. Namely, the anomalous diffusion may ultimately have its origin in memory effects giving rise to fractional Brownian motion, i.e. the nucleus behaves as a random walker in a fractal heat bath. This process naturally introduces the new fitting parameter, α , indicating the role played by fractional dynamics in the time for the complex diffusion which is observed in human neuronal tissue. In normal diffusion, $\alpha = 1$, and we have the classical expressions [29, 28, 36] once more.

The calculation is accomplished using the fractional Langevin equation

for the translational Brownian motion proposed by Lutz [2] which supposes that the random force in that equation is Gaussian, so that the properties of characteristic functions of Gaussian random variables may once again be used to calculate the dephasing, yielding a fractional generalization of the results of Refs.[28, 29, 36].

The signal attenuation due to the diffusion of water protons in diffusion weighted magnetic resonance imaging has been analysed using a fractional diffusion equation, which assumes that the water protons under study are experiencing a fractal heat bath. As expected, the fractional parameter α was approximately one for the fits to voxels containing freely diffusing protons. In experiments in both human and animal neuronal tissue the parameter α was measured to be $0.3 < \alpha < 0.9$. Therefore, in the complex tissue environment, the time dependence of the signal decay is not cubic, but in the range of $t^{2.3} \rightarrow t^{2.9}$. The experimental validation of the fractional diffusion equation was performed by varying many of the experimental design parameters, and it was demonstrated that consistent values of the fitting parameters were produced. The equation was compared to the stretched exponential equation and the biexponential equation and in both cases proved a better fit to the experimental data. It has been shown previously that the diffusion behaviour in the cellular environment is subdiffusive [38, 40, 66, 67, 69, 70, 73, 75] using both MRI and non-imaging methods. The methods which have been outlined here propose one possible microscopic explanation for the observed subdiffusion, however the conclusions must be tempered by the fact that other relaxation processes, such as those arising from restricted normal diffusion, may give rise to apparently anomalous behaviour.

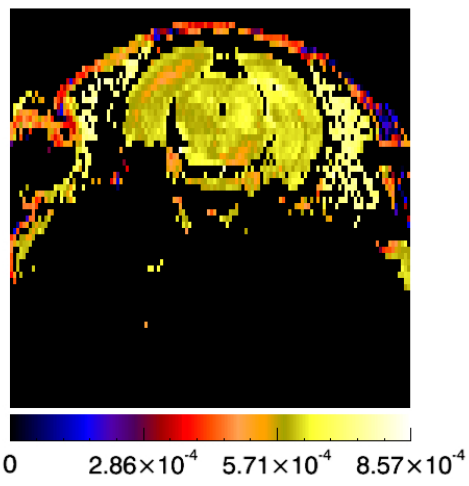

(a) Map of D

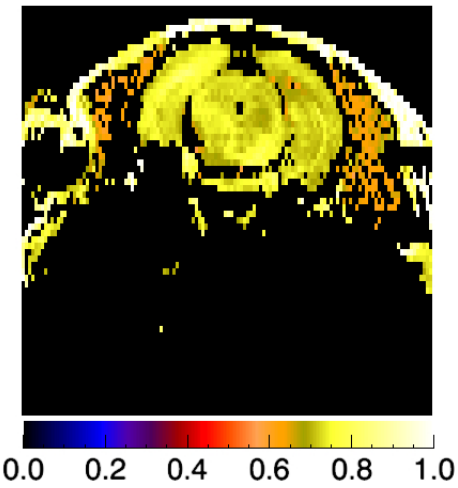

(b) Map of α

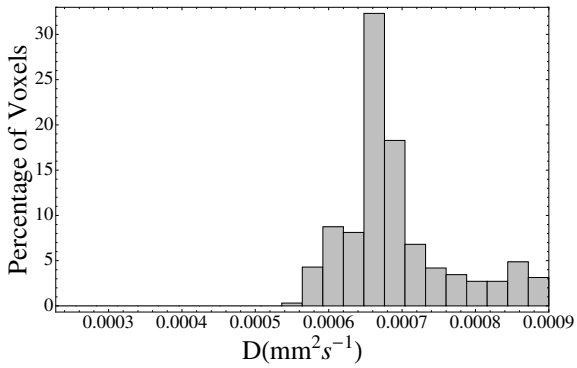

(c) Histogram of D

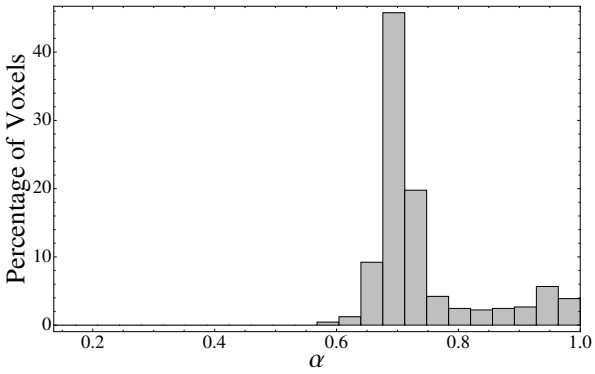

(d) Histogram of α

Figure 35: Second animal (a) A map of the diffusion coefficients, D (mm^2 s^{-1}), for each voxel. (b) A map of α image for the second animal. (c) A histogram of the values displayed in (a) $0.59 \pm 0.18 \times 10^{-3}$ mm^2 s^{-1} (d) A histogram of the frequency of the values shown in (b) with mean 0.72 ± 0.28.

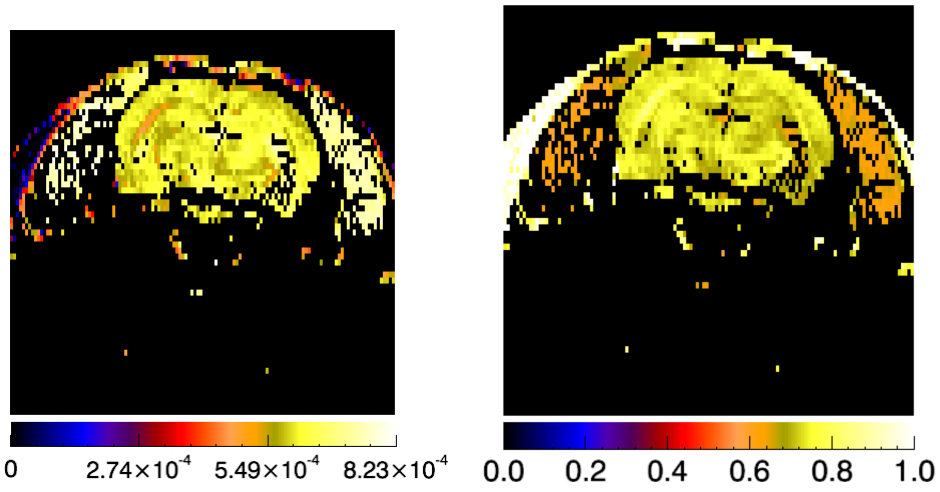

(a) Map of D (b) Map of α

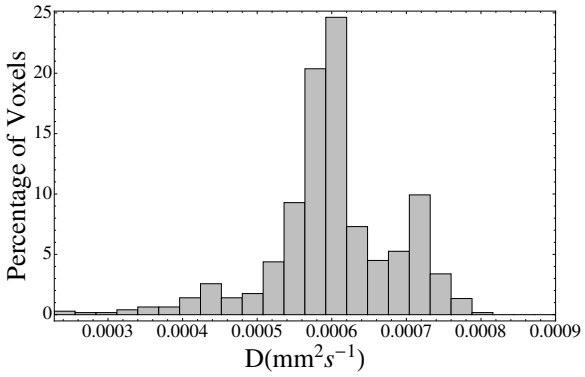

(c) Histogram of D

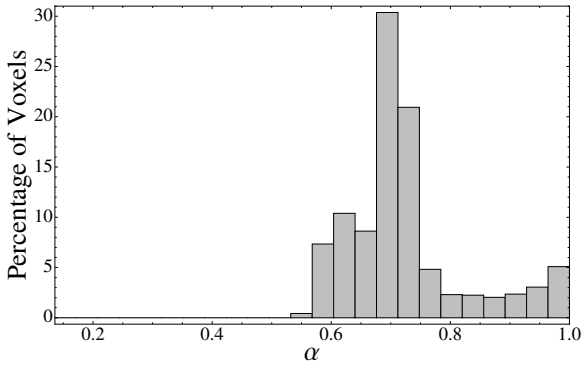

(d) Histogram of α

Figure 36: Third animal (a) Distribution of diffusion coefficients through a single slice for the third animal. (b) Distribution of α for a slice in the third rat. (c) A histogram of the frequency of the diffusion coefficients shown in (a) $0.7 \pm 0.18 \times 10^{-3}$ mm^2 s^{-1}. (d) A histogram of the frequency of the values in (b) with a mean of 0.7 ± 0.24.

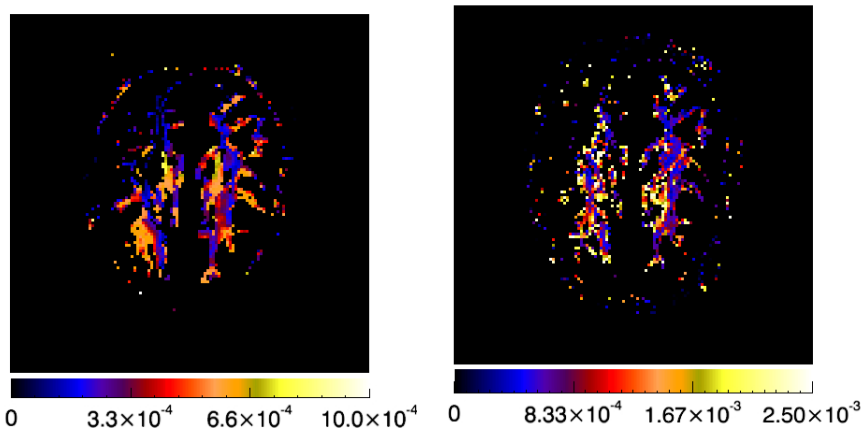

(a) Map of D, fractional eq. (b) Map of D, stretched exp.

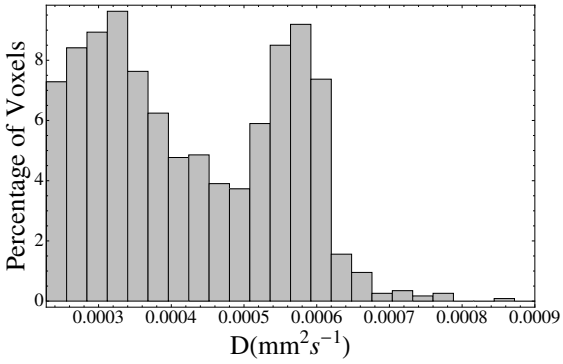

(c) Histogram of D, fractional eq.

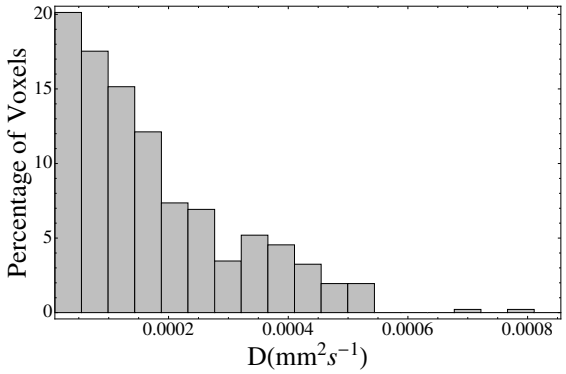

(d) Histogram of D, stretched exp.

Figure 37: (a) A map of the diffusion coefficients in white matter for the rectangular gradient experiment with variable duration using the fractional diffusion equation. (b) The distribution of diffusion coefficients in white matter as produced by the stretched exponential expression.(c) A histogram plot of (a) with a mean of $0.39 \pm 0.18 \times 10^{-3}$ mm^2 s^{-1}. (d) A histogram plot of (b) with $0.37 \pm 0.14 \times 10^{-3}$ mm^2 s^{-1}.

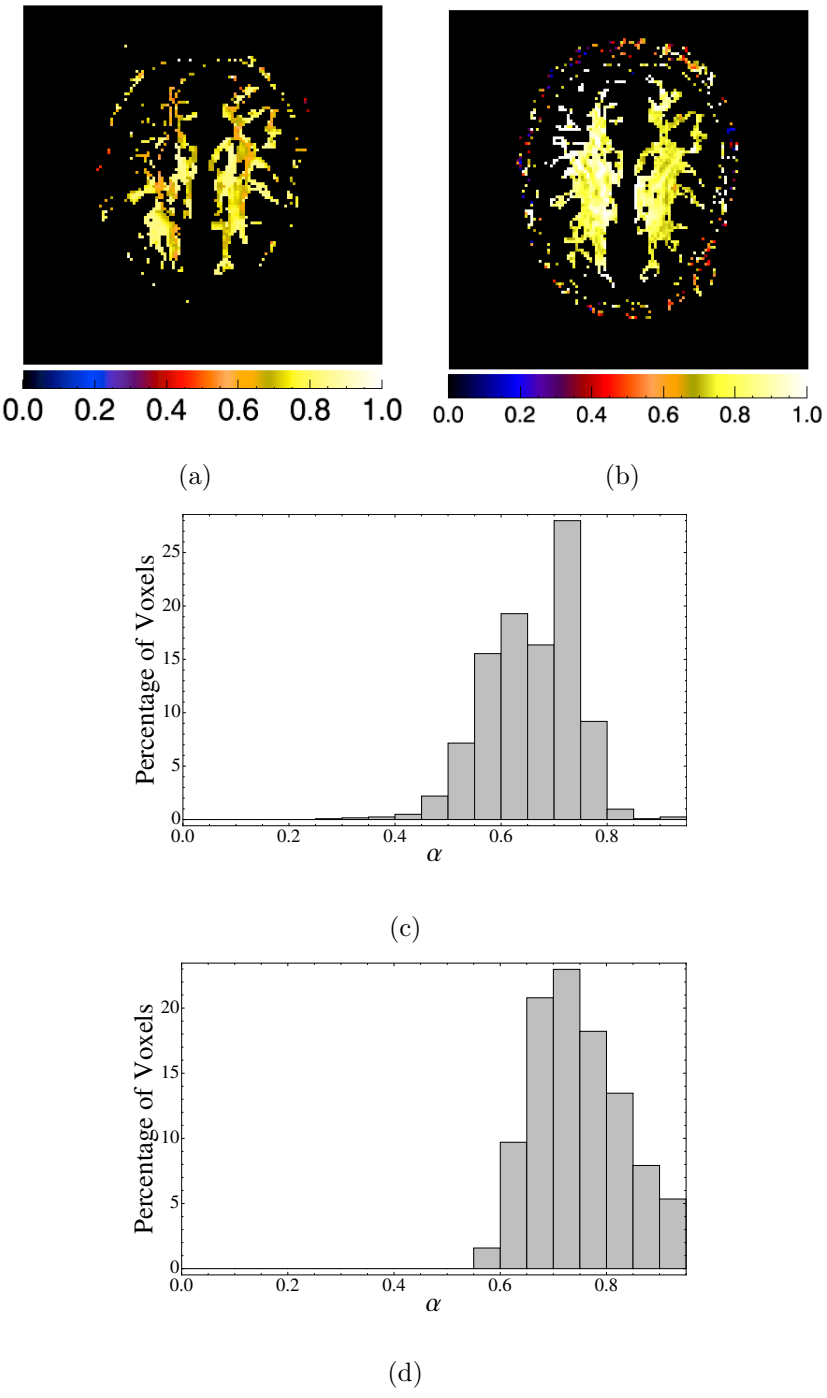

Figure 38: (a)The distribution of α in white matter regions of the brain for the fractional diffusion equation fit. (b) The distribution of α as obtained by fitting the stretched exponential expression to the white matter regions of the brain from the rectangular experiment with varying duration. (c) A histogram plot of (a) with a mean of 0.75 $\pm$ 0.09 (d) A histogram plot of the distribution of α in the map (b) with a mean of 0.84 $\pm$ 0.09

List of Abbreviations

ADC	Apparent diffusion coefficient
ATP	Adenosine-triphosphate
BOLD	Blood oxygenation level dependent
CSF	Cerebrospinal fluid
CTRW	Continuous time random walk
DTI	Diffusion tensor imaging
DW MRI	Diffusion Weighted Magnetic Resonance Imaging
EPI	Echo planar imaging
FA	Fractional anisotropy
fMRI	Functional magnetic resonance imaging
KWW	Kohlrausch–Williams–Watts
MS	Multiple sclerosis
NMR	Nuclear magnetic resonance
pdf	Probability distribution function
PGSE	Pulsed gradient spin echo
r.m.s.	Root mean square
RARE	Rapid acquisition with relaxation enhancement
RF	Radiofrequency
TE	Echo time

Bibliography

[1] J.M. Cooke, Y.P. Kalmykov, W.T. Coffey, and C.M. Kerskens. Langevin equation approach to diffusion magnetic resonance imaging. *Physical Review E*, 80(6):61102, 2009.

[2] E. Lutz. Fractional Langevin equation. *Physical Review E*, 64(5):51106, 2001.

[3] B.B. Mandelbrot and J.W. van Ness. Fractional Brownian motions, fractional noises and applications. *SIAM review*, 10(4):422–437, 1968.

[4] R Metzler and J Klafter. The restaurant at the end of the random walk: recent developments in the description of anomalous transport by fractional dynamics. *J.Phys.A*, 37:R161–R208, 2004.

[5] ME Moseley, J. Kucharczyk, J. Mintorovitch, Y. Cohen, J. Kurhanewicz, N. Derugin, H. Asgari, and D. Norman. Diffusion-weighted MR imaging of acute stroke: correlation with T2-weighted and magnetic susceptibility-enhanced MR imaging in cats. *American Journal of Neuroradiology*, 11(3):423–429, 1990.

[6] A. Darquié, J.B. Poline, C. Poupon, H. Saint-Jalmes, and D. Le Bihan. Transient decrease in water diffusion observed in human occipital cortex during visual stimulation. *Proceedings of the National Academy of Sciences*, 98(16):9391– 9395, 2001.

[7] PJ Basser, J. Mattiello, and D. LeBihan. MR diffusion tensor spectroscopy and imaging. *Biophysical Journal*, 66(1):259–267, 1994.

[8] R. Bammer and F. Fazekas. Diffusion imaging in multiple sclerosis. *Neuroimaging Clinics of North America*, 12(1):71–106, 2002.

[9] M. Maeda, Y. Kawamura, Y. Tamagawa, T. Matsuda, S. Itoh, H. Kimura, T. Iwasaki, N. Hayashi, K. Yamamoto, and Y. Ishii. Intravoxel incoherent motion (IVIM) MRI in intracranial, extraaxial tumors and cysts. *J Comput Assist Tomogr*, 16(4):514–518, 1992.

[10] F. Bloch. Nuclear induction. *Phys. Rev.*, 70(7-8):460–474, Oct 1946.

[11] E. L. Hahn. Spin echoes. *Phys. Rev.*, 80(4):580–594, Nov 1950.

[12] E. Nelson. *Dynamical theories of Brownian motion*. Princeton University Press, Princeton, NJ, 1967.

[13] M. Kac. Random walk and the theory of Brownian motion. *The American Mathematical Monthly*, 54(7):369–391, 1947.

[14] MD Haw. Colloidal suspensions, Brownian motion, molecular reality: a short history. *Journal of Physics Condensed Matter*, 14(33):7769–7779, 2002.

[15] M.C. Wang and GE Uhlenbeck. On the theory of the Brownian motion II. *Reviews of Modern Physics*, 17(2-3):323–342, 1945.

[16] W. Coffey. Development and application of the theory of Brownian motion. *Advances in chemical physics*, 63:69–252, 1985.

[17] W. Ebeling, E. Gudowska-Nowak, and I.M. Sokolov. On Stochastic Dynamics in Physics—Remarks on History and Terminology. *Acta Physica Polonica B*, 39(5):1003, 2008.

[18] W.T. Coffey, Y.P. Kalmykov, and J.T. Waldron. *The Langevin Equation 2nd Ed.* World Scientific River Edge, NJ, 2004.

[19] R. Kubo, M. Toda, and N. Hashitsume. *Statistical Physics II: Nonequilibrium statistical mechanics 2nd Ed.* Springer Verlag, Berlin, 1991.

[20] R.M. Mazo. *Brownian motion: fluctuations, dynamics, and applications.* Oxford University Press, Oxford, 2002.

[21] W.T. Coffey. Dielectric relaxation: an overview. *Journal of Molecular Liquids*, 114(1-3):5–25, 2004.

[22] R. Metzler and J. Klafter. The random walk's guide to anomalous diffusion: a fractional dynamics approach. *Physics Reports*, 339(1):1 – 77, 2001.

[23] W.T. Coffey, D.S.F. Crothers, D. Holland, and S.V. Titov. Green function for the diffusion limit of one-dimensional continuous time random walks. *Journal of Molecular Liquids*, 114(1-3):165–171, 2004.

[24] W. Paul and J. Baschnagel. *Stochastic processes: from physics to finance.* Springer Verlag, Berlin., 1999.

[25] F. Bloch. The principle of nuclear induction. *Science*, 118(3068):425 – 430, 1953.

[26] A. Abragam. *The Principles of Nuclear Magnetism.* Oxford University Press, London, 1961.

[27] R.K. Wangsness and F. Bloch. The Dynamical Theory of Nuclear Induction. *Physical Review*, 89:728–739, 1953.

[28] H.C. Torrey. Bloch equations with diffusion terms. *Physical Review*, 104(3):563–565, 1956.

[29] HY Carr and EM Purcell. Effects of diffusion on free precession in nuclear magnetic resonance experiments. *Physical Review*, 94(3):630–638, 1954.

[30] D.S. Grebenkov. NMR survey of reflected Brownian motion. *Reviews of Modern Physics*, 79(3):1077–1137, 2007.

[31] M.A. Bernstein, K.F. King, and X.J. Zhou. *Handbook of MRI Pulse Sequences*. Academic Press, New York, 2004.

[32] D. Le Bihan. *Diffusion and perfusion magnetic resonance imaging: applications to functional MRI*. Raven Press, New York, 1995.

[33] P.E. Chen, J.E. Simon, M.D. Hill, C.H. Sohn, P. Dickhoff, W.F. Morrish, R.J. Sevick, and R. Frayne. Acute Ischemic Stroke: Accuracy of Diffusion-weighted MR ImagingEffects of b Value and Cerebrospinal Fluid Suppression1. *Radiology*, 238(1):232 – 239, 2006.

[34] M.L. García-Martín, P. Ballesteros, and S. Cerdán. The metabolism of water in cells and tissues as detected by NMR methods. *Progress in Nuclear Magnetic Resonance Spectroscopy*, 39(1):41–77, 2001.

[35] D. Le Bihan, E. Breton, D. Lallemand, P. Grenier, E. Cabanis, and M. Laval-Jeantet. MR imaging of intravoxel incoherent motions: application to diffusion and perfusion in neurologic disorders. *Radiology*, 161(2):401–407, 1986.

[36] EO Stejskal and JE Tanner. Spin diffusion measurements: spin echoes in the presence of a time-dependent field gradient. *The Journal of Chemical Physics*, 42:288, 1965.

[37] TP Das and AK Saha. Mathematical Analysis of the Hahn Spin-Echo Experiment. *Physical Review*, 93(4):749–756, 1954.

[38] R.L. Magin, O. Abdullah, D. Baleanu, and X.J. Zhou. Anomalous diffusion expressed through fractional order differential operators in the Bloch–Torrey equation. *Journal of Magnetic Resonance*, 190(2):255, 2008.

[39] R.V. Mulkern, H. Gudbjartsson, C.F. Westin, H.P. Zengingonul, W. Gartner, C.R.G. Guttmann, R. Robertson, W. Kyriakos, R. Schwartz, D. Holtzman, et al. Multi-component apparent diffusion coefficients in human brain. *NMR in Biomedicine*, 12(1):51–62, 1999.

[40] K.M. Bennett, K.M. Schmainda, R. Bennett, D.B. Rowe, H. Lu, and J.S. Hyde. Characterization of continuously distributed cortical water diffusion rates with a stretched-exponential model. *Magnetic Resonance in Medicine*, 50(4):727–734, 2003.

[41] T. Niendorf, R.M. Dijkhuizen, D.G. Norris, M. van Lookeren Campagne, and K. Nicolay. Biexponential diffusion attenuation in various states of brain tissue: implications for diffusion-weighted imaging. *Magnetic Resonance in Medicine*, 36(6):847 – 857, 1996.

[42] C.A. Clark and D. Le Bihan. Water diffusion compartmentation and anisotropy at high b values in the human brain. *Magnetic Resonance in Medicine*, 44(6):852–859, 2000.

[43] BA Inglis, EL Bossart, DL Buckley, ED Wirth, and TH Mareci. Visualization of neural tissue water compartments using biexponential diffusion tensor MRI. *Magnetic Resonance in Medicine*, 45(4):580–587, 2001.

[44] S.E. Maier, P. Bogner, G. Bajzik, H. Mamata, Y. Mamata, I. Repa, F.A. Jolesz, and R.V. Mulkern. Normal Brain and Brain Tumor: Multicom-

ponent Apparent Diffusion Coefficient Line Scan Imaging. *Radiology*, 219(3):842 – 849, 2001.

[45] R.V. Mulkern, S.J. Haker, and S.E. Maier. On high b diffusion imaging in the human brain: ruminations and experimental insights. *Magnetic Resonance Imaging*, 27(8):1151–1162, 2009.

[46] A. Schwarcz, P. Bogner, P. Meric, J.L. Correze, Z. Berente, J. Pal, F. Gallyas, T. Doczi, B. Gillet, and J.C. Beloeil. The existence of biexponential signal decay in magnetic resonance diffusion-weighted imaging appears to be independent of compartmentalization. *Magnetic Resonance in Medicine*, 51(2):278–285, 2004.

[47] T.Q. Duong, J.V. Sehy, D.A. Yablonskiy, B.J. Snider, J.J.H. Ackerman, and J.J. Neil. Extracellular apparent diffusion in rat brain. *Magnetic Resonance in Medicine*, 45(5):801–810, 2001.

[48] J.V. Sehy, A.A. Banks, J.J.H. Ackerman, and J.J. Neil. Importance of intracellular water apparent diffusion to the measurement of membrane permeability. *Biophysical journal*, 83(5):2856–2863, 2002.

[49] Y. Assaf and Y. Cohen. Non-Mono-Exponential Attenuation of Water andN-Acetyl Aspartate Signals Due to Diffusion in Brain Tissue. *Journal of Magnetic Resonance*, 131(1):69–85, 1998.

[50] D.A. Yablonskiy, G.L. Bretthorst, and J.J.H. Ackerman. Statistical model for diffusion attenuated MR signal. *Magnetic resonance in medicine: official journal of the Society of Magnetic Resonance in Medicine/Society of Magnetic Resonance in Medicine*, 50(4):664 – 669, 2003.

[51] J.H. Jensen, J.A. Helpern, A. Ramani, H. Lu, and K. Kaczynski. Diffusional kurtosis imaging: the quantification of non-gaussian water diffusion by means of magnetic resonance imaging. *Magnetic Resonance in Medicine*, 53(6):1432–1440, 2005.

[52] V.G. Kiselev and K.A. Il'yasov. Is the" biexponential diffusion" biexponential? *Magnetic Resonance in Medicine*, 57(3):464 – 469, 2007.

[53] M.M. Cheung, E.S. Hui, K.C. Chan, J.A. Helpern, L. Qi, and E.X. Wu. Does diffusion kurtosis imaging lead to better neural tissue characterization? A rodent brain maturation study. *Neuroimage*, 45(2):386–392, 2009.

[54] MW Evans, GJ Evans, WT Coffey, and P. Grigolini. *Molecular dynamics*. Wiley Interscience, New York, 1982.

[55] K.M. Bennett, J.S. Hyde, and K.M. Schmainda. Water diffusion heterogeneity index in the human brain is insensitive to the orientation of applied magnetic field gradients. *Magnetic resonance in medicine*, 56(2):235–239, 2006.

[56] M.G. Hall and T.R. Barrick. From diffusion-weighted MRI to anomalous diffusion imaging. *Magnetic Resonance in Medicine*, 59(3):447–455, 2008.

[57] E. Özarslan, P.J. Basser, T.M. Shepherd, P.E. Thelwall, B.C. Vemuri, and S.J. Blackband. Observation of anomalous diffusion in excised tissue by characterizing the diffusion-time dependence of the MR signal. *Journal of Magnetic Resonance*, 183(2):315–323, 2006.

[58] KB Oldham and J. Spanier. *The Fractional Calculus*. Academic Press, New York, 1974.

[59] D. Häussinger. The role of cellular hydration in the regulation of cell function. *Biochemical Journal*, 313(3):697 – 710, 1996.

[60] S. Wieser and G. J. Schütz. Tracking single molecules in the live cell plasma membrane – Do's and Don't's. *Methods*, 46:131–140, Oct 2008.

[61] D.P. Rall, W.W. Oppelt, and C.S. Patlak. Extracellular space of brain as determined by diffusion of inulin from the ventricular system. *Life Sciences*, 1(2):43–48, 1962.

[62] C. Nicholson. Diffusion and related transport mechanisms in brain tissue. *Reports on progress in physics*, 64(7):815–884, 2001.

[63] A. Caspi, R. Granek, and M. Elbaum. Diffusion and directed motion in cellular transport. *Physical Review E*, 66(1):11916–1 – 11916–12, 2002.

[64] A.I. García-Pérez, E.A. López-Beltrán, P. Klüner, J. Luque, P. Ballesteros, and S. Cerdán. Molecular crowding and viscosity as determinants of translational diffusion of metabolites in subcellular organelles. *Archives of biochemistry and biophysics*, 362(2):329–338, 1999.

[65] J. Wu and K.M. Berland. Propagators and time-dependent diffusion coefficients for anomalous diffusion. *Biophysical Journal*, 95(4):2049–2052, 2008.

[66] G. Guigas and M. Weiss. Sampling the Cell with Anomalous Diffusion-The Discovery of Slowness. *Biophysical Journal*, 94(1):90–94, 2008.

[67] G. Guigas, C. Kalla, and M. Weiss. Probing the nanoscale viscoelasticity of intracellular fluids in living cells. *Biophysical journal*, 93(1):316–323, 2007.

[68] M. Weiss, M. Elsner, F. Kartberg, and T. Nilsson. Anomalous subdiffusion is a measure for cytoplasmic crowding in living cells. *Biophysical journal*, 87(5):3518–3524, 2004.

[69] I. Golding and E.C. Cox. Physical nature of bacterial cytoplasm. *Physical review letters*, 96(9):98102 – 98106, 2006.

[70] D.S. Banks and C. Fradin. Anomalous diffusion of proteins due to molecular crowding. *Biophysical journal*, 89(5):2960–2971, 2005.

[71] M.T. Klann, A. Lapin, and M. Reuss. Stochastic Simulation of Signal Transduction: Impact of the Cellular Architecture on Diffusion. *Biophysical Journal*, 96(12):5122–5129, 2009.

[72] M. Wachsmuth, W. Waldeck, and J. Langowski. Anomalous diffusion of fluorescent probes inside living cell nuclei investigated by spatially-resolved fluorescence correlation spectroscopy. *J. Mol. Biol.*, 298:677–689, May 2000.

[73] M. Köpf, C. Corinth, O. Haferkamp, and TF Nonnenmacher. Anomalous diffusion of water in biological tissues. *Biophysical journal*, 70(6):2950–2958, 1996.

[74] R. Kimmich, W. Unrath, G. Schnur, and E. Rommel. NMR measurement of small diffusion coefficients in the fringe field of superconducting magnets. *Journal of magnetic resonance*, 91(1):136–140, 1991.

[75] M. Köpf, R. Metzler, O. Haferkamp, and TF Nonnenmacher. NMR studies of anomalous diffusion in biological tissues: experimental observation of Lévy stable processes. *Fractals in Biology and Medicine*, 2:354–364, 1998.

[76] CS Johnson. Diffusion ordered nuclear magnetic resonance spectroscopy: principles and applications. *Progress in Nuclear Magnetic Resonance Spectroscopy*, 34(3):203–256, 1999.

[77] P.R. Rau, J. Sellner, S. Heiland, K. Plaschke, P.D. Schellinger, U.K. Meyding-Lamadé, and W.R. Lamadé. Apparent diffusion coefficient in the aging mouse brain: A magnetic resonance imaging study. *Life sciences*, 78(11):1175–1180, 2006.

[78] P.W. Schaefer, P.E. Grant, and R.G. Gonzalez. Diffusion-weighted MR Imaging of the Brain 1. *Radiology*, 217(2):331–345, 2000.

[79] JB Fiebach, O. Jansen, PD Schellinger, S. Heiland, W. Hacke, and K. Sartor. Serial analysis of the apparent diffusion coefficient time course in human stroke. *Neuroradiology(Berlin. Print)*, 44(4):294–298, 2002.

[80] H. Neeb, K. Zilles, and N.J. Shah. Fully-automated detection of cerebral water content changes: study of age-and gender-related H2O patterns with quantitative MRI. *Neuroimage*, 29(3):910–922, 2006.

[81] M. Hoehn, K. Nicolay, C. Franke, and B. van der Sanden. Application of magnetic resonance to animal models of cerebral ischemia. *Journal of Magnetic Resonance Imaging*, 14(5):491–509, 2001.

[82] P. van Gelderen, M.H.M. de Vleeschouwer, D. DesPres, J. Pekar, P.C.M. van Zijl, and C.T.W. Moonen. Water diffusion and acute stroke. *Magnetic Resonance in Medicine*, 31(2):154–154, 1994.

[83] DG Norris, T. Niendorf, M. Hoehn-Berlage, K. Kohno, EJ Schneider, P. Hainz, M. Hropot, and D. Leibfritz. Incidence of apparent restricted diffusion in three different models of cerebral infarction. *Magnetic resonance imaging*, 12(8):1175–1182, 1994.

[84] K.F. Liu, F. Li, T. Tatlisumak, J.H. Garcia, C.H. Sotak, M. Fisher, and J.D. Fenstermacher. Regional variations in the apparent diffusion coefficient and the intracellular distribution of water in rat brain during acute focal ischemia. *Stroke*, 32(8):1897–1905, 2001.

[85] T.Q. Duong, J.J.H. Ackerman, H.S. Ying, and J.J. Neil. Evaluation of extra-and intracellular apparent diffusion in normal and globally ischemic rat brain via 19F NMR. *Magnetic Resonance in Medicine*, 40(1):1–13, 1998.

[86] J. Latt, M. Nilsson, D. van Westen, R. Wirestam, F. Stahlberg, and S. Brockstedt. Diffusion-weighted MRI measurements on stroke patients reveal water-exchange mechanisms in sub-acute ischaemic lesions. *NMR in Biomedicine*, 22(6):619 – 628, 2009.

[87] J. Pfeuffer, S.W. Provencher, and R. Gruetter. Water diffusion in rat brain in vivo as detected at very large b values is multicompartmental. *Magnetic Resonance Materials in Physics, Biology and Medicine*, 8(2):98–108, 1999.

[88] PC Sundgren, Q. Dong, D. Gomez-Hassan, SK Mukherji, P. Maly, and R. Welsh. Diffusion tensor imaging of the brain: review of clinical applications. *Neuroradiology*, 46(5):339–350, 2004.

[89] J. Weber, HP Mattle, O. Heid, L. Remonda, and G. Schroth. Diffusion-weighted imaging in ischaemic stroke: a follow-up study. *Neuroradiology*, 42(3):184–191, 2000.

[90] P. Mukherjee, M.M. Bahn, R.C. McKinstry, J.S. Shimony, T.S. Cull, E. Akbudak, A.Z. Snyder, and T.E. Conturo. Differences between Gray

Matter and White Matter Water Diffusion in Stroke: Diffusion-Tensor MR Imaging in 12 Patients 1. *Radiology*, 215(1):211–220, 2000.

[91] G. Schlaug, B. Siewert, A. Benfield, RR Edelman, and S. Warach. Time course of the apparent diffusion coefficient (ADC) abnormality in human stroke. *Neurology*, 49(1):113–119, 1997.

[92] R. Bammer, S. Skare, R. Newbould, C. Liu, V. Thijs, S. Ropele, D.B. Clayton, G. Krueger, M.E. Moseley, and G.H. Glover. Foundations of advanced magnetic resonance imaging. *NeuroRx*, 2(2):167–196, 2005.

[93] MD Denis Le Bihan, J.F. Mangin, C. Poupon, C.A. Clark, S. Pappata, N. Molko, and MD Hughes Chabriat. Diffusion tensor imaging: concepts and applications. *Journal of magnetic resonance imaging*, 13(4):534–546, 2001.

[94] Y.A. Bhagat and C. Beaulieu. Diffusion anisotropy in subcortical white matter and cortical gray matter: changes with aging and the role of CSF-suppression. *Journal of Magnetic Resonance Imaging*, 20(2):216–227, 2004.

[95] P. Mukherjee and R.C. McKinstry. Diffusion tensor imaging and tractography of human brain development. *Neuroimaging Clinics of North America*, 16(1):19–43, 2006.

[96] DH Salat, DS Tuch, DN Greve, AJW van der Kouwe, ND Hevelone, AK Zaleta, BR Rosen, B. Fischl, S. Corkin, H.D. Rosas, et al. Age-related alterations in white matter microstructure measured by diffusion tensor imaging. *Neurobiology of Aging*, 26(8):1215–1227, 2005.

[97] P.J. Basser, S. Pajevic, C. Pierpaoli, J. Duda, and A. Aldroubi. In

vivo fiber tractography using DT-MRI data. *Magnetic Resonance in Medicine*, 44(4):625–632, 2000.

[98] D. Le Bihan. The wet mind: water and functional neuroimaging. *Phys Med Biol*, 52(7):57–90, 2007.

[99] T. Li and A.W. Song. Fast functional brain signal changes detected by diffusion weighted fMRI. *Magnetic resonance imaging*, 21(8):829–833, 2003.

[100] J. Persson, L. Nyberg, J. Lind, A. Larsson, L.G. Nilsson, M. Ingvar, and R.L. Buckner. Structure-function correlates of cognitive decline in aging. *Cerebral Cortex*, 16(7):907–915, 2006.

[101] D. Head, A.Z. Snyder, L.E. Girton, J.C. Morris, and R.L. Buckner. Frontal-hippocampal double dissociation between normal aging and Alzheimer's disease. *Cerebral Cortex*, 15(6):732, 2005.

[102] C. DeCarli, J. Massaro, D. Harvey, J. Hald, M. Tullberg, R. Au, A. Beiser, R. DAgostino, and P.A. Wolf. Measures of brain morphology and infarction in the Framingham Heart Study: establishing what is normal. *Neurobiology of aging*, 26(4):491–510, 2005.

[103] C.R. Jack Jr and R.C. Petersen. *Structural imaging approaches to Alzheimer's disease*. Totowa, NJ: Humana, 2000.

[104] N. Raz, U. Lindenberger, K.M. Rodrigue, K.M. Kennedy, D. Head, A. Williamson, C. Dahle, D. Gerstorf, and J.D. Acker. Regional brain changes in aging healthy adults: general trends, individual differences and modifiers. *Cerebral Cortex*, 15(11):1676–1689, 2005.

[105] D.A. Drachman. Aging and the brain: a new frontier. *Annals of neurology*, 42(6):819–828, 1997.

[106] A.O. Nusbaum, C.Y. Tang, M.S. Buchsbaum, T.C. Wei, and S.W. Atlas. Regional and global changes in cerebral diffusion with normal aging. *American Journal of Neuroradiology*, 22(1):136 – 142, 2001.

[107] J. Helenius, L. Soinne, J. Perkio, O. Salonen, A. Kangasmaki, M. Kaste, R.A.D. Carano, H.J. Aronen, and T. Tatlisumak. Diffusion-weighted MR imaging in normal human brains in various age groups. *American Journal of Neuroradiology*, 23(2):194 – 199, 2002.

[108] S. Heiland, K. Sartor, E. Martin, H.J. Bardenheuer, and K. Plaschke. In vivo monitoring of age-related changes in rat brain using quantitative diffusion magnetic resonance imaging and magnetic resonance relaxometry. *Neuroscience letters*, 334(3):157–160, 2002.

[109] T.A.G.M. Huisman, A.G. Sorensen, K. Hergan, R.G. Gonzalez, and P.W. Schaefer. Diffusion-weighted imaging for the evaluation of diffuse axonal injury in closed head injury. *Journal of computer assisted tomography*, 27(1):5 – 11, 2003.

[110] Y. Mardor, R. Pfeffer, R. Spiegelmann, Y. Roth, S.E. Maier, O. Nissim, R. Berger, A. Glicksman, J. Baram, A. Orenstein, et al. Early detection of response to radiation therapy in patients with brain malignancies using conventional and high b-value diffusion-weighted magnetic resonance imaging. *Journal of Clinical Oncology*, 21(6):1094 – 1100, 2003.

[111] T.L. Chenevert, L.D. Stegman, J.M.G. Taylor, P.L. Robertson, H.S. Greenberg, A. Rehemtulla, and B.D. Ross. Diffusion magnetic resonance imaging: an early surrogate marker of therapeutic efficacy in brain tumors. *JNCI Cancer Spectrum*, 92(24):2029 – 2036, 2000.

[112] M.A. Horsfield, M. Lai, S.L. Webb, G.J. Barker, P.S. Tofts, R. Turner,

P. Rudge, and D.H. Miller. Apparent diffusion coefficients in benign and secondary progressive multiple sclerosis by nuclear magnetic resonance. *Magnetic Resonance in Medicine*, 36(3):393 – 400, 1996.

[113] A.O. Nusbaum, D. Lu, C.Y. Tang, and S.W. Atlas. Quantitative Diffusion Measurements in Focal Multiple Sclerosis Lesions Correlations with Appearance on TI-Weighted MR Images. *American Journal of Roentgenology*, 175(3):821–825, 2000.

[114] K. Seppi, M.F.H. Schocke, K.J. Mair, R. Esterhammer, C. Scherfler, F. Geser, C. Kremser, S. Boesch, W. Jaschke, W. Poewe, et al. Progression of putaminal degeneration in multiple system atrophy: a serial diffusion MR study. *Neuroimage*, 31(1):240–245, 2006.

[115] S. Chandrasekhar. Stochastic problems in physics and astronomy. *Reviews of modern physics*, 15(1):1–89, 1943.

[116] G.E. Uhlenbeck and L.S. Ornstein. On the theory of the Brownian motion. *Physical Review*, 36(5):823–841, 1930.

[117] SI Denisov, P. Hänggi, and H. Kantz. Parameters of the fractional Fokker-Planck equation. *Europhysics Letters.*, 85(4):40007–1 – 40007–4, 2009.

[118] E. Lutz. Fractional transport equations for Lévy stable processes. *Physical Review Letters*, 86(11):2208–2211, 2001.

[119] H. Yang, G. Luo, P. Karnchanaphanurach, T.M. Louie, I. Rech, S. Cova, L. Xun, and X.S. Xie. Protein conformational dynamics probed by single-molecule electron transfer. *Science*, 302(5643):262–266, 2003.

[120] SC Kou and X.S. Xie. Generalized Langevin equation with fractional Gaussian noise: subdiffusion within a single protein molecule. *Physical review letters*, 93(18):180603, 2004.

[121] B. Robertson. Spin-echo decay of spins diffusing in a bounded region. *Physical Review*, 151(1):273–277, 1966.

[122] J.E. Tanner and E.O. Stejskal. Restricted Self-Diffusion of Protons in Colloidal Systems by the Pulsed-Gradient, Spin Echo Method. *The Journal of Chemical Physics*, 49:1768, 1968.

[123] PT Callaghan, A. Coy, D. MacGowan, KJ Packer, and FO Zelaya. Diffraction-like effects in NMR diffusion studies of fluids in porous solids. *Nature*, 351:467–469, 1991.

[124] SD Stoller, W. Happer, and FJ Dyson. Transverse spin relaxation in inhomogeneous magnetic fields. *Physical Review A*, 44(11):7459–7477, 1991.

[125] P.N. Sen. Time-dependent diffusion coefficient as a probe of geometry. *Concepts in Magnetic Resonance*, 23(1):1–21, 2004.

[126] A. Widom and HJ Chen. Fractal Brownian motion and nuclear spin echoes. *Journal of Physics*, 28:1243–1243, 1995.

[127] J.J. Mor. The Levenberg-Marquardt algorithm: implementation and theory. *Lecture notes in mathematics*, 630:105–116, 1977.